MICROCOPY RESOLUTION TEST CHART

NATIONAL BUREAU OF STANDARDS-1963-A

NUMERICAL SOLUTIONS FOR CRITICAL AND

UNSTEADY SUBCRITICAL FLOW ABOUT AN EXTERNAL

COMPRESSION AXI-SYMMETRIC INLET

DISSERTATION

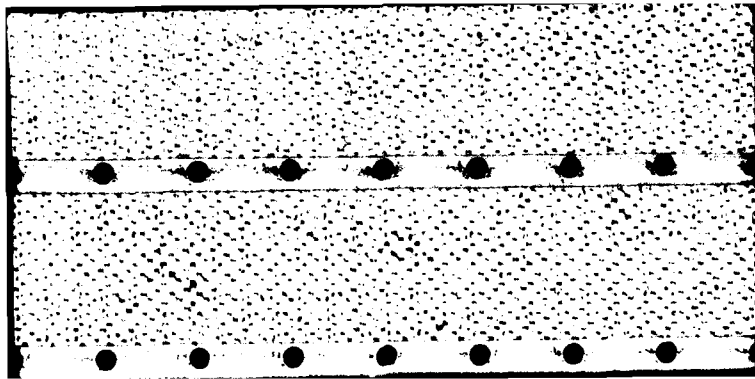AFIT/DS/AA/82-2   Richard W. Newsome, Jr.
                     Capt   USAF

DTIC
ELECTE
FEB 2 3 1983

A

NUMERICAL SOLUTIONS FOR CRITICAL AND

UNSTEADY SUBCRITICAL FLOW ABOUT AN EXTERNAL

COMPRESSION AXI-SYMMETRIC INLET

DISSERTATION

Presented to the Faculty of the School of Engineering

of the Air Force Institute of Technology

Air University

in Partial Fulfillment of the

Requirements for the Degree of

Doctor of Philosophy

by

Richard W. Newsome, Jr., B.S., M.S.

Captain   USAF

Approved for public release; distribution unlimited

NUMERICAL SOLUTIONS FOR CRITICAL AND

UNSTEADY SUBCRITICAL FLOW ABOUT AN EXTERNAL

COMPRESSION AXI-SYMMETRIC INLET

by

Richard W. Newsome, Jr., B.S., M.S.

Captain   USAF

Approved: _____   18 Nov 82
          Chairman

          _____   18 Nov 82

          William C. Elrod _____   18 Nov 82

          David A. Lee _____   18 Nov 82

          Urmila Ghia _____   18 Nov 1982

Accepted:

          J. Przemieniecki   19 Nov 1982
          Dean, School of Engineering

CONTENTS

ACKNOWLEDGEMENTS

I wish to thank the many people who have contributed to the successful completion of this work. Dr. Wilbur Hankey, who served as my committee chairman, suggested the project and provided the resources necessary for its solution. The support and encouragement of Dr. Hankey and Dr. Joseph Shang are gratefully acknowledged. Their insight and sound judgement have been invaluable during the course of this effort. The environment afforded by the Computational Aerodynamics Group has been a source of professional growth and friendship.

I am grateful to the other members of my committee, Dr. David Lee and Dr. William Elrod, of the Air Force Institute of Technology for their advice and careful consideration. I would also like to thank Mrs. Valerie Holler for her expert typing of this dissertation and its many revisions.

Most importantly, I thank my wife, Mary, for her great patience over the long course of this effort. It is to her and our children, Brian and Laura, whose births coincide roughly with its beginning and end, that I dedicate this work. They have served as a constant reminder of what is truly important in life.

LIST OF FIGURES

List of Tables

LIST OF SYMBOLS

A Cross sectional area of diffuser at a given axial location

$A_{*_{eff}}$ Effective throat area corrrected for viscous displacement

A_x, A_y Jacobian matrices of the flux vectors F, and G, Equation C.2

AR Area ratio, A_*/A_c, Equation 4.1

c Speed of sound, $\sqrt{\gamma RT}$

C_p Specific heat, $\dfrac{\partial h}{\partial T}$

C_v Specific heat, $\dfrac{\partial e_I}{\partial T}$

D Inlet Diameter

d_{ij} Deviatoric stress tensor, Equation 2.9

d_{qr} qr'th component of deviatoric stress vector

$\mathcal{D}$ Damping term added to the difference equations, Equation 3.52

e_I Internal energy, Equation 2.13

E Total energy, Equation 2.3

f_n n'th frequency mode

F Flux vector in x coordinate, Equation 2.20

$\bar{F}$ Flux vector in ξ coordinate, Equation 3.8

G Flux vector in y coordinate, Equation 2.20; Amplification matrix in Von Neumann stability analysis, Equation D.4

$\bar{G}$ Flux vector in η coordinate, Equation 3.8

h_i i'th scale factor

h Enthalpy, $e_I + p/\rho$

H Axi-symmetric source term, Equation 2.20

$\bar{H}$ Axi-symmetric source term, computational coordinates, Equation 3.8

I Identify matrix; or complex number $\sqrt{-1}$

J Jacobian $\xi_x \eta_y - \xi_y \eta_x$

k	Thermal conductivity
k_t	Turbulent thermal conductivity
k_ξ, k_η	Wave number in ξ and η coordinates
k_n	Wave number of nth frequency mode
L	Inlet length, cowl lip to diffuser throat
L	Finite difference operator, Equations 3.27, 3.32
$\dot{m}$	Mass flux through diffuser cross sectional area
M	Mach number, $(u^2 + v^2)/c$
$Min_{i,j}$	Denotes minimum value over range of i,j values
N_j	Normal vector
0	Denotes "terms of order"
p	pressure
P	Period of oscillation, Equation 4.3
Pr	Prandtl number, $\dfrac{\mu C_p}{k} = .72$
Pr_t	Turbulent Prandtl number, $\dfrac{\epsilon C_p}{k_t} \equiv .9$
q_i	Heat transfer rate vector
q_r	r'th component of heat transfer rate vector
R	Gas constant
Re	Reynolds number, $(\rho UL)/\mu$
s	Distance along surface from leading edge
St	Strouhal number, $f\delta/U$
t	Time
T	Temperature
TR	Throttle ratio, A_e/A_c, Equation 4.1
$T(\xi,\eta)$	Forcing function for coordinate line attraction in Thompson's Method
u_i	Velocity vector
u	Velocity component in x direction

U	Conservative variables vector, Equation 2.20
U_c	Contravariant velocity component, Equation 3.7
U_ξ	Term in time step calculation, Equation 3.50
u	Velocity component tangent to wall surface
U	Conservative variables vector in computational coordinates, Equation 3.8
v	Velocity component in y direction
V	Non-conservative dependent variables, Equation 3.43
V_c	Contravariant velocity component, Equation 3.7
V_ξ	Term in time step calculation, Equation 3.50
V	Velocity scale for eddy viscosity, Equations 2.38, 2.39
x_i	i'th coordinate
x	Axial coordinate
y	Radial coordinate
y_n	Distance normal to surface
y_o	Body radius

GREEK AND SPECIAL SYMBOLS

α	Courant-Friedrichs-Lewy number, Equation 3.47
β	Damping coefficient, Equation 3.52
γ	Ratio of specific heats, C_p/C_v
$\Gamma(s)$	Transition function for transition from Laminar to turbulent flow, Equation 2.40
∂_q	Partial Derivative, ∂/∂_q
δ_1	Incompressible 2-D displacement thickness
δ_{ij}	Kronecker delta, $(1, i = j; 0, i \neq j)$
δ_q	2nd order central difference approximation to the partial derivative ∂_q, Appendix A
δ_{qr}	2nd order central difference approximation to the 2nd partial derivative ∂_{qr}, Appendix A
Δ	Increment

Δ_q	1st order forward difference approximation to the partial derivative ∂_q, Appendix A
∇_q	1st order backward difference approximation to the partial derivative ∂_q, Appendix A
∇^2	Laplacian operator
ΔS_ξ, ΔS_η	Terms in time step calculation, Equation 3.50
ϵ	Eddy viscosity coefficient
ϵ_d	Displacement correction for throat area
η	Computational coordinate
Θ	Azimuthal coordinate
Θ_1, Θ_2	Terms in time step calculation, Equation 3.50
κ	Exit area reduction constant due to struts, Equation E.1
κ_1	Von Karman's constant (.40)
κ_2	Clauser's constant (.0168)
ℓ	Turbulent mixing length scale, Equations 2.37, 2.39
λ	Second viscosity coefficient, $-2/3\ \mu$
λ_t	Turbulent second viscosity coefficient, $-2/3\ \epsilon$
λ_n	Wave length of n'th frequency mode
μ	Viscosity coefficient
ξ	Computational coordinate
ρ	Density
τ_{ij}	Stress tensor, Equations 2.8, 2.17
τ_{qr}	qr'th component of the stress tensor
ϕ	Amplitude function in Von Neumann's stability analysis
χ	Mach number function, Equation 1.1
ω_n	Circular frequency, $2\pi f_n$

SUBSCRIPTS

*	Denotes properties at the downstream throat
c	Denotes axial station at cowl lip
e	Denotes diffuser exit station
d	Denotes an arbitrary axial location within the duct
D	Diameter
o	Reference station
x,y	1st partial derivative with respect to x or y
xx, xy yy	2nd partial derivatives with respect to x and/or y
w	Denotes value at the wall
ref	Reference value at boundary layer edge
ξ,η	1st partial derivative with respect to ξ or η
$\xi\xi$, $\xi\eta$, $\eta\eta$	2nd partial derivatives with respect to ξ and/or η
i	Index for the ith ξ location
j	Index for the jth η location
aw	Denotes adiabatic wall temperature

SUPERSCRIPTS

—	Time averaged mean value, Equation 2.22
'	Fluctuating component of time averaged value, Equation 2.22
~	Mass averaged mean value, Equation 2.22
"	Fluctuating component of mass averaged value, Equation 2.22
n	Denotes evaluation at the nth time level
$\overline{n+1}$	Denotes evaluation at a provisional n + 1 time level
*, **	Intermediate time levels in the fractional step equations

ABSTRACT

The unsteady, compressible, Reynolds-averaged Navier-Stokes
equations were solved for the flow field about an external compression
axi-symmetric inlet with a length to diameter ratio, L/D = 15.88, at
Mach 2.0 and a Reynolds number based on diameter, Re_D = 2.36x10^6, operat-
ing in the near-critical and subcritical flow regimes. The near-critical
solution reached a stable steady state while the subcritical solutions
attained an unstable bounded oscillatory state, characterized by large
amplitude pressure oscillations and traveling shock waves. This phenomenon
is the result of a shear layer instability combined with a closed-loop
feedback of reflected disturbances and the naturally occurring self-
sustained oscillations are commonly known as buzz. Numerical results
are given in terms of Mach contours, velocity plots, pressure-time traces
at selected stations, as well as mass flux and other mass-averaged
quantities along the duct length. Comparison with experiment is also
given.

Section I

INTRODUCTION

The fluid dynamic behavior of a supersonic inlet, operating in the critical and subcritical flow regimes has been of interest since the earliest experiments with supersonic diffusers. These flow conditions correspond to a normal shock location at or before the diffuser throat (minimum cross sectional area) near the inlet entrance. The critical flow regime is the point of optimum diffuser efficiency and results in maximum mass flow, pressure recovery, and stream thrust. Unfortunately, the critical and, more typically, the subcritical flow regimes are characterized by the onset of violent flow oscillations within the inlet and rapid movement of the normal or bow shock on the centerbody. This motion is termed buzz and is frequently violent enough to result in structural damage, engine surge (jet engine), combustion flameout, or non-recoverable thrust loss (ramjet). Although the buzz phenomenon has been studied for almost forty years it remains poorly understood. To this day, there is no analytic method for predicting the amplitude or frequency of the oscillations or even a certain method for predicting buzz onset.

With the advent of "super computers" such as the CRAY 1-S and the rapid maturity of computational fluid dynamics as a discipline, it has recently become possible to calculate numerical solutions in these flow regimes from the fundamental equations of fluid mechanics - the Navier-Stokes equations. Although this approach is certainly not without its own difficulties, it does offer the possibility of complete information without regard to instrumentation and the potential for new insight into the problem. The purpose of this report is to document a numerical

study of the near-critical and subcritical regimes of an external compression axi-symmetric inlet tested experimentally at the University of Tokyo by Nagashima, Obokata, and Asanuma (Ref 1) in 1972.

1.1 Operating Characteristics of Supersonic Inlets

The operating characteristics of a supersonic inlet can be classified as either supercritical, critical or subcritical (Refs 2,3). The three regimes are illustrated in Figure (1) for an external compression inlet at the design Mach number. In this type of inlet, the minimum entrance area, A_c, occurs at the cowl lip. The design Mach number corresponds to a flight condition in which the conical shock impinges on the tip of the cowl lip. For a given flight condition (Mach number and angle of attack), the operating condition of the diffuser is determined by the diffuser back pressure required to match that dictated by the downstream component. This downstream component could be a throat, a combustor, or a compressor face. For the case at hand, the downstream component is a throat and the operating condition is determined by the requirement that the mass flow passed by the downstream throat must equal that captured by the inlet

$$\dot{m}_* = \frac{A_* P_{t_*}}{\sqrt{RT_{t_*}}} X_* = \frac{A_c P_{t_c}}{\sqrt{RT_{t_c}}} X_c = \dot{m}_c \qquad (1.1)$$

where

$$X(\gamma,M) = \frac{\sqrt{\gamma}\ M}{(1+ \frac{\gamma-1}{2} M^2)^{\frac{\gamma+1}{2(\gamma-1)}}}$$

and all properties are mass-averaged over the station cross sectional area. This leads to the relation

$$\left(\frac{P_{t_*}}{P_{t_c}}\right) = \left(\frac{A_c}{A_*}\right) \left(\frac{X_c}{X_*}\right) \sqrt{\frac{T_{t_*}}{T_{t_c}}} \qquad (1.2)$$

2

Supercritical

$$A_{cap} = A_c$$

Critical

$$A_{cap} = A_c$$

Subcritical

$$A'_{cap}$$

$$A'_c$$

expelled shock wave
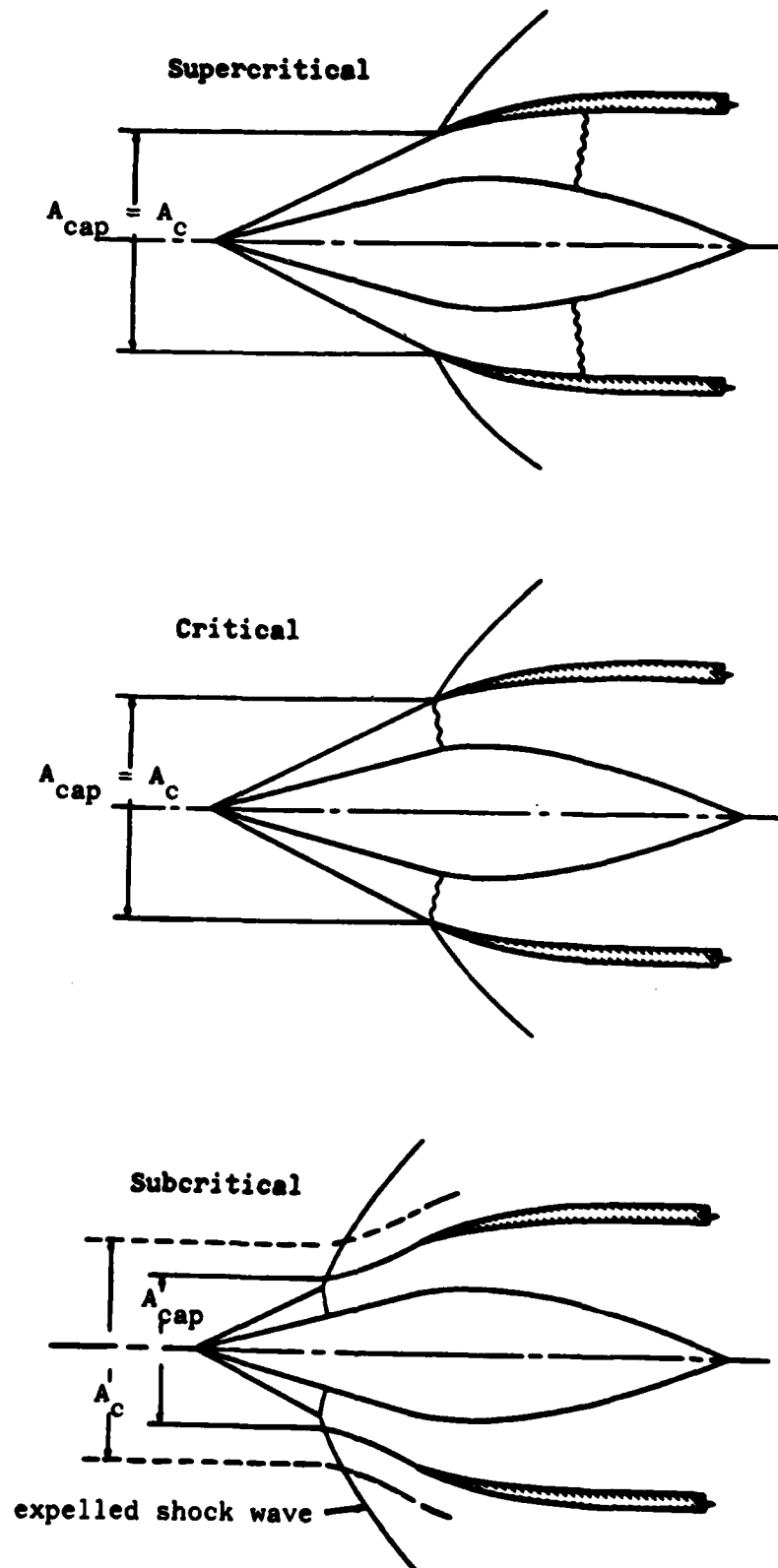
Fig. 1 Operating Regimes of a Supersonic External
Compression Inlet (from Ref 3)

3

In the supercritical regime, the downstream throat may be assumed to be choked for the throat areas considered. The mass flow captured by the inlet is a maximum and is determined by the geometry and flight condition (A_c, p_{t_c}, X_c specified). As the throat area, A_*, is changed, the downstream total pressure, p_{t_*}, is then determined by Equation (1.2). This serves to position the shock system within the diffuser since the majority of the total pressure loss is shock induced. As the downstream throat is further closed, a higher p_{t_*} is required. This can only be produced if the shock is forced upstream in the diffuser where it occurs at a lower averaged Mach number and a smaller total pressure loss. If the throat area is sufficiently reduced the normal shock will be positioned at the cowl lip. As mentioned previously, this critical regime is the point where maximum mass flow and highest pressure recovery are coincident. Any further decrease in throat area will force the normal shock out of the diffuser to a position on the centerbody so that mass flow may be spilled to a level which can be passed by the downstream throat. This is the subcritical regime and is where buzz typically occurs.

In the past, inlets have been designed to avoid the unstable flow regime through the use of such devices as by-pass doors, boundary layer bleed, or fuel flow limiters. However, the requirement for a stable operating regime often imposes a substantial penalty on the inlet in terms of diffuser efficiency (total pressure recovery) or additive drag. This impacts total flight vehicle performance but most significantly it may impose bounds in the flight envelope for off-design and maneuvering conditions. A more thorough understanding of

4

buzz is a necessary first step toward the design of future inlets less susceptible to its adverse effects.

1.2 Review of Previous Investigations into Inlet Buzz

Oswatitsch (Ref 4) first observed inlet buzz during the course of experimental work in 1944 but did not explain its occurrence.

Ferri and Nucci (Ref 5) tested a variety of external compression diffuser geometries. They identified the cause of the instability as the entrance of a vortex sheet (free shear layer) into the cowl. The vortex sheet resulted from (1) the interaction of the oblique conical and the strong bow shock or (2) a lambda shock at the base of the centerbody resulting from the shock-induced boundary layer separation. In their view, the vortex sheet tended to cause the boundary layer on the inner cowl wall to separate which then choked the flow. Pressure waves propagated forward and drove the shock further outward. The subsequent reduction in mass flow decreased the back pressure, the bow shock retreated and the vortex sheet was expelled. Once initiated, the process continued in a periodic fashion. Their theory is incomplete since stable flow has been observed with vortex sheet impingement on the cowl.

Sterbentz and Evvard (Ref 6) and Sterbentz and Davids (Ref 7) used a Helmholz resonator analogy in which the inlet mass flow was modeled as a slug of air bounded downstream by a weightless spring to predict resonant frequency and amplitude. This led to an instability requirement that the diffuser pressure recovery curve as a function of mass flow should have a positive slope in the subcritical region. This hypothesis has been shown to be false. Further, the theory cannot predict

5

the onset of buzz and does not model the actual physical processes.

Trimpi (Ref 8) advanced a modified one-dimensional characteristic theory in which the buzz cycle was traced through the inlet as a series of compression and expansion waves propagating and reflecting from the bow shock and the choked nozzle throat. His theory did not predict the onset of buzz and in fact required the use of experimental data to start the calculation when the shock was in motion ahead of the cowl. The Helmholz resonator and wave propagation theories are not compatible. Trimpi, in a later experimental study (Ref 9), proposed a prediction method for buzz amplitude and further suggested a qualitative method in which stability was related to the instantaneous ratio of entropy increase to mass flow decrease. He observed the occurrence of low frequency buzz, which agreed well with his theory, and of an intermittent high frequency buzz whose origin he postulated to be localized near the inlet entrance.

Dailey (Ref 10) also observed experimentally both high and low frequency oscillations. For high frequency oscillation which occurred at low mass flows, he suggested vortex shedding at the cowl lip. For low frequency buzz, characteristic at higher subcritical mass flows, Dailey postulated that the instability was initiated within the separated boundary layer on the centerbody. This is in contrast with the theory of Ferri in which instability resulted from vortex sheet impingement on the cowl. According to Dailey, the inlet flow was completely blocked due to massive separation within the inlet. Upstream of the blockage, mass accumulated and forced the bow shock upstream until flow was spilled from the cowl lip. Downstream of the blockage, back pressure decreased and the flow collapsed to restart the cycle. In Dailey's

6

view, the buzz cycle was governed by a relaxation process determined by the time required for mass to fill up and spill from the diffuser. Trimpi had previously described this process in terms of wave propagation and Refs (11) and (12) indicate the sharp disagreement between the theories of Trimpi and Dailey.

In a subsequent study, Brown (Ref 13) tested a series of inlet types. Results were similar to those of Dailey (Ref 10). Brown advanced the hypothesis of an edge tone phenomenon to explan the high frequency oscillation and the sudden shifts in frequency.

Mirels (Ref 14) performed a one dimensional analysis of small perturbations in which the mechanism leading to buzz is the amplification of acoustic waves due to successive reflections in the combustion or plenum chamber. He concluded the flow would be unstable when the real part of the acoustic impedance of the inlet is greater than a term of the same order of magnitude as the combustion chamber Mach number.

Previously, Stoolman (Ref 15) had considered the stability of a normal shock diffuser. The mechanism for stability considered, was again the amplification ratio of reflected to incident waves. He concluded that the diffuser was unstable in the absence of viscous dissipation. His conclusion was contradicted by Chang and Hsu (Ref 16) who reported that acoustic impedance was always negative and the flow always stable in the absence of viscous dissipation. In a later paper (Ref 17), solutions to one-dimensional quasi-steady, linearized equations for viscous compressible flow indicated that instability was possible, due to wave amplification at the inlet entrance when entropy production due to viscous dissipation was considered.

7

Kowalewicz (Ref 18) considered the stability of a normal shock diffuser with the extension of accounting for mass flow spillage and divergence in diffuser cross-sectional area. The approach was to linearize the governing equations, assume harmonic solutions, and solve the eigenvalue problem to predict natural frequency and damping. Since viscosity was not considered, for high subcritical mass flows (low spillage, where the theory was valid), the flow was found to be stable, in agreement with the results of Chang and Hsu.

In experimental testing of 2-D inlets of the Concorde type, Fisher, Neale, and Brooks (Ref 19) identified two distinct amplitudes of buzz of roughly the same frequency - little buzz and big buzz. In both cases the triggering mechanism was the entrance of a shear zone with a total pressure gradient into the diffuser (Ferri condition). Instability was dependent upon the magnitude of the total pressure change and its gradient, as well as its proximity to the cowl lip. Specifically, little buzz was associated with the intersection of the normal shock with the ramp hinge shock and isentropic fan. Big buzz was found to be initiated by the intersection of the normal shock with the initial wedge shock. The strength of the shear zone total pressure gradient was then sufficient to cause downstream boundary layer separation which resulted in inlet throat choking and large amplitude oscillation in the manner described by Dailey.

Steward and Fisher (Ref 20) studied the effects of freestream turbulence, Reynolds number, and surface roughness, on axi-symmetric inlets at Mach numbers near two. They observed the Ferri instability at centerbody positions in which the shock impinged on the cowl lip. For other positions, they found the instability resulted from centerbody

boundary layer instability. At higher subcritical mass flows this type of instability resulted in a very mild and erratic oscillation termed flutter. The much larger amplitude oscillation, buzz, was encountered if a turbulent boundary layer trip was placed at the center-body tip or if the mass flow were further reduced.

Nagashima, Obokata and Ananuma (Ref 1) experimentally studied in-stability in axisymmetric external compression inlets. They found that both high and low frequency buzz, as measured by spectral analyser, have definite spikes as predicted by an acoustic model. This report was chosen as the basis for numerical comparison and is described in detail in Section IV.

Sajben, et.al. (Refs 21, 22, 23, 24) appear to have conducted the most comprehensive experimental investigation of diffuser instability. Two different nominally two dimensional supercritically operating diffusers with area ratios of A_e/A_c = 1.52 and 2.37 were considered. A variety of pressure ratios were tested, corresponding to different up-stream normal shock Mach numbers. The smaller area ratio diffuser was found to be relatively quiet with naturally occurring pressure dis-turbances on the order of $\Delta P/P_t \simeq .06$, while the larger area ratio model displayed disturbances of $\Delta P/P_t \simeq .11 \rightarrow .15$ and shock wave movement equal to one throat height. The characteristic length scale for the weaker shock conditions was the duct length and the disturbance propagation was acoustic in origin. For the stronger shock conditions, the characteristic length scale corresponded with the inviscid core length and the disturbance propagation was not acoustic. Forced disturbances at the diffuser exit were also investigated and resonance was not found.

9

1.3 Computational Fluid Dynamics Applied to Internal Flows and Flows With Self-Sustained Oscillations

Internal Flows

The field of computational aerodynamics has continued its rapid evolutionary growth as a major tool in aerodynamics research. Early computational approaches to internal flow problems consisted of the method of characteristics or potential flow methods for the inviscid flow coupled with a boundary layer method for the viscous flow field. However, the unsteady Reynolds-averaged Navier-Stokes equations must be solved for many "real life" diffusers because of the presence of strong shock-boundary layer interactions, subsonic flow, and boundary layer separation due to the adverse pressure gradients inherent in diffusers. Restricting attention to the Navier-Stokes equations, Knight (Ref 25) gave the first solution to a realistic high Reynolds number inlet. Numerical solutions were obtained for the two-dimensional steady flow about two hypersonic inlet geometries. More recently, Knight (Refs 26, 27) considered the supersonic flow associated with a Mach 2.5 inlet with the extension of accounting for boundary layer bleed and improving algorithm efficiency. Currently, work on three dimensional Navier-Stokes calculations of inlet flows is still in progress (Ref 28). As an alternative to the considerable cost of solutions to the full Navier-Stokes equations, parabolized procedures have also been developed, in which streamwise diffusive terms are dropped, allowing spatial marching in the primary flow direction. Reference (29) describes a procedure which has been applied to supersonic diffuser flows with adverse pressure gradients so long as streamwise separation was not encountered. References (30, 31) summarize the status of current computa-

10

tiona¹ methods applied to internal aerodynamics.

Flows Exhibiting Self-Sustained Oscillations

Steady state solutions to the Navier-Stokes equations are nor-
mally obtained from the unsteady equations by a relaxation process to
an asymptotic steady state condition. It was realized, however, that
these equations should also provide accurate temporal resolution of
unsteady flows as well. An important subset of unsteady flows includes
those, with no external forcing function, for which a steady state
solution does not exist. These flows exhibit bounded self-sustained
oscillations which are periodic or quasi-periodic. Levy (Ref 32) was the
first to demonstrate that current Navier-Stokes algorithms were capable
of reproducing the time dependent aspects of the mean flow in an
unsteady turbulent flow field. Levy considered the flow about a thick
airfoil in the transonic regime. The flow was found to be steady
except in a critical Mach number regime where the shock on the upper
and lower surfaces displayed an asymmetric oscillation. The flow
oscillated between the trailing edge separation observed at lower Mach
numbers and a shock induced separation at higher Mach numbers. Good
agreement with experiment was found but inadequacies in the turbulence
model for the separated region were noted.

Steger and Bailey (Ref 33) successfully simulated the fluid dy-
namically driven flutter or buzz of the aileron of a P-80 airfoil at the
flight condition where it had been observed experimentally some 30 years
earlier. The flow was steady at lower Mach numbers and unsteady at higher
Mach numbers, in accord with experiment. Inviscid calculations were
found to decay or diverge, depending upon the Mach number, indicating

the crucial role played by viscosity in establishing a repeatable, bounded limit cycle.

Shang and Hankey have considered several flows which exhibit self-sustained oscillations. The pressure oscillations produced by the shear layer instability in the supersonic flow over an open cavity were computed in Ref (34). Linear stability theory was also used to explain the resonant phenomenon. In Ref (35), numerical solutions were obtained for two different spike lengths for the axi-symmetric flow over spike-tipped bodies in a Mach three laminar flow regime. The shorter length body resulted in a stable flow in accord with the experiment and linear stability theory. The longer length body produced a large amplitude high frequency oscillation in excellent agreement with the experiment in both frequency and amplitude of the observed oscillations. Shang (Ref 36) also considered the oscillatory flow about a cylinder involving the periodic shedding of vorticity. The numerical simulation again was successful in reproducing the dominant fluid dynamic mechanisms.

Very recently, Liou and Coakley (Refs 37, 38) computed several of the cases investigated experimentally by Sajben for both forced and self-sustained oscillations. The forced oscillations computed were predicted well in terms of amplitude and phase angle although shock displacement was overpredicted in some cases. For the self-sustained oscillations, good agreement in predicted frequency was obtained at moderate and weak shock pressure ratios. At the strong shock pressure ratio, the computed frequency was 1.75 times the experimental result. The authors noted a substantial sensitivity in the degree of flow separation and in the unsteady flow behavior to small changes in the constants of the turbulence model.

12

Chapman (Ref 39) summarized, in 1979, the two key features found in successful solutions of the Reynolds-averaged Navier-Stokes solutions for unsteady turbulent flows: (1) the flowfield exhibits a single dominant oscillatory frequency, (2) this frequency is an order of magnitude lower than the mean frequency of the turbulent eddies. To date, Liou and Coakley have published the only computational work concerned with unsteady diffuser flows. This differs from the present effort in that it addresses the relatively mild oscillations found in the supercritical flow regime. The present effort is directed toward the much larger amplitude instability in both the internal and external flowfields associated with the subcritical flow regime.

1.4 Research Objectives

The review of previous work is indicative of the complexity of the problem. The inlet flow is characterized by large regions of separated flow and viscous-inviscid (shock boundary layer) interaction in an unsteady, turbulent flow. Experimental studies have been extremely limited by instrumentation. Previous analytic works have not fully modeled the real flow and, as a result, have arrived at incomplete and at times contradictory results. Today the actual physical mechanisms involved in inlet buzz are still unresolved.

The objective of this effort is to compute Navier-Stokes solutions for the flowfield about an inlet operating in the near-critical and the unstable subcritical regimes. These computations provide the first test of current Navier-Stokes algorithms to numerically capture the buzz phenomenon which occurs during subcritical flow conditions. As such, they offer the potential of providing a new tool in our effort to better

13

understand the instability process. Because different instability mechanisms are present in different configurations, one specific experiment has been chosen for comparison. The external compression axi-symmetric inlet tested by Nagashima, Obokata, and Asunama was selected as the basis for numerical solutions. One steady state solution will be obtained for verification of the solution procedure and then several solutions in the unsteady, subcritical regime will be studied. Where possible, the numerical solution will be compared with experiment and analysis to provide a unified explaination of inlet buzz.

Section II

MATHEMATICAL DESCRIPTION OF THE PROBLEM

2.1 Governing Equations

The equations governing the motion of an unsteady, compressible, viscous gas with no body forces or heat sources are derived from conservation laws of mass, momentum, and energy. Conservation of mass (continuity) states that the rate of increase of mass in a given volume is equal to the net rate of inflow of mass through the bounding surface, or,

$$\int_v \frac{\partial}{\partial t} (\rho) \, dv = -\int_s (\rho) \, u_j \, n_j \, ds \tag{2.1}$$

making use of cartesian tensor notation with the summation convention. Conservation of momentum states that the rate of increase of momentum within a control volume is equal to the net rate of inflow of momentum through the surface plus the net force acting on the volume at the surface, or,

$$\int_v \frac{\partial}{\partial t} (\rho u_i) dv = -\int_s (\rho u_i) \, u_j \, n_j \, ds + \int_s \tau_{ij} \, n_j \, ds \tag{2.2}$$

Conservation of energy requires that the rate of change of energy within a volume is equal to the net rate of transport of energy through the surface plus the rate of heat addition and rate of work done on the volume at the surface.

$$\int_v \frac{\partial}{\partial t} (\rho E) dv = -\int_s (\rho E) \, u_j \, n_j \, ds - \int_s q_j \, n_j \, ds + \int_s u_i \, \tau_{ij} \, n_j \, ds$$

with

$$E = (e_I + \frac{1}{2} u_k u_k) \tag{2.3}$$

Making use of the Gauss divergence theorem,

$$\int_s \alpha n_j \, ds = \int_v \frac{\partial}{\partial x_j} (\alpha) \, dv \tag{2.4}$$

15

the equations may be written in differential form, valid for an arbitrary infinitesimal volume:

$$\frac{\partial}{\partial t}(\rho) + \frac{\partial}{\partial x_j}(\rho u_j) = 0, \tag{2.5}$$

$$\frac{\partial}{\partial t}(\rho u_i) + \frac{\partial}{\partial x_j}(\rho u_i u_j - \tau_{ij}) = 0, \tag{2.6}$$

$$\frac{\partial}{\partial t}(\rho E) + \frac{\partial}{\partial x_j}(\rho u_j E - u_i \tau_{ij} + q_j) = 0 \tag{2.7}$$

These equations are commonly known as the Navier-Stokes equations and describe the dynamics of very general flows. Complete derivations may be found in many books, for example, Liepmann and Roshko (Ref 40: 332-338).

The stress tensor is composed of a pressure term acting normal to the surface and non-isotropic term, the deviatoric stress tensor, d_{ij}, producing normal and tangential stress as a consequence of the viscosity of the fluid

$$\tau_{ij} = -p\delta_{ij} + d_{ij} \tag{2.8}$$

For a Newtonian fluid, the deviatoric stress is linearly related to the rate of strain and can be expressed as

$$d_{ij} = \mu\left(\frac{\partial u_i}{\partial x_j} + \frac{\partial u_j}{\partial x_i}\right) + \lambda \delta_{ij} \frac{\partial u_k}{\partial x_k} \tag{2.9}$$

The heat flux vector is taken from Fourier's law

$$q_j = -k \frac{\partial T}{\partial x_j} \tag{2.10}$$

From Sutherland's law, the viscosity is

$$\frac{\mu}{\mu_o} = \left(\frac{T}{T_o}\right)^{3/2} \left(\frac{T_o + 110°K)}{T + 110°K)}\right) \tag{2.11}$$

$\lambda = -2/3 \; \mu$ (Stoke's hypothesis) and $k = \mu \; C_p/Pr$

The equations are closed by an equation of state. For the present problem, a perfect gas may be assumed:

$$p = \rho RT \tag{2.12}$$

16

and if the gas is calorically perfect,

$$e_I = C_v T \qquad (2.13)$$

Together with proper initial and boundary conditions, the equation set (2.5) to (2.13) complete the mathematical problem description.

2.2 Axi-symmetric Coordinate System

Since the problem to be considered involves an axi-symmetric inlet, the most natural coordinate system is a cylindrical one. If the inlet is only examined at zero angle of attack the flowfield exhibits no azimuthal dependence and one of the three momentum equations may be deleted, with additional simplifications in the remaining equations.

Equations (2.5) to (2.7) may be generalized to any orthogonal curvilinear coordinate system as:

$$\frac{\partial}{\partial t}(\rho) + \frac{1}{h_1 h_2 h_3} \sum_j \frac{\partial}{\partial x_j}(\frac{h_1 h_2 h_3}{h_j}\rho u_j) = 0 \qquad (2.14)$$

$$\frac{\partial}{\partial t}(\rho u_i) + \frac{1}{h_1 h_2 h_3}\{\sum_j [\frac{\partial}{\partial x_j}(\frac{h_1 h_2 h_3}{h_j})\rho u_i u_j - \tau_{ij}])$$

$$+ \frac{h_1 h_2 h_3}{h_i h_j}[\rho u_i u_j - \tau_{ij}]\frac{\partial h_i}{\partial x_j} - \frac{h_1 h_2 h_3}{h_i h_j}[\rho u_j u_j - \tau_{jj}]\frac{\partial h_j}{\partial x_i}]\} = 0$$
$$(2.15)$$

$$\frac{\partial}{\partial t}(\rho E) + \frac{1}{h_1 h_2 h_3}\{\sum_j [\frac{\partial}{\partial x_j}(\frac{h_1 h_2 h_3}{h_j}[\rho u_j E - \sum_i u_i \tau_{ij} + q_j]\} = 0$$
$$(2.16)$$

with

$$\tau_{ij} = -p\delta_{ij} +$$
$$(\mu)\{\frac{1}{h_j}\frac{\partial u_i}{\partial x_j} + \frac{1}{h_i}\frac{\partial u_j}{\partial x_i} - \frac{u_i}{h_i h_j}\frac{\partial h_i}{\partial x_i} - \frac{u_i}{h_i h_j}\frac{\partial h_i}{\partial x_j}$$
$$+ \delta_{ij}\sum_k[\frac{u_k}{h_i h_k}\frac{\partial h_i}{\partial x_k} + \frac{u_k}{h_j h_k}\frac{\partial h_j}{\partial x_k}]\}$$
$$+ (\lambda)\frac{1}{h_1 h_2 h_3}\{\sum_k \frac{\partial}{\partial x_k}(\frac{h_1 h_2 h_3}{h_k}u_k)\}\delta_{ij} \qquad (2.17)$$

17

$$q_j = -\gamma\left(\frac{\mu}{Pr}\right) \frac{1}{h_j} \frac{\partial e_I}{\partial x_j} \tag{2.18}$$

$$E = \left(e_I + \frac{1}{2} \sum_k u_k u_k\right) \tag{2.19}$$

For cylindrical coordinates

$$x_1 = x$$
$$x_2 = y$$
$$x_3 = \theta$$

and the scale factors are

$$h_1 = 1$$
$$h_2 = 1$$
$$h_3 = x_2 = y$$

Substituting, and imposing the axi-symmetric requirement

$$\frac{\partial}{\partial \theta} = 0 \qquad u_3 = 0$$

the equations may be expressed in vector form as:

$$\frac{\partial}{\partial t}(U) + \frac{\partial}{\partial x}(F) + \frac{1}{y}\frac{\partial}{\partial y}(yG) = \frac{1}{y}H \tag{2.20}$$

where

$$U = \begin{bmatrix} \rho \\ \rho u \\ \rho v \\ \rho E \end{bmatrix} \qquad F = \begin{bmatrix} \rho u \\ \rho u^2 - \tau_{xx} \\ \rho uv - \tau_{yx} \\ \rho uE - u\tau_{xx} - v\tau_{xy} + q_x \end{bmatrix}$$

$$G = \begin{bmatrix} \rho v \\ \rho uv - \tau_{xy} \\ \rho v^2 - \tau_{yy} \\ \rho vE - u\tau_{yx} - v\tau_{yy} + q_y \end{bmatrix} \qquad H = \begin{bmatrix} 0 \\ 0 \\ -\tau_{\theta\theta} \\ 0 \end{bmatrix}$$

and

$$\tau_{xx} = -p + 2\mu \frac{\partial u}{\partial x} + \lambda\{\frac{\partial u}{\partial x} + \frac{1}{y}\frac{\partial}{\partial y}(yv)\}$$

$$\tau_{xy} = \tau_{yx} = \mu(\frac{\partial u}{\partial y} + \frac{\partial v}{\partial x})$$

$$\tau_{yy} = -p + 2\mu \frac{\partial v}{\partial y} + \lambda\{\frac{\partial u}{\partial x} + \frac{1}{y}\frac{\partial}{\partial y}(yv)\}$$

$$\tau_{\theta\theta} = -p + 2\mu \frac{v}{y} + \lambda\{\frac{\partial u}{\partial x} + \frac{1}{y}\frac{\partial}{\partial y}(yv)\}$$

$$q_x = -\gamma \frac{\mu}{Pr}\frac{\partial e_I}{\partial x} \qquad q_y = -\gamma\frac{\mu}{Pr}\frac{\partial e_I}{\partial y}$$

$$E = e_I + \frac{1}{2}(u^2 + v^2)$$

The vector components correspond to the continuity, two momentum, and energy equations respectively.

2.3 Reynolds-Averaged Navier-Stokes Equations

In many cases, the flow is turbulent and is characterized by random fluctuations in all variables. Usually, it is impossible to numerically resolve all of the length and time scales involved, and so an averaging process is carried out to solve for the mean motion which is of primary importance anyway. According to Chapman (Ref 39) this averaging is valid for unsteady flows as well, provided that its time scale is long in comparison with the mean frequency of the turbulent eddies, yet short when compared to the time scale of the unsteady flow.

Rubesin and Rose (Ref 41) introduced an averaging procedure which leads to a convenient form of the equations. The dependent variables are written in terms of time averaged mean and fluctuating terms:

$$\rho = \bar{\rho} + \rho'$$
$$p = \bar{p} + p'$$
$$\tau_{ij} = \bar{\tau}_{ij} + \tau_{ij}'$$
$$q_i = \bar{q}_i + q_i'$$

(2.21)

19

and mass averaged mean and fluctuating quantities:

$$u_i = \tilde{u}_i + u_i''$$

$$e = \tilde{e} + e''$$

$$\mu = \tilde{\mu} + \mu'' \qquad (2.22)$$

$$k = \tilde{k} + k''$$

By definition

$$\bar{f} = \int_{t_1}^{t_1 + t_m} f\,dt \qquad t_{t.e.} << t_m << t_{ch} \qquad (2.23)$$

The following rules of averaging are assumed to apply:

$$\overline{\bar{f}} = \bar{f}$$

$$\overline{\bar{f}'} = 0$$

$$\overline{f + g} = \bar{f} + \bar{g}$$

$$\overline{\bar{f}g} = \bar{f}\,\bar{g} \qquad (2.24)$$

$$\overline{\frac{\partial f}{\partial s}} = \frac{\partial}{\partial s}(\bar{f})$$

$$\overline{f\,ds} = \bar{f}\,ds$$

In mass averaging, the mass flux is written as a single term and the mean velocity is defined as

$$\tilde{u}_i = \bar{\bar{u}}_i = \frac{\overline{\rho u_i}}{\bar{\rho}} \qquad (2.25)$$

then

$$\overline{\rho u_i} = \overline{(\bar{\rho} + \rho')(\tilde{u}_i + u_i'')} = \bar{\rho}\tilde{u}_i + \overline{\rho'\tilde{u}_i} + \overline{\rho u_i''}$$

giving

$$\overline{\rho u_i''} = 0 \qquad (2.26)$$

Also

$$\overline{\rho u_i} = \overline{(\bar{\rho} + \rho')(\bar{u} + u_i'')} = \overline{\bar{\rho}\tilde{u}_i} + \overline{\rho'\tilde{u}_i} + \overline{\bar{\rho}u_i''} + \overline{\rho'u_i''}$$

20

which implies

$$\overline{u_i''} = - \frac{\overline{\rho' u_i''}}{\bar{\rho}} \neq 0 \tag{2.27}$$

Expressions similar to equations (2.25) to (2.27) may also be written

for the internal energy, e_I. Upon substituting the variables, in terms

of mean and fluctuating quanities, into equations (2.5) to (2.7) and

time averaging, the following mean flow equations result:

$$\frac{\partial}{\partial t}(\bar{\rho}) + \frac{\partial}{\partial x_j} \left[\bar{\rho}\, \tilde{u}_j \right] = 0 \tag{2.28}$$

$$\frac{\partial}{\partial t}(\bar{\rho}\, \tilde{u}_i) + \frac{\partial}{\partial x_j} \left[\bar{\rho}\tilde{u}_i\tilde{u}_j - (\overline{\tau_{ij}} - \overline{\rho u_i''u_j''}) \right] = 0 \tag{2.29}$$

$$\frac{\partial}{\partial t}(\bar{\rho}\tilde{E}) + \frac{\partial}{\partial x_j} \left[\tilde{u}_j\bar{\rho}\tilde{E} - \tilde{u}_i(\overline{\tau_{ij}} - \overline{\rho u_i''u_j''}) + \bar{q}_j + \overline{\rho u_j''e_I''} \right] = 0 \tag{2.30}$$

The term

$$\overline{u_i'' \left(\tau_{ij} - \frac{1}{2} \rho u_i''u_j'' \right)}$$

has been neglected from (2.30) by order of magnitude considerations.

The equations for the stress tensor and heat flux vector assume the same

form as their laminar counterparts if fluctuating quantities are again

assumed small in comparison to mean values.

Equations (2.28) to (2.30) differ from their laminar counterparts

only with the exception of the following additional terms:

$$- \overline{\rho u_i''u_j''} \quad \text{(Reynolds stress)} \tag{2.31}$$

$$\overline{\rho u_j''e_I''} \quad \text{(Reynolds heat flux)} \tag{2.32}$$

These terms represent the effect of the turbulent fluctuations on the

mean motion. For example, the Reynolds stress term represents an

apparent additional stress which is a property of the flow and not

the medium.

2.4 Turbulence Model

The turbulent fluctuating averages are additional unknowns for which there are no corresponding equations. The equations must be closed at some point by appropriate expressions for the unknowns. Most practical methods to date have been based upon the eddy viscosity concept. This includes the simpler algebraic models as well as the more complicated one and two equation models. The Reynolds stress tensor is modeled as being proportional to the laminar stress tensor of the mean flow, with the coefficient of proportionality being defined as the eddy viscosity

$$- \overline{\rho u_i'' u_j''} = \epsilon \left(\frac{\partial \tilde{u}_i}{\partial x_j} + \frac{\partial \tilde{u}_j}{\partial x_i} \right) + \lambda_t \frac{\partial \tilde{u}_k}{\partial x_k} \delta_{ij} \tag{2.33}$$

$$\lambda_t = -2/3 \, \epsilon$$

A similar eddy diffusivity for heat flux can be defined as

$$- \overline{\rho e_I'' u_j''} = \frac{k_t}{C_v} \frac{\partial \tilde{e}_I}{\partial x_j} = \gamma \frac{\epsilon}{Pr_t} \frac{\partial e_I}{\partial x_j} \tag{2.34}$$

$$Pr_t = \frac{C_p \epsilon}{k_t} = .9$$

The constant Prandtl number is based upon a Reynolds analogy, in which the eddy diffusivities of momentum and heat are related.

Upon substituting expressions (2.33) and (2.34) into equations (2.28) through (2.30) and transforming to axi-symmetric coordinates by equations (2.14) to (2.19) the Reynolds-averaged axi-symmetric Navier-Stokes equations may be written as:

$$\frac{\partial}{\partial t} (\bar{U}) + \frac{\partial}{\partial x} (\bar{F}) + \frac{1}{y} \frac{\partial}{\partial y} (y\bar{G}) = \frac{1}{y} \bar{H} \tag{2.35}$$

$$\bar{U} = \begin{bmatrix} \bar{\rho} \\ \bar{\rho}\tilde{u} \\ \bar{\rho}\tilde{v} \\ \bar{\rho}\tilde{E} \end{bmatrix} \qquad \bar{F} = \begin{bmatrix} \bar{\rho}\tilde{u} \\ \bar{\rho}\tilde{u}^2 - \bar{\tau}_{xx} \\ \bar{\rho}\tilde{u}\tilde{v} - \bar{\tau}_{yx} \\ \bar{\rho}\tilde{u}\tilde{E} - \tilde{u}\bar{\tau}_{xx} - \tilde{v}\bar{\tau}_{xy} + \bar{q}_x \end{bmatrix}$$

22

$$\bar{G} = \begin{bmatrix} \bar{\rho}\tilde{v} \\ \bar{\rho}\tilde{u}\tilde{v} - \bar{\tau}_{xy} \\ \bar{\rho}\tilde{v}^2 - \bar{\tau}_{yy} \\ \bar{\rho}\tilde{v}\tilde{E} - \tilde{u}\bar{\tau}_{yx} - \tilde{v}\bar{\tau}_{yy} + \bar{q}_y \end{bmatrix} \qquad \bar{H} = \begin{bmatrix} 0 \\ 0 \\ -\bar{\tau}_{\theta\theta} \\ 0 \end{bmatrix}$$

$$\bar{\tau}_{xx} = -\bar{p} + 2(\tilde{\mu} + \epsilon)\frac{\partial\tilde{u}}{\partial x} + (\tilde{\lambda} + \lambda_t)\{\frac{\partial\tilde{u}}{\partial x} + \frac{1}{y}\frac{\partial}{\partial y}(y\tilde{v})\}$$

$$\bar{\tau}_{xy} = \bar{\tau}_{yx} = (\tilde{\mu} + \epsilon)(\frac{\partial\tilde{u}}{\partial y} + \frac{\partial\tilde{v}}{\partial x})$$

$$\bar{\tau}_{yy} = -\bar{p} + 2(\tilde{\mu} + \epsilon)\frac{\partial v}{\partial y} + (\tilde{\lambda} + \lambda_t)\{\frac{\partial\tilde{u}}{\partial x} + \frac{1}{y}\frac{\partial}{\partial y}(y\tilde{v})\}$$

$$\bar{\tau}_{\theta\theta} = -\bar{p} + 2(\tilde{\mu} + \epsilon)\frac{\tilde{v}}{y} + (\tilde{\lambda} + \lambda_t)\{\frac{\partial u}{\partial x} + \frac{1}{y}\frac{\partial}{\partial y}(y\tilde{v})\}$$

$$\tilde{E} = C_v\tilde{T} + \frac{1}{2}(\tilde{u}^2 + \tilde{v}^2) = \tilde{e}_I + \frac{1}{2}(\tilde{u}^2 + \tilde{v}^2)$$

$$\bar{q}_x = -\gamma(\frac{\tilde{\mu}}{Pr} + \frac{\epsilon}{Pr_t})\frac{\partial\tilde{e}_I}{\partial x} \qquad\qquad \bar{q}_y = -\gamma(\frac{\tilde{\mu}}{Pr} + \frac{\epsilon}{Pr_t})\frac{\partial e_I}{\partial y}$$

A Cebeci-Smith two-layer, equlilibrium model (Refs 42, 43, 44) was chosen to model the eddy viscosity in regions where the flow was expected to be turbulent. That is, in the boundary layer region downstream of the transition from laminar to turbulent flow. The eddy viscosity is assumed to be composed of an inner and outer layer. In both cases the eddy viscosity may be expressed as,

$$\epsilon = \bar{\rho}\ell V\Gamma(s) \tag{2.36}$$

where ℓ and V are appropriate length and velocity scales. In the inner region, Cebeci (Ref 42) gives the length scale for an axi-symmetric boundary layer, with Van Driest's modification as:

$$\ell = k_1 \sqrt{\frac{y_0 + |y_n|}{y_0}} \; y_0 \ln(\frac{y_0 + |y_n|}{y_0}) [1-\exp(-\frac{y_0}{A} \ln(\frac{y_0 + |y_n|}{y_0}))] \tag{2.37}$$

and the velocity scale is

$$V = \ell \left|\frac{\partial u}{\partial y_n}\right| \tag{2.38}$$

where

$k_1 = .40$ (Von Karman's constant)

$A = 26 \dfrac{\mu_w}{\sqrt{\rho_w |\tau_w|}}$

y_n = distance normal to the surface

y_o = body radius

u = velocity component tangent to surface

$\Gamma(s)$ = transition factor

s – distance along surface from leading edge

In the outer region, the length scale is proportional to the two dimensional incompressible displacement thickness.

$$\ell = k_2 \, \delta_1 = k_2 \int_0^\delta \left(1 - \frac{u}{u_{ref}}\right) dy_n \qquad (2.39)$$

$$k_2 = .0168 \qquad \text{(Clauser's constant)}$$

The velocity scale is the reference velocity

$V = u_{ref}$ – velocity tangent to boundary at the edge of the
boundary layer.

A continuous distribution of eddy viscosity is obtained by switching to the outer expression when it is first exceeded by the inner expression. The equation used to model the transition from laminar to turbulent flow is taken from Dhawan and Narashima (Ref 45)

$$\Gamma(s) = 1 - \exp\left(-.412 \, \bar{s}^2\right)$$

$$\bar{s} = (s - s_i)/\Lambda \qquad s_i \leq s \leq s_f \qquad (2.40)$$

$$\Lambda = s\big|_{\Gamma = 3/4} \;-\; s\big|_{\Gamma = 1/4}$$

The locations for turbulence onset (s_i) and fully turbulent flow (s_f) must be known or approximated a priori.

The Cebeci-Smith model has the important advantage of its relative economy compared with the more complex differential equation

24

models. It has been extensively used with good success for attached flows without large adverse pressure gradients. Unfortunately the problem to be considered involves large regions of separated flow caused by highly adverse pressure gradients. The author is not aware of any model which is generally satisfactory for unsteady separated flows. The algebraic model assumes an equilibrium between production and dissipation of the turbulence which is not true in regions of rapid change such as adverse pressure gradients and separated boundary layers. Relaxation and pressure gradient corrections have been used in these regions to improve agreement with experiment but usually require model adjustment for each flow field. Another common correction, intermittency, was not implemented due to its little influence on the flow field and the eventual merger of the downstream boundary layers. Since transition must be modeled, the location and extent of the transition region should be known from experiment or otherwise rationally estimated. Finally, what part of the turbulent spectrum should be modeled when the subject of the calculation is itself a periodic instability must be considered. In essence, this means that the limits over which the turbulent fluctuations are averaged, Equation (2.23), should be appropriate for the problem at hand. If interest is focused on the direct calculation of the flow instability and this is resolvable to a limited extent on the computational grid, the period over which averaging is performed and the eddy viscosity coefficient which models the fluctuating averages should correspond only to the higher frequencies which are not resolvable (Ref 46). The Cebeci-Smith model was adopted as a baseline to provide an approximate representation of the turbulence at a reasonable cost.

Section III

NUMERICAL METHODS

3.1 Body Oriented Coordinate System

Coordinate Transformation to Computational Plane

The governing partial differential equations must be discretized over a finite number of points at which approximate solutions are generated. A body-oriented coordinate system is usually chosen to align the coordinate axes with the body contours in order to simplify the implementation of boundary conditions. Such a grid also provides suitable resolution in regions of rapid change through coordinate grid stretching. The solution algorithm, however, must be on a uniform grid if standard finite difference formulas are to be valid. This is accomplished by transforming the physical coordinates (x,y) to computational coordinates (ξ,η).

If the functions $\xi(x,y)$ and $\eta(x,y)$ and their first partials are continuous and the Jacobian, J, $\neq 0$, then the coordinate transformation is admissible. The following relations may then be obtained by application of the chain rule:

$$\begin{bmatrix} \dfrac{\partial}{\partial x} \\[2ex] \dfrac{\partial}{\partial y} \end{bmatrix} = \begin{bmatrix} \dfrac{\partial \xi}{\partial x} & \dfrac{\partial \eta}{\partial x} \\[2ex] \dfrac{\partial \xi}{\partial y} & \dfrac{\partial \eta}{\partial y} \end{bmatrix} \begin{bmatrix} \dfrac{\partial}{\partial \xi} \\[2ex] \dfrac{\partial}{\partial \eta} \end{bmatrix} \qquad (3.1)$$

and:

$$\begin{bmatrix} \dfrac{\partial}{\partial \xi} \\[2ex] \dfrac{\partial}{\partial \eta} \end{bmatrix} = \begin{bmatrix} \dfrac{\partial x}{\partial \xi} & \dfrac{\partial y}{\partial \xi} \\[2ex] \dfrac{\partial x}{\partial \eta} & \dfrac{\partial y}{\partial \eta} \end{bmatrix} \begin{bmatrix} \dfrac{\partial}{\partial x} \\[2ex] \dfrac{\partial}{\partial y} \end{bmatrix} \qquad (3.2)$$

26

The two Jacobian matrices are inverses and thus the transformation derivatives may be evaluated as:

$$\xi_x = y_\eta / J^{-1}$$

$$\eta_x = -y_\xi / J^{-1}$$

$$\xi_y = -x_\eta / J^{-1} \tag{3.3}$$

$$\eta_y = x_\xi / J^{-1} ,$$

where

$$J^{-1} = x_\xi y_\eta - x_\eta y_\xi = \frac{1}{J} = \frac{1}{\xi_x \eta_y - \xi_y \eta_x} \tag{3.4}$$

Equation (2.35) may be expanded, using equation (3.1) to give

$$\frac{\partial}{\partial t}(U) + \left[\xi_x \frac{\partial F}{\partial \xi} + \frac{1}{y} \xi_y \frac{\partial}{\partial \xi}(yG)\right] + \left[\eta_x \frac{\partial F}{\partial \eta} + \frac{1}{y} \eta_y \frac{\partial}{\partial \eta}(yG)\right] = \frac{1}{y} H \tag{3.5}$$

The equations are usually written in divergence, or conservation law, form, (Refs 47, 48, 49, 50, 51) because of its ability to capture "weak solutions." This is a consequence of the exact cancellation of intercell fluxes, which assures strict conservation of mass, momentum, and energy. Conservation form is most advantageous for flows involving shocks. This form can be shown to satisfy the Rankine-Hugoniot shock jump relations, ensuring correct shock location, strength, and speed. Upon multiplying by

$$J^{-1} y$$

Equation (3.5) may be rewritten as:

$$\frac{\partial}{\partial t} (J^{-1} y U) + \frac{\partial}{\partial \xi} [J^{-1} y \xi_x F + J^{-1} \xi_y y G]$$

$$+ \frac{\partial}{\partial \eta} [J^{-1} y \eta_x F + J^{-1} \eta_y y G] - J^{-1} H \tag{3.6}$$

$$= (\frac{\partial}{\partial \xi} [J^{-1} y \xi_x] + \frac{\partial}{\partial \eta} [J^{-1} y \eta_x]) F + (\frac{\partial}{\partial \xi}[J^{-1}\xi_y] + \frac{\partial}{\partial \eta} [J^{-1}\eta_y]) y G$$

It is not difficult to show that the terms on the right hand side are both identically zero. The remaining source term is a consequence of the ignorable coordinate, Θ, and must remain in the axi-symmetric equations. If the contravariant velocity components

$$U_c = \xi_x u + \xi_y v$$
$$V_c = \eta_x u + \eta_y v \tag{3.7}$$

are defined, the governing equations may be written in a compact form as,

$$\frac{\partial}{\partial t}(U) + \frac{\partial}{\partial \xi}(F) + \frac{\partial}{\partial \eta}(G) = H \tag{3.8}$$

where

$$U = \frac{y}{J} \begin{bmatrix} \rho \\ \rho u \\ \rho v \\ \rho E \end{bmatrix}$$

$$F = \frac{y}{J} \begin{bmatrix} \rho U_c \\ \rho u U_c - \xi_x \tau_{xx} - \xi_y \tau_{xy} \\ \rho v U_c - \xi_y \tau_{yy} - \xi_x \tau_{xy} \\ \rho E U_c + \xi_x b_x + \xi_y b_y \end{bmatrix}$$

$$G = \frac{y}{J} \begin{bmatrix} \rho V_c \\ \rho u V_c - \eta_x \tau_{xx} - \eta_y \tau_{xy} \\ \rho v V_c - \eta_y \tau_{yy} - \eta_x \tau_{xy} \\ \rho E V_c + \eta_x b_x + \eta_y b_y \end{bmatrix}$$

$$H = \frac{1}{J} \begin{bmatrix} 0 \\ 0 \\ -\tau_{\Theta\Theta} \\ 0 \end{bmatrix}$$

28

$$b_x = q_x - u\tau_{xx} - v\tau_{xy}$$

$$b_y = q_y - u\tau_{xy} - v\tau_{yy}$$

$$\tau_{xx} = -p + 2(\mu+\epsilon)\frac{\partial u}{\partial x} + (\lambda+\lambda_t)\{\frac{\partial u}{\partial x} + \frac{1}{y}\frac{\partial}{\partial y}(yv)\}$$

$$\tau_{xy} = \tau_{yx} = (\mu+\epsilon)\{\frac{\partial u}{\partial y} + \frac{\partial v}{\partial x}\}$$

$$\tau_{yy} = -p + 2(\mu+\epsilon)\frac{\partial v}{\partial y} + (\lambda+\lambda_t)\{\frac{\partial u}{\partial x} + \frac{1}{y}\frac{\partial}{\partial y}(yv)\}$$

$$\tau_{\theta\theta} = -p + 2(\mu+\epsilon)\frac{v}{y} + (\lambda+\lambda_t)\{\frac{\partial u}{\partial x} + \frac{1}{y}\frac{\partial}{\partial y}(yv)\}$$

The superscripts for averaged variables have been dropped and partials with respect to x and y in the shear stress terms are evaluated by application of Equation (3.1). For example,

$$\tau_{xy} = (\mu+\xi)\{\frac{\partial u}{\partial \xi}\xi_y + \frac{\partial u}{\partial \eta}\eta_y + \frac{\partial v}{\partial \xi}\xi_x + \frac{\partial v}{\partial \eta}\eta_x\} \tag{3.9}$$

This is the form of the equations used for numerical integration.

Coordinate Generation

Two different approaches were used to generate coordinate systems for the axi-symmetric inlet considered. A popular approach is to map a coordinate system about any arbitrary body such that resulting computational plane is then a unit square. This method has the outstanding advantage that the solution algorithm is independent of any particular geometry. Since both the internal and external flow about the inlet must be computed, the grid must be wrapped about the cowl lip. The resulting C-shaped grid is shown in Figure 2. Thompson's method (Ref 52) was used to generate the grid as a solution to the

29

elliptic system of equations;

$$\nabla^2 \xi = \frac{\partial^2 \xi}{\partial x^2} + \frac{\partial^2 \xi}{\partial y^2} = 0$$

$$\nabla^2 \eta = \frac{\partial^2 \eta}{\partial x^2} + \frac{\partial^2 \eta}{\partial y^2} = T(\xi, \eta) \ (\eta_{xx}^{\ 2} + \eta_{yy}^{\ 2}) \tag{3.10}$$

The forcing function, $T(\xi, \eta)$, which determines coordinate line attraction near the boundaries was given by Knight (Ref 53) and iteratively corrected to maintain a constant step size at the boundaries. This approach was used to generate acceptable flowfield solutions for the upstream inlet. It was abandoned, however, because of several distinct disadvantages. The cowl lip tested experimentally was sharp. To avoid the singularity in the transformation, the lip must be rounded. As the radius of curvature becomes smaller, the transformation derivatives become larger and the allowable time step in the solution algorithm becomes smaller. Any finite radius of curvature also produces a detached lip shock which is not present with a sharp lip at the condition tested experimentally. Also since the total number of η grid lines is the same in both the interior and exterior regions of the inlet, a trade off must be made between the coarse grid exterior to the inlet with a larger truncation error and a very dense interior grid resulting in a lower allowable time step in the solution algorithm. Finally, it is difficult to determine forcing functions which counter the natural tendency of the elliptic system to cluster points about convex surfaces and away from concave surfaces.

A much better approach is to map the physical plane into an L-shaped domain, Figure 3, in which the cowl lip is treated as an interior region. The cowl tip is resolved to within one grid cell and the lip need not be rounded. Such a mesh may be quickly and inexpensively produced. An

Physical Plane

$$\xi = (I-1)\Delta\xi$$

$$\Delta\xi = \frac{1}{(IK-1)}$$

$$I = 1,2,3,\ldots,IK$$

$$\eta = (J-1)\Delta\eta$$

$$\Delta\eta = \frac{1}{(JK-1)}$$

$$J = 1,2,3,\ldots,JK$$

Computational Plane

Fig. 2 C-Grid Coordinate System - Inlet Forebody

Physical Plane

$$\zeta = (I-1)\Delta\xi$$

$$\Delta\xi = \frac{1}{(IK-1)}$$

$$I = 1,2,3,\ldots,IK$$

$$\eta = (J-1)\Delta\eta$$

$$\Delta\eta = \frac{1}{(JK-1)}$$

$$J = 1,2,3,\ldots,JK$$
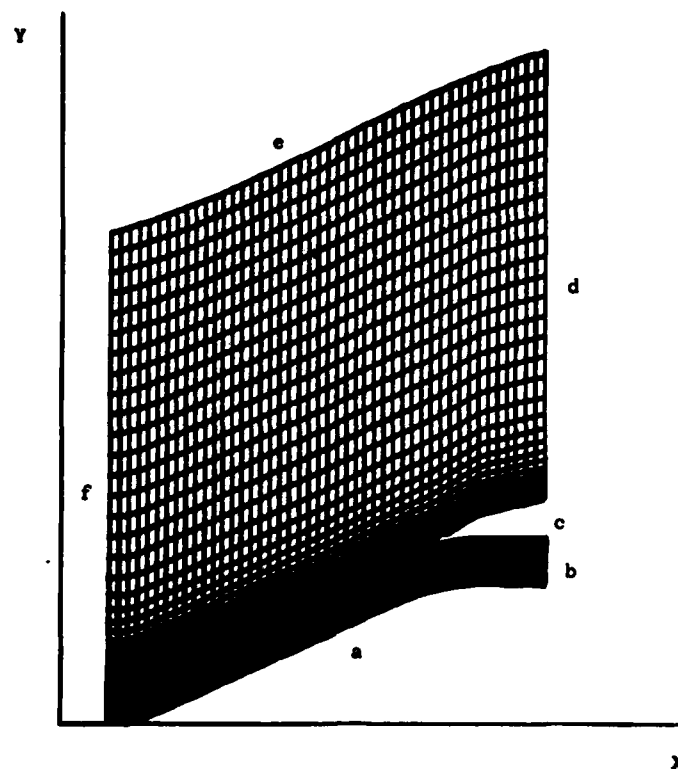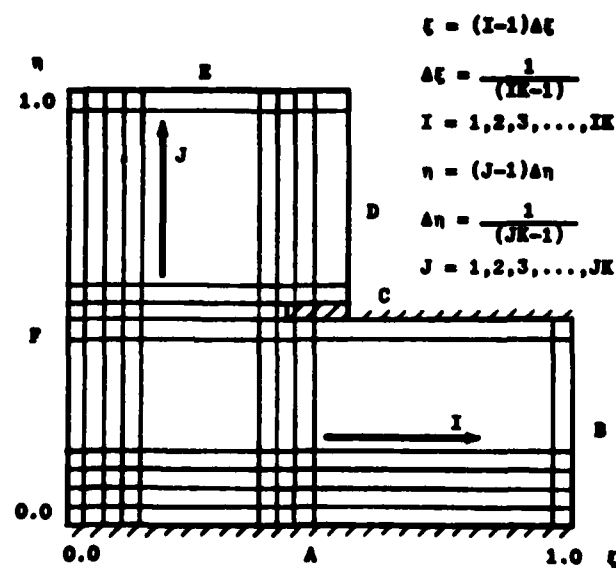
Computational Plane

Fig. 3 L-Grid Coordinate System — Inlet Forebody

algebraic mesh generation scheme was used which clustered points near the centerbody and cowl walls by an exponential stretching, smoothly blended to a constant step size in the center of the duct. The external region of the grid was generated between the inner grid boundary and the specified outer boundary with a region of exponential stretching blended to a constant step size region. First derivative continuity was maintained throughout the grid. The grids generated for the full inlet configurations are shown in Section IV.

Once the grid has been generated, the transformation derivatives are computed and stored once and for all using Equations (3.3). Standard second order accurate difference formulas are used to obtain derivative values. In the interior, central differences are used

$$f_{\xi i,j} = \frac{f_{i+1,j} - f_{i-1,j}}{2\Delta\xi} - \left(\frac{1}{6}\frac{\partial^3 f}{\partial\xi^3}\bigg|_{i,j}\Delta\xi^2\right)$$

$$f_{\eta i,j} = \frac{f_{i,j+1} - f_{i,j-1}}{2\Delta\eta} - \left(\frac{1}{6}\frac{\partial^3 f}{\partial\eta^3}\bigg|_{i,j}\Delta\eta^2\right)$$

$$(3.11)$$

where $f = x,y$ and the leading truncation error term is indicated in parenthesis. On the boundaries, including the cowl lip, transformation derivatives are similarly given by one sided forward,

$$f_{\xi i,j} = \frac{-3f_{i,j} + 4f_{i+1,j} - f_{i+2,j}}{2\Delta\xi} - \left(\frac{1}{3}\frac{\partial^3 f}{\partial\xi^3}\Delta\xi^2\right)_{i,j}$$

$$f_{\eta i,j} = \frac{-3f_{i,j} + 4f_{i,j+1} - f_{i,j+2}}{2\Delta\eta} - \left(\frac{1}{3}\frac{\partial^3 f}{\partial\eta^3}\Delta\eta^2\right)_{i,j}$$

$$(3.12)$$

and backward differences,

$$f_{\xi i,j} = \frac{f_{i-2,j} - 4f_{i-1,j} + 3f_{i,j}}{2\Delta\xi} - \left(\frac{1}{3}\frac{\partial^3 f}{\partial\xi^3}\Delta\xi^2\right)_{i,j}$$

$$f_{\eta i,j} = \frac{f_{i,j-2} - 4f_{i,j-1} + 3f_{i,j}}{2\Delta\eta} - \left(\frac{1}{3}\frac{\partial^3 f}{\partial\eta^3}\Delta\eta^2\right)_{i,j}$$

$$(3.13)$$

33

3.2 Solution Algorithm

MacCormack's Method

MacCormack's explicit finite difference algorithm (Refs 54,55) was chosen for numerical integration of the Navier-Stokes equations (3.8), based upon its proven success in a wide variety of problems. The method provides consistent time accurate resolution for unsteady flows and is noted for its robustness and excellent shock capturing ability.

The method is best illustrated by consideration of a simple example in non-transformed variables. Since multi-dimensional systems of equations may be split into sequences of one-dimensional operators by the method of fractional steps, the scheme may be demonstrated by considering the non-linear set of equations

$$\frac{\partial}{\partial t} (U) + \frac{\partial}{\partial x} (F) = 0 \tag{3.14}$$

where $F = F(U)$ and $U = U(t,x)$ are, in general, vectors. The equation may be discretized in time and space as

$$x = i\Delta x , \qquad t = n\Delta t , \qquad F_i^n = F (U(n\Delta t, i\Delta x))$$

A second order time accurate predictor-corrector algorithm may be written as

$$U_i^{\overline{n+1}} = U_i^n - \Delta t \, \partial_x F_i^n \tag{3.15}$$

$$U_i^{n+1} = U_i^n - \frac{1}{2} \Delta t (\partial_x F_i^n + \partial_x F_i^{\overline{n+1}}) \tag{3.16}$$

which is the modified Euler predictor-corrector method. The notation, $\overline{n+1}$, is used to denote a provisional n+1 time level given by the predictor. MacCormack's algorithm results when the spatial derivatives are alternately given by one sided first order differences

$$U_i^{\overline{n+1}} = U_i^n - \Delta t \, \nabla_x F_i^n \tag{3.17}$$

$$U_i^{n+1} = U_i^n - \frac{1}{2} \Delta t (\nabla_x F_i^n + \Delta_x F_i^{\overline{n+1}}) \tag{3.18}$$

Upon substituting from Equation (3.17), Equation (3.18) may be written as,

$$U_i^{n+1} = \frac{1}{2} [U_i^n + \overline{U_i^{n+1}} - \Delta t \; \Delta_x \; \overline{F_i^{n+1}}] \tag{3.19}$$

The result in a second order accurate in space and time, conditionally stable, procedure of Lax-Wendroff type with effectively central spatial differences. This is shown in Appendix A, which summarizes the difference operators used in MacCormack's algorithm. The scheme is dissipative due to the asymmetry in the differencing and this contributes much to the robustness of the method. Appendix B demonstrates rigorously the second order accuracy of the scheme in which the difference equation generates an approximation to the differential eqn of the form

$$U_t + F_x + O(\Delta t^2) + O(\Delta t \Delta x) + O(\Delta x^2) = 0 \tag{3.20}$$

The Navier-Stokes equations contain second derivatives resulting from the viscous stress terms. These appear in the F and G terms as first derivatives. If the outer differencing of the F and G terms is forward (backward) and the interior derivatives occur in the same variable as the outer derivative, these terms are then evaluated by first order backward (forward) differences. Mixed derivative terms are evaluated by 2nd order central differences for the interior terms. As an example, a component of F having the form

$$F = \mu \left(\frac{\partial u}{\partial y} + \frac{\partial v}{\partial x}\right)$$

is differenced by Equation (3.16) as

$$\overline{U_{i,j}^{n+1}} = U_{i,j}^n + \Delta t \; \nabla_x \; F_{i,j}^n = U_{i,j}^n - \frac{\Delta t}{\Delta x} (F_{i,j}^n - F_{i-1,j}^n) \tag{3.21}$$

with

$$F_{i,j}^n = \mu_{i,j}^n \; (\delta_y \; u_{i,j}^n + \Delta_x \; v_{i,j}^n)$$

$$\tag{3.22}$$

$$F_{i-1,j}^n = \mu_{i-1,j}^n \; (\delta_y \; u_{i-1,j}^n + \Delta_x \; v_{i-1,j}^n)$$

and by Equation (3.19) as

$$U_{i,j}^{n+1} = \frac{1}{2} (U_{i,j}^n + \overline{U_{i,j}^{n+1}} - \Delta t \; \Delta_x \; \overline{F_{i,j}^{n+1}})$$

$$= \frac{1}{2} (U_{i,j}^n + \overline{U_{i,j}^{n+1}} - \frac{\Delta t}{\Delta x} [\overline{F_{i+1,j}^{n+1}} - \overline{F_{i,j}^{n+1}}]) \tag{3.23}$$

with

$$\overline{F_{i+1,j}^{n+1}} = \overline{\mu_{i+1,j}^{n+1}} \; (\delta_y \; \overline{u_{i+1,j}^{n+1}} + \nabla_x \; \overline{v_{i+1,j}^{n+1}})$$

$$\overline{F_{i,j}^{n+1}} = \overline{\mu_{i,j}^{n+1}} \; (\delta_y \; \overline{u_{i,j}^{n+1}} + \nabla_x \; \overline{v_{i,j}^{n+1}}) \; . \tag{3.24}$$

The result is, again, an effectively central, second order accurate

difference approximation to the second derivative terms,

$$\frac{\partial^2 u}{\partial x \partial y} \quad \text{and} \; \frac{\partial^2 v}{\partial x^2}$$

If viscosity is considered constant, Equation (3.23) may be rewritten,

using the notation of Appendix A, as

$$U_{i,j}^{n+1} = U_{i,j}^n - \mu \frac{\Delta t}{2} \delta_y (\nabla_x \; u_{i,j}^n + \Delta_x \; \overline{u_{i,j}^{n+1}})$$

$$- \mu \frac{\Delta t}{2} \nabla_x \Delta_x \; (v_{i,j}^n + \overline{v_{i,j}^{n+1}}) \tag{3.25}$$

in which the structure of the differencing is transparent.

Splitting

For multi-dimensional systems of equations, additional efficiency

may be gained if the equations are split into a sequence of one dimen-

sional operators. The two dimensional equation

$$\frac{\partial}{\partial t} (U) + \frac{\partial}{\partial x} (F) + \frac{\partial}{\partial y} (G) = 0 \tag{3.26}$$

may be advanced in time, using the method of fractional steps (Refs 54,

55, 56, 57, 58) by the symmetric operator sequence:

$$U^{n+1} = L_y \; (\frac{\Delta t}{m})^{m/2} \; L_x(\Delta t) \; L_y(\frac{\Delta t}{m})^{m/2} \; U^n \tag{3.27}$$

In detail, this becomes

$$U_{i,j}^{*} = L_y \left(\frac{\Delta t}{m}\right)^{m/2} U_{i,j}^{n}$$

$$U_{i,j}^{**} = L_x (\Delta t) U_{i,j}^{*}$$

$$U_{i,j}^{n+1} = L_y \left(\frac{\Delta t}{m}\right)^{m/2} U_{i,j}^{**}$$

The L_y operator updates the one-dimension equation

$$\frac{\partial}{\partial t}(U) + \frac{\partial}{\partial y}(G) = 0 \tag{3.28}$$

as

$$U_{i,j}^{\bar{*}} = U_{i,j}^{n} - \frac{\Delta t}{m} \nabla_y G_{i,j}^{n}$$

$$U_{i,j}^{*} = \frac{1}{2} (U_{i,j}^{n} + U_{i,j}^{\bar{*}} - \frac{\Delta t}{m} \Delta_y G_{i,j}^{\bar{*}}) \tag{3.29}$$

similarly L_x approximates

$$\frac{\partial}{\partial t}(U) + \frac{\partial}{\partial x}(F) = 0 \tag{3.30}$$

as

$$U_{i,j}^{\overline{**}} = U_{i,j}^{*} - \Delta t \nabla_x F_{i,j}^{*} \tag{3.31}$$

$$U_{i,j}^{**} = \frac{1}{2} (U_{i,j}^{*} + U_{i,j}^{\overline{**}} - \Delta t \Delta_x F_{i,j}^{\overline{**}})$$

Splitting is efficient when, because of stability, the allowable time
step in one direction is much smaller than the other. That is, where m,
the largest integer ratio of allowable time steps in the L_x and L_y
operators, is greater than two. The solution may be advanced several
times in one operator before the other need be advanced. This sit-
uation typically occurs in the boundary layer region, where in order
to resolve the large flow gradients normal to the wall

$$\Delta y/\Delta x << 1$$

Lomax (Ref 58) has shown that if a symmetric operator sequence is
followed, the split algorithm retains full second order temporal and

spatial accuracy. This is outlined in Appendix C.

Computational Coordinates

MacCormacks method, as outlined, may now be applied directly to the transformed Navier-Stokes Equations (3.8). The solution is then advanced in time by the operator sequence.

$$U_{i,j}^{n+1} = L_\eta(\Delta t_\eta) \; L_\xi(\Delta t_\xi) \; L_\eta(\Delta t_\eta) \; U_{i,j}^{n} \qquad (3.32)$$

where $m = \dfrac{\Delta t_\xi}{\Delta t_\eta} \equiv 2$, $\xi = (i-1)\Delta\xi$, $\eta = (j-1)\Delta\eta$, $t = n\Delta t_\xi$

and $i = 1,2,3,\ldots,ik \qquad j = 1,2,3,\ldots,jk$

The L_η operator,

$$U_{i,j}^{*} = L_\eta(\Delta t_\eta) \; U_{i,j}^{n} \qquad (3.33)$$

updates the radial split equation

$$\frac{\partial}{\partial t}(U) + \frac{\partial}{\partial \eta}(G) = H \qquad (3.34)$$

as

$$U_{i,j}^{\bar{*}} = U_{i,j}^{n} - \frac{\Delta t_\eta}{\Delta \eta}(G_{i,j}^{n} - G_{i,j-1}^{n}) + \Delta t_\eta \; H_{i,j}^{n}$$

$$U_{i,j}^{*} = \frac{1}{2}[U_{i,j}^{n} + U_{i,j}^{\bar{*}} - \frac{\Delta t_\eta}{\Delta \eta}(G_{i,j+1}^{\bar{*}} - G_{i,j}^{\bar{*}}) + \Delta t_\eta \; H_{i,j}^{*}] \qquad (3.35)$$

The L_ξ operator,

$$U_{i,j}^{**} = L_\xi(\Delta t_\xi) \; U_{i,j}^{*} \qquad (3.36)$$

updates the axial split equation

$$\frac{\partial}{\partial t}(U) + \frac{\partial}{\partial \xi}(F) = 0 \qquad (3.37)$$

as

$$U_{i,j}^{\overline{**}} = U_{i,j}^{*} - \frac{\Delta t_\xi}{\Delta \xi}(F_{i,j}^{*} - F_{i-1,j}^{*})$$

$$U_{i,j}^{**} = \frac{1}{2}[U_{i,j}^{*} + U_{i,j}^{\overline{**}} - \frac{\Delta t_\xi}{\Delta \xi}(F_{i+1,j}^{\overline{**}} - F_{i,j}^{\overline{**}})] \qquad (3.38)$$

38

The method carries through in a straight-forward manner, with the differencing now being either forward, backward, or central in the computational variables ξ, η. However, the interior derivatives in the source term, H, are approximated with central differences in both ξ and η for both the predictor and corrector in the radial equation.

Stability

MacCormack's method is conditionally stable with a corresponding restriction on the allowable time step. Stability of a given algorithm is difficult to ascertain. The most successful approach to date is that of Von Neumann (Refs 50,51). The governing equations must be linearized and the coefficient matrices assumed to be locally constant or slowly varying. Consistent with the linearized form of the equations, the growth or decay of each Fourier component is examined independently. The approach is to assume a solution of the form

$$V^n_{i,j} = \phi^n(k_\xi, k_\eta) e^{I(k_\xi i\Delta\xi + k_\eta i\Delta\eta)} \tag{3.39}$$

where

$I = \sqrt{-1}$

$\phi^n(k_\xi, k_\eta)$ - amplitude function at nth time level

k_ξ - wave number in ξ

k_η - wave number in η

A difference equation may be obtained by applying the two step MacCormack predictor-corrector to the linearized equations. Provisional $\overline{(\ )^{n+1}}$ values may be eliminated in the corrector by substitution from the predictor. Equation (3.39) is then substituted into the resulting corrector equation. Considerable manipulation will lead to an equation of the form

$$\phi^{n+1}(k_\xi, k_\nu) = G(k_\xi, k_\eta) \, \phi^n(k_\xi, k_\eta) \tag{3.40}$$

from which

$$\phi^n(k_\xi, k_\eta) = \left[G(k_\xi, k_\eta) \right]^n \phi^0(k_\xi, k_\eta) . \tag{3.41}$$

For a fixed time, $t = n\Delta t$, as the time step is refined, the iteration

number approaches the limit

$$\lim_{\Delta t \to 0} \left(\frac{t}{\Delta t} \right) = \infty$$

Thus, for stability, the matrix norm of the amplification matrix, G, must

remain bounded,

$$||G^n|| \leq M \text{ as } n \to \infty.$$

It can be shown that a necessary condition is that

$$|\lambda| \leq 1 + O(\Delta t), \tag{3.42}$$

where λ is the largest eigenvalue of the amplification matrix for all

possible combinations of wave number k_ξ, k_η. This is frequently termed

the spectral radius.

Because the equations are solved in factored or split form, the

stability of the L_η and L_ξ operators may be ascertained independently.

Upon rewriting the non-conservative form of the governing equations (3.5)

in the more convenient variables

$$V = \begin{bmatrix} \rho \\ u \\ v \\ p \end{bmatrix} \tag{3.43}$$

and linearizing, the axial split equation becomes

$$\frac{\partial V}{\partial t} + A \frac{\partial V}{\partial \xi} + C \frac{\partial^2 V}{\partial \xi^2} + E_1 \frac{\partial \left(\frac{\partial V}{\partial \eta} \right)}{\partial \xi} + F_1 V = 0 \tag{3.44}$$

and the radial is

$$\frac{\partial V}{\partial t} + B \frac{\partial V}{\partial \eta} + D \frac{\partial^2 V}{\partial \eta^2} + E_2 \frac{\partial \left(\frac{\partial V}{\partial \xi} \right)}{\partial \eta} + F_2 V = 0 \tag{3.45}$$

A, B, C, D, E_1, E_2, F_1, F_2 are 4x4 constant matrices which are coefficients

40

of the inviscid, diffusive, mixed derivative and source terms respectively. F_1V and F_2V appear because of the axi-symmetric form of the equations and do not appear in the two dimensional case. Richtmyer and Morton (Ref 50: Sec 8.4) demonstrate that stability is unaffected by the source or lower order terms so they may be safely ignored. Consequently, stability conditions for the axisymmetric equations are the same as the two dimensional stability bounds.

MacCormack and Baldwin (Ref 55) have analyzed separately the stability of the inviscid, diffusive and mixed derivative parts of Equations (3.44) and (3.45) by the von Neumann method for the non-transformed equations. The dominant stability component is the inviscid limit, with smaller viscous corrections.

$$\Delta t_{\xi,\eta} = \frac{1}{\frac{1}{\Delta t_{inv}} + \frac{1}{\Delta t_{diff}} + \frac{1}{\Delta t_{md}}} \tag{3.46}$$

The algebra involved is quite lengthy and need not be detailed here. What is of interest are corresponding stability restrictions for the transformed equations. Since the transformed equations are identical in form with those considered by MacCormack, Appendix D demonstrates how similar stability restrictions may be generalized for the transformed equations. The maximum allowable time step is then

$$\Delta t_\xi = 2 \, \alpha \, \min_{i,j} \left[\min_{i,j} (\Delta t_{\eta_{i,j}}), \frac{1}{2} \min_{i,j} (\Delta t_{\xi_{i,j}}) \right]$$

$$\Delta t_\eta = \alpha \, \min_{i,j} \left[\min_{i,j} (\Delta t_{\eta_{i,j}}), \frac{1}{2} \min_{i,j} (\Delta t_{\xi_{i,j}}) \right] \tag{3.47}$$

where

$\alpha = 0. \rightarrow 1.0$ (usually .9)

$$\Delta t_{\xi i,j} = \left. \frac{\Delta S_\xi}{|U_\xi| + c + [\frac{2\Theta_1}{\Delta S_\xi} + \frac{\Theta_2}{\Delta S_\eta}]/\rho} \right|_{i,j} \tag{3.48}$$

41

$$\Delta t_{\eta i,j} = \frac{\Delta S_\eta}{|V_\eta| + c + [\frac{2\theta_1}{\Delta S_\eta} + \frac{\theta_2}{\Delta S_\eta}]/\rho} \Bigg|_{i,j}$$ (3.49)

Also,

$$\Delta S_\xi = \frac{\Delta \xi}{\sqrt{\xi_x^2 + \xi_y^2}} \qquad\qquad \Delta S_\eta = \frac{\Delta \eta}{\sqrt{\eta_x^2 + \eta_y^2}}$$

$$U_\xi = \frac{U_c}{\sqrt{\xi_x^2 + \xi_y^2}} \qquad\qquad V_\eta = \frac{V_c}{\sqrt{\eta_x^2 + \eta_y^2}}$$ (3.50)

$$\theta_1 = \max \left[|2(\mu+\epsilon) + (\lambda+\lambda_t)|, \ \gamma(\frac{\mu}{Pr} + \frac{\epsilon}{Pr_t}) \right]$$

$$\theta_2 = \sqrt{|(\mu+\epsilon)(\lambda+\lambda_T)|}$$

This same stability condition was given by Knight (Ref 53) in his solution for the two-dimensional transformed equations. For many viscous flows the time-step restriction in the L_η operator is quite severe. The equations become very stiff in the sense that the allowable time step is much smaller than what is required to accurately resolve the temporal dynamics of the flow. It is the desire to avoid this restriction that motivates the use of an implicit method in which spatial derivatives are evaluated at the n+1 time level with unconditional stability. References (59), and (60) are representative of current implicit methods. The basic explicit method was used for the present work, however, because of its robustness, its time accurate resolution, and its easy implementation on a vector processor.

Numerical Damping

MacCormack's algorithm is a "shock-capturing" technique in which a discontinuity such as a shock must be resolved over several mesh points rather than the order of a mean free path length in which it physically occurs. A solution in this region will normally exhibit non-physical

42

oscillations before and after the shock. At best, these are unappealing and they may lead to numerical instability. MacCormack (Ref 55) has introduced a fourth-order smoothing term which is effective in damping the shock induced oscillations and negligible elsewhere. Damping is incorporated into the L_ξ operator, equation (3.38) as

$$F^*_{i,j} \leftarrow F^*_{i,j} + D^*_{i,j}$$

$$F^*_{i-1,j} \leftarrow F^*_{i-1,j} + D^*_{i-1,j}$$

$$\overline{F^{**}_{i+1}} \leftarrow \overline{F^{**}_{i+1,j}} + \overline{D^{**}_{i+1,j}}$$

$$\overline{F^{**}_{i,j}} \leftarrow \overline{F^{**}_{i,j}} + \overline{D^{**}_{i,j}}$$

(3.51)

where

$$D^*_{i,j} = \beta(U^*_{c_{i,j}} + \sqrt{\xi^2_{x_{i,j}} + \xi^2_{y_{i,j}}} \; c^*_{i,j}) \frac{\left|p^*_{i+1,j} - 2p^*_{i,j} + p^*_{i-1,j}\right|}{(p^*_{i+1,j} + 2p^*_{i,j} + p^*_{i,j})}$$

$$\times (U^*_{i+1,j} - U^*_{i,j})$$

$$\overline{D^{**}_{i+1,j}} = \beta(U^{\overline{**}}_{c_{i+1,j}} + \sqrt{\xi^2_{x_{i+1,j}} + \xi^2_{y_{i,j}}} \; \overline{c^{**}_{i+1,j}}) \frac{\left|\overline{p^{**}_{i+2,j}} - 2\overline{p^{**}_{i+1,j}} + \overline{p^{**}_{i,j}}\right|}{(\overline{p^{**}_{i+2,j}} + 2\overline{p^{**}_{i+1,j}} + \overline{p^{**}_{i,j}})}$$

$$\times (\overline{U^{**}_{i+1,j}} - \overline{U^{**}_{i,j}}) \quad (3.52)$$

$\beta = 0.0 \rightarrow 5.0$ (usually $1.0 \rightarrow 2.0$)

The net effect is an eddy viscosity term of the form

$$\beta \, \Delta t \, \Delta \xi^3 \frac{\partial}{\partial \xi} \left[\frac{U_c + \sqrt{\xi^2_x + \xi^2_y} \; c}{4p} \left| \frac{\partial^2 p}{\partial \xi^2} \right| \frac{\partial U}{\partial \xi} \right] \quad (3.53)$$

added to the difference Equation (3.38). Damping is similarly incorporated into the L_η operator, Equation (3.35).

43

3.3 Boundary and Initial Condition Implementation

Boundary Conditions

Boundary conditions must be updated after each pass through the predictor and corrector for each operator. Referring to Figure (3), they may be classified in several different categories:

Solid wall - A, C, (and B for no mass flow through the nozzle) ,

Inflow - F ,

Outflow - B, D ,

Outer Boundary - E ,

Centerline - A, ahead of centerbody.

Solid Wall Boundary Conditions

The velocity components are set by the no-slip condition as

$$u = v = 0 . \tag{3.54}$$

Temperature is assumed to be the adiabatic wall temperature specified from the free stream condition as

$$T_w = (T_{aw})_L \left[1 - \Gamma(s)\right] + (T_{aw})_{TB} \, \Gamma(s) \tag{3.55}$$

where

$$(T_{aw})_L = T_\infty + \sqrt{Pr} \, \frac{u_\infty^2}{2C_p}$$

$$(T_{aw})_{TB} = T_\infty + \sqrt[3]{Pr} \, \frac{u_\infty^2}{2C_p}$$

A compatibility relation is used to update the wall static pressure by finding the normal component of the two momentum equations at the wall. After applying the no-slip condition and neglecting the shear stress terms by order of magnitude considerations, the compatiblity condition becomes

$$\frac{\partial p}{\partial n} = \left[\left(\frac{\partial p}{\partial \xi} \xi_x + \frac{\partial p}{\partial \eta} \eta_x \right) \hat{i} + \left(\frac{\partial p}{\partial \xi} \xi_y + \frac{\partial p}{\partial \eta} \eta_y \right) \hat{j} \right] \cdot \left[\frac{\eta_x \hat{i} + \eta_y \hat{j}}{\sqrt{\eta_x^2 + \eta_y^2}} \right] = 0 \tag{3.56}$$

This may be discretized (on the centerbody, for example) as

$$\Delta_\eta P_{1,1} = -\left[\frac{\xi_x \eta_x + \xi_y \eta_y}{\eta_x^2 + \eta_y^2}\right]_{1,1} \delta_\xi P_{1,2} \qquad (3.57)$$

to update the wall pressure from the previously computed values at neighboring interior points. Once u, v, T, and p are known, all other variables may be computed from these known values.

Inflow Conditions

The inflow boundary is specified to be the unperturbed freestream condition:

$$\begin{bmatrix} u \\ v \\ T \\ P \end{bmatrix} = \begin{bmatrix} u_\infty \\ 0 \\ T_\infty \\ P_\infty \end{bmatrix} \qquad (3.58)$$

Since the flow is supersonic, there is no downstream influence on the inflow boundary. Some care must be taken in the placement of the upstream boundary to ensure the freestream condition is valid. In particular, the upstream boundary should be well ahead of the most forward travel of the normal shock during the buzz cycle or the shock will reflect off the boundary.

Outflow Boundary Conditions

The no-change or zeroth order extrapolation was used to specify the outflow based upon the computed interior values as follows

$$\frac{\partial}{\partial \xi} V = 0 \quad , \quad V = \begin{bmatrix} u \\ v \\ p \\ e_I \end{bmatrix} \qquad (3.59)$$

Using 1st order one sided differences

$$\nabla_\xi \, V_{1,jk} = 0 \qquad\qquad (3.60)$$

The flow at the downstream boundaries is also supersonic except in the boundary layer regions. As a consequence of the domain of dependence in supersonic flow, the downstream boundary has no effect upon the interior of the flow.

The Outer Boundary

The outer radial boundary was placed such that the shock would exit through the outflow boundary in both the steady state and buzz cases. The outer boundary would then be set as the unperturbed freestream value. However, during its forward travel, the strong normal shock could briefly impinge on the upper boundary and reflect into the domain. To avoid this problem, a no-reflection condition was used which allowed the shock to exit without reflection and otherwise recovered the freestream value.

Flow conditions on the outer boundary are extrapolated from the interior along the outward running characteristic as

$$\frac{\partial}{\partial \mu} V = 0 \quad , \quad V = \begin{bmatrix} u \\ v \\ p \\ e_I \end{bmatrix} \qquad\qquad (3.61)$$

This equation is strictly valid only for two dimensional, inviscid, supersonic, steady, isentropic flow in a simple wave region in which there is no change in the inward-running characteristic. Along the outward-running characteristic then, the flow properties remain constant. This relation will also be valid for axi-symmetric flow at large radius and additionally has proven to be a reliable boundary condition for more general flows as shown by Roache (Ref 51: 282).

Referring to Figure 4, the condition is implemented as follows:

(1.) compute the outward running characteristic orientation at the grid point (i,jk), from the flow angle and Mach angle

$$\theta = \tan^{-1}(\frac{v}{u})_{i,jk}$$

$$\alpha = \tan^{-1}(\frac{1}{\sqrt{M^2-1}})_{i,jk}$$

(2.) extrapolate backward to find the intersection with the line $\eta(jk-1) = $ const as a solution of the equations

$$y_c = y(L, jk-1) - \frac{\Delta y}{\Delta x}(x(L, jk-1) - x_c)$$

$$y_c = y(i,jk) - \tan(\alpha+\theta)(x(i,jk) - x_c)$$

(3.) linearly interpolate along arc length between known interior grid points along $\eta(jk-1)$ Line,

$$V(i,jk) = V(x_c, y_c) = V(L-1, jk-1) + \frac{s}{\Delta s}(V(L,jk-1) - V(L-1,jk-1))$$

$$(3.62)$$

where

$$s = \sqrt{[x_c-x(L-1,j-1)]^2 + [y_c-y(L-1,j-1)]^2}$$

$$\Delta s = \sqrt{\Delta x^2 + \Delta y^2}$$
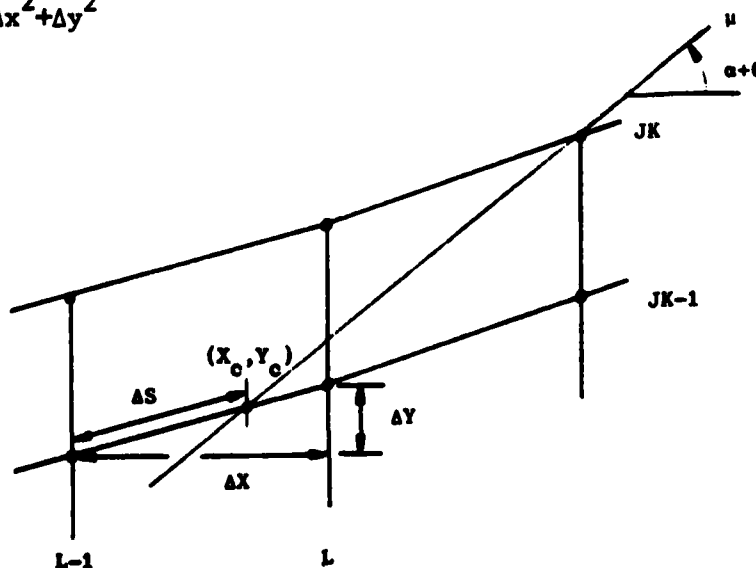
Fig. 4 Characteristic Boundary Condition Implementation

47

Centerline Boundary Conditions

For an axi-symmetric flow, along the centerline a symmetry condition must exist:

$$\frac{\partial}{\partial y} V = 0 \qquad V = \begin{bmatrix} u \\ p \\ e_I \end{bmatrix} \qquad (3.63)$$

and

$$v = 0$$

This is implemented as a one sided difference in the transformed variables as,

$$\Delta_\eta V_{I,1} = 0 \qquad (3.64)$$

Initial Conditions

The solution procedure requires that some initial flow field be specified. This is then integrated foward in time to a steady state which, if it exists, is independent of whatever initial conditions are specified. The situation is less clear for the unsteady cases considered. A purely periodic solution would be expected to be independent of initial conditions as well. The buzz phenomenon is quasi-periodic with a definite period produced by the dominant lower frequencies but not repeatable due to the superposition of non-commensurable higher frequency components. A solution in this case is not necessarily independent of the specified initial conditions. This is especially true when only a few cycles are computed and the flow has several possible modes.

Several different types of initial conditions were used for the cases presented in Section IV. These are briefly outlined below.

Near-Critical Steady

Upstream flow conditions (from inflow boundary to some distance

downstream of cowl lip) were specified as uniform freestream flow. Down-
stream conditions were taken from one dimensional flow relationships
based upon area ratio, with an assumed location of an ideal normal shock
in the diffuser.

Unstable Subcritical With Mass Through-Flow

Here the converged steady state solution was used as initial condi-
tion for the subcritical flow with an impulsive decrease in the downstream
throat area.

Unstable Subcritical With No Mass Through-Flow

Upstream flow conditions were taken from the previous unsteady results
in which the normal shock has been forced from the diffuser. Within the
diffuser, a no flow condition was imposed $(u,v=0)$ Static pressure was
fixed at the experimentally determined point of maximum pressure recovery
before the onset of buzz. Temperature was also fixed uniformly at the
adiabatic wall temperature, which is, of course, close to the stagnation
temperature.

3.4 Implementation on a Vector-Processor (Cray 1-S)

All calculations presented in this report were done on the Cray 1-S
at the Air Force Weapons Laboratory, Kirtland Air Force Base, Albuquerque,
New Mexico. Access was through the Scientific and Management Network
(SAMNET) subsystem of the ARPA Network (ARPANET) and also by long dis-
tance commercial lines dial up.

The Cray 1-S is known as a vector processor and uses a pipeline
architecture to dramatically increase the execution rate of a given

program. An interesting non-technical introduction to the subject of vector processors and "super computers" has recently been given by Levine (Ref 61). In essence, a pipeline architecture continously feeds new operands into the "pipeline" in which subsequent elements of a vector operation immediately follow the initial element as it is broken down into segments and proceeds to completion. After the time required for the initial operand to pass through the pipeline, $T_{startup}$, a new result will be generated every clock period, T_o, thereafter. A vector operation of length N will then execute in the time, (Ref 62),

$$T_{tot} = T_{startup} + N\ T_o \tag{3.65}$$

The Cray 1-S has a peak execution rate in excess of 100 million floating point operations per second (MFLOPS).

Vectorization is automatically done by the FORTRAN compiler (Ref 63: Chapter 4) if the structure of the code is such that vectorization is not inhibited. The Cray compiler vectorizes the innermost do loop in which the vector length is equal to the difference between starting and stopping values of that loop index. Vectorization is inhibited by:

      (a)   Recursive relationships in the inner loop index ,

      (b)   Subscripts which are not constant integer increments
             of the loop index ,

      (c)   GO TO, IF, Call or other logical call statements ,

occuring in the innermost loop. An efficient vectorized code requires vectorizable do loops with a long vector length so that execution time is not dominated by the startup time. The execution rate approaches an asymptotic limit near integer multiples of the vector register length of sixty four.

MacCormack's explicit algorithm is easily vectorized and this has

been done for the present code. Vector length was set by the i variable corresponding to the ξ coordinate. The minimum vector length is then near fifty and the maximum over two hundred. A common measure of the efficiency of a given algorithm on a given computer is the rate of data processing

$$RDP = \frac{(CPU \ Time)}{(\#Grid \ Points)(\#Iterations)} \ . \tag{3.66}$$

In the present case, a data processing rate per operator of

$$(RDP)_{oper} = 1.166 \times 10^{-5} \ sec$$

has been achieved. This is in good agreement with the results reported by other users of vectorized explicit codes on the Cray 1-S, and Cyber 203, (Refs 28,64).

It should be noted that the execution rate of the vectorized code on the Cray is nearly thirty times faster than the rate on the Wright-Patterson AFB Cyber 170-750. The Cray is five times faster in the scalar mode and an additional factor of six results from the vectorization. Because of the large difference in the time step necessary for stability and high frequency resolution compared with the fundamental period of the oscillation, the computation time is extensive. For the full length inlet, central processor time is in excess of one hour per buzz cycle. Additionally, the core memory used with the Cray is well in excess of that available on the Cyber. The use of the Cray has been an essential element in the successful completion of this work.

51

Section IV

DISCUSSION OF RESULTS

4.1 Experimental Test Description and Results

Experimental Apparatus

The experimental work of Nagashima, Obokata and Asanuma (Ref 1)
was chosen as the basis for numerical comparison. At the time the
computational effort was begun, this appeared to offer the most complete
data set available. In order to understand the numerical results, it
is necessary to consider in some detail the experimental test.

An external compression axi-symmetric inlet was tested at zero
and three degrees angle of attack in a supersonic blow-down wind
tunnel. The test section Mach number was fixed at a value of two.
From the reported data, settling chamber total pressure was determined
to be three atmospheres. Total temperature was assumed to be the
standard reference temperature of 15°C. Reynolds number based on the
model diameter of 6 cm was then set at 2.35×10^6. Run time was
350 seconds at three atmospheres.

A cross sectional view of the inlet model is presented in Figure
5. The length of the inlet cowl was 63.5 cm with an L/D ratio of roughly
15.88. The centerbody half angle was 25°. Three different combinations
of spacers were used to vary the position of the centerbody with
respect to the cowl. These are identified in Ref (1) as spacers A, B
and C. Only spacer A was considered for numerical comparison because
the majority of the reported data was for this case. The forebody
geometry for spacer A is shown in Figure 6 and Table 1 tabulates the geo-
metric coordinates of the centerbody and cowl. A D.C. motor was used to

52
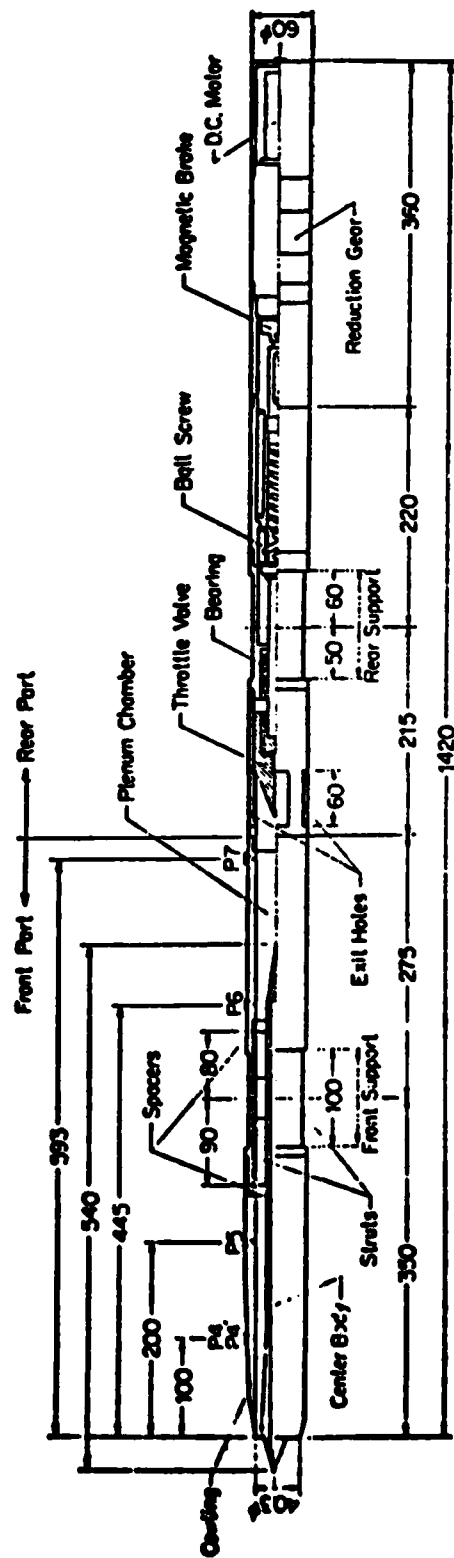
Fig. 5 Experimental Test Model (from Ref 1)
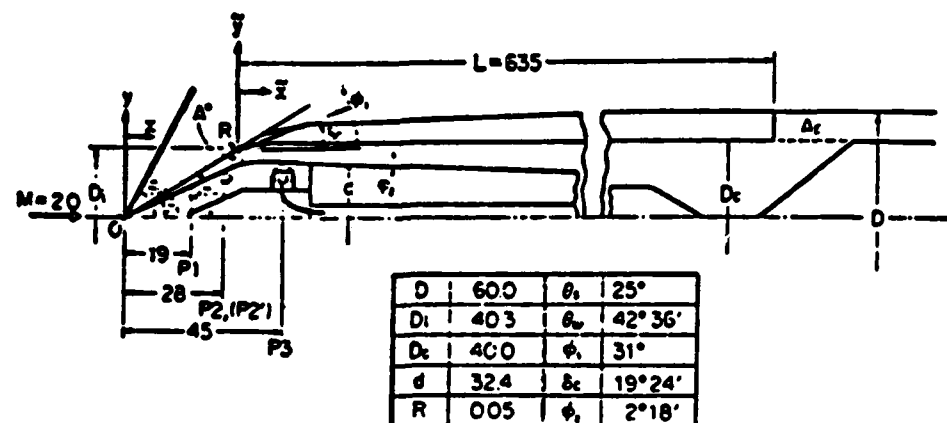
Fig. 6   Inlet Model Characteristics (from Ref 1)

Centerbody Geometry (mm)

X	Y
0.0	0.0
30.0	13.989
30.05	14.215
31.0	14.428
31.5	14.627
32.0	14.813
32.5	14.986
33.0	15.147
33.5	15.296
34.0	15.433
34.5	15.558
35.0	15.672
35.5	15.774
36.0	15.866
36.5	15.946
37.0	16.015
37.5	16.074
38.0	16.122
38.5	16.159
39.0	16.185
39.5	16.201
40.0	16.206
40.927	16.188
240.0	8.384
250.0	8.0
477.805	8.0
540.0	0.0

Inner Cowl Wall Geometry (mm)

X	Y
0.0	20.164
0.5	20.340
1.0	20.508
1.5	20.659
2.0	20.796
2.5	20.917
3.0	21.016
3.5	21.114
4.0	21.191
4.5	21.254
5.0	21.303
5.5	21.337
6.0	21.358
6.5	21.365
120.0	21.365
210.0	20.0

Outer Cowl Wall Geometry (mm)

X	Y
0.0	20.164
6.384	24.0
20.0	27.0
120.0	30.0

$$X = \tilde{X} + 32.805$$

Table 1   Inlet Model Coordinates

control the position of a throttle valve in order to vary the exit area. This area could then be varied continuously within the throttle ratio limits.

$$TR = A_e/A_c = 0 \rightarrow 2.41 \qquad (4.1)$$

where

A_c - upstream capture area at cowl lip

A_e - exit area of holes located along side walls of cowling

(not the minimum or choking area)

Instrumentation

The model was instrumented with seven static pressure probes of strain gauge type. Two were placed on the cone surface (p_1, p_2) and one at the throat (p_3). Four additional probes were placed within the diffuser, before (p_4, p_5) and after (p_6) the diffuser strut, and in the plenum chamber (p_7). Probe locations are shown in Figures 5 and 6. Flow visualization of the exterior flow field was provided by high speed schlieren photography at 5600 frames/sec. A power spectral analyser was used to provide Fourier analysis data of the unsteady pressure traces. No other flow field information was available.

Experimental Results

Spacers A, B, and C were tested for a variety of throttle ratios corresponding to supercritical, critical, and subcritical flow conditions. Attention will be restricted to spacer A with which numerical comparisons will be made. For this configuration, the angle between the centerbody apex and the cowl tip was 31.6°. This value corresponded to a design Mach number of near four, at which the oblique conical

shock impinges upon the cowl lip.

At the test condition, Mach two, the flow was reported to be steady for throttle ratios (TR) greater than 1.14. Pressures corresponding to several supercritical-critical conditions are shown in Figure 7. Pressure rise within the duct was reported by the authors to be smooth, indicating the presence of a shock train due to shock-boundary layer interaction rather than a simple normal shock. A schlieren picture of the external shock structure is available in Figure 8.

Further reduction in the throttle area initiated the onset of the buzz phenomenon associated with the subcritical regime. This is characterized by violent pressure oscillations within the duct and large amplitude shock movement on the centerbody. Typical pressure traces are shown in Figure 9 and the corresponding schlieren pictures are presented in Figures 11 and 12.

Referring to Figures 9 and 10, there were apparently two distinct buzz regimes. At high values of subcritical throttle ratio, the pressure traces exhibited a dominant frequency near the fundamental mode upon which much higher frequency harmonics were superposed in an erratic manner. The shock wave movement and the pressure traces at the front and back ends of the inlet were step-like in nature. Interior to the duct, the wave form was more sinusoidal. This organized pattern did not hold near the throat where the pressure trace became highly irregular. The lower leg of the bow shock was also observed to oscillate with a low amplitude high frequency motion secondary to its primary motion.

As the throttle ratio was further decreased, the dominant frequency suddenly shifted to a value three times the fundamental with

56
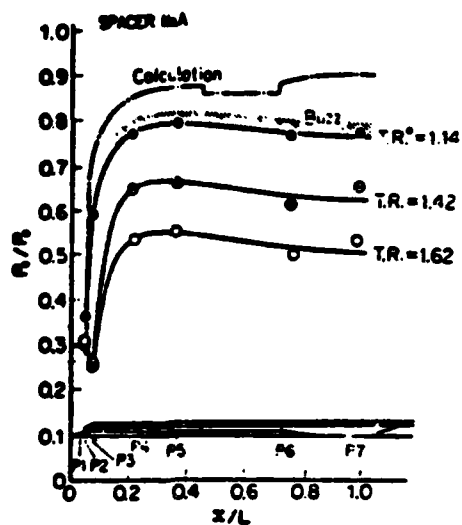
Fig. 7   Axial Distribution of Static Pressure
         (from Ref 1)

Fig. 8   Shock Structure on Forebody, Steady Flow
         TR=1.42 (from Ref 1)
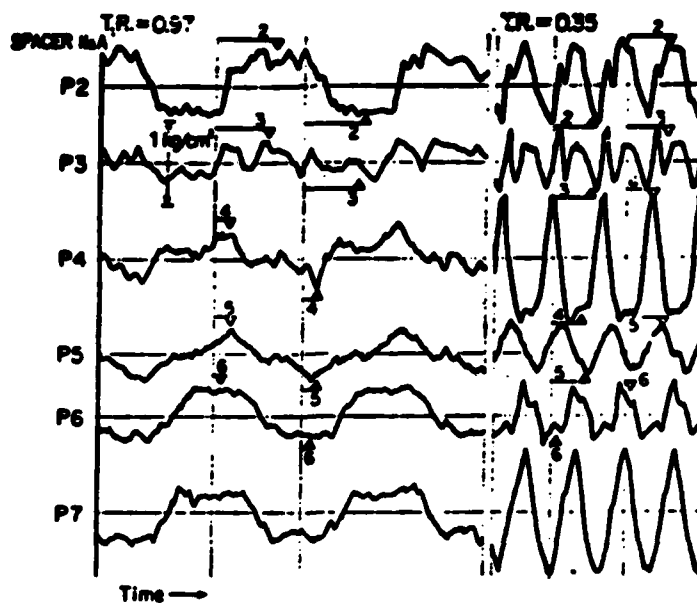
Fig. 9 Experimental Pressure Fluctuation (from Ref 1)
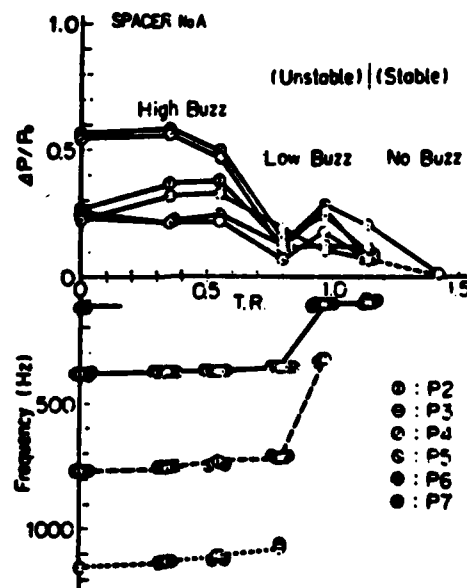
Fig. 10 Amplitude and Frequency Characteristics of
Pressure Oscillations (from Ref 1)
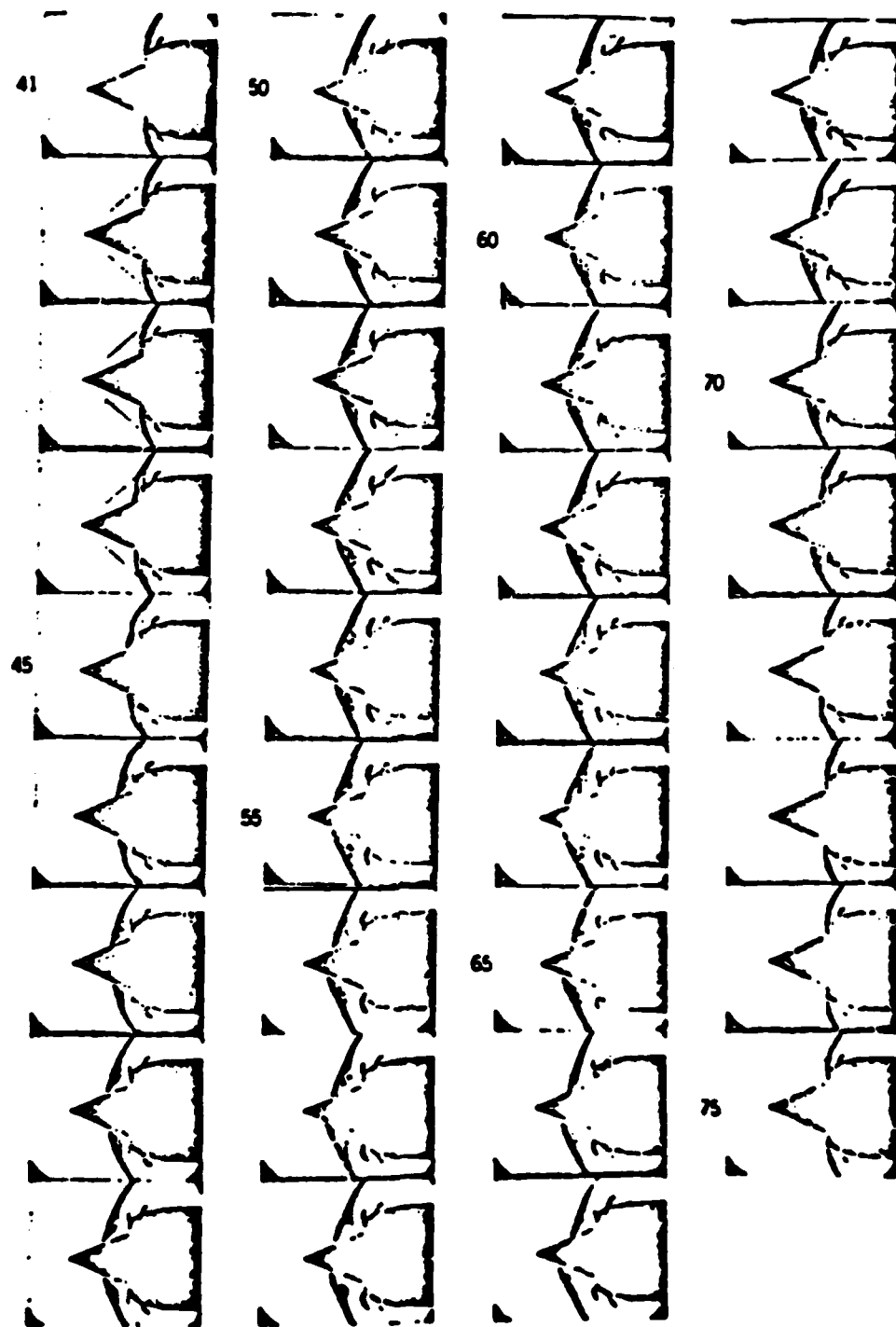
Fig. 11   Schlieren Photography of Traveling Shock Wave
          Low Buzz (TR=.97, Frame Speed = 5600 fps)
          (from Ref 1)
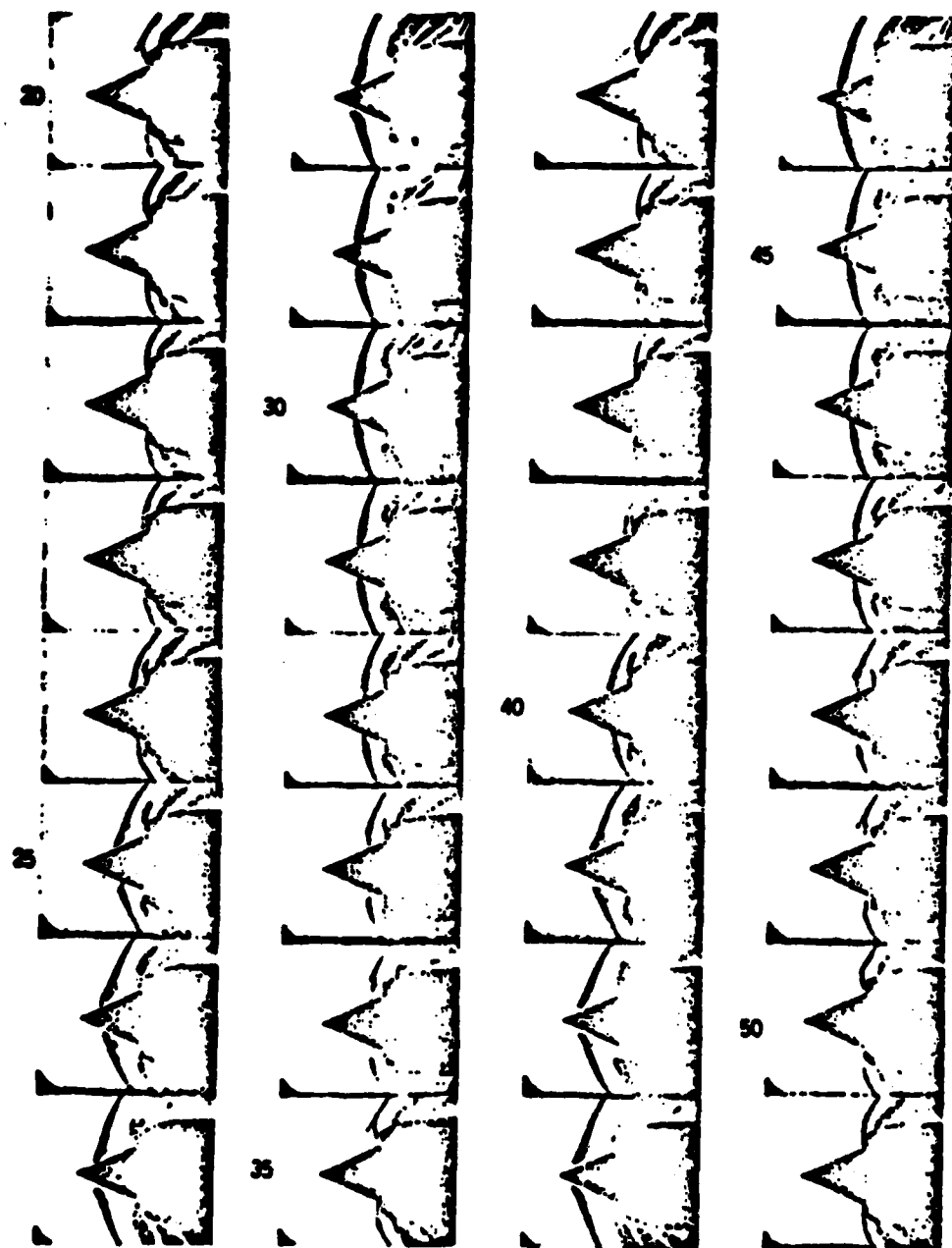
Fig. 12   Schlieren Photography of Traveling Shock Wave
          High Buzz (TR=.67, frame speed = 5800 fps)
          (from Ref 1)

the 6th and 9th modes also observed from spectral analysis. This held true until the throttle valve was completely closed, where tᵇ fundamental frequency was also observed at the two downstream probes. Acoustic theory, outlined in the next section, predicts only odd frequency modes for a duct with an open and a closed end. The amplitude of the fluctuations at first decreased and then reached a much higher value for the low subcritical throttle ratios. The shock movement was larger in amplitude and appeared to be a continuous motion.

4.2 Theoretical Considerations

Before considering the numerical results, valuable insight into the physical mechanisms which govern the buzz cycle can be gained by a brief synopsis of related theoretical work. Rockwell and Nandasher (Ref 65) and Hankey and Shang (Ref 66) both have outlined the necessary conditions for a self-sustained oscillation to occur:

(a) upstream feedback of reflected disturbances from a downstream impingement surface to an unstable shear layer in proper phase and at a frequency where amplification is possible,

(b) selective amplification of disturbances in the unstable shear layer over a limited frequency range.

Feedback Mechanism

The dominant feedback mechanism for the inlet is the reflection of expansion and compression waves in like sense from the downstream throat. The time required for a wave to travel from the upstream disturbance to the downstream throat and back is

$$T_p = \int_0^L \frac{1}{(1+M)c} \, dx + \int_0^L \frac{1}{(1-M)c} \, dx \qquad (4.2)$$

where

c - local acoustic speed at which the disturbance propagates

relative to the mean flow

M - undisturbed mean flow Mach number .

The buzz cycle begins with the forward expulsion of the bow shock on the centerbody and a consequent expansion wave which propagates down the duct. The reflected expansion wave interacts with the bow shock and the shock retreats inward. This generates a compression wave which similarly travels downstream and is reflected to expel the bow shock and begin the cycle again. If it is further assumed that the flow is uniform along the length of the duct, L, then the fundamental period, upon integration, is

$$P = 2T_p = \frac{4L}{(1-M^2)c} \tag{4.3}$$

and the fundamental and higher odd frequency modes as predicted for a duct with an open and a closed end are

$$f_n = \frac{1}{P} (2n-1) = \frac{c}{4L} (1-M^2)(2n-1) \quad n = 1,2,3,... \tag{4.4}$$

This very simple model serves to explain several of the features observed in buzz. The step-like behavior of the shock and the pressure probes at the extreme ends of the inlet is a result of the time delay involved in the propagation of forward and rearward traveling pressure waves. Equation (4.4) also serves to explain the experimentally observed shift in the fundamental frequency with throttle ratio. As the throttle valve is closed, the average duct Mach number must decrease since the throat remains choked and the upstream flow conditions are determined by the area ratio, (A_d/A_*). For example, at the condition TR=.97, the experimentally observed frequency was $f_1 = 110 H_z$. This requires

62

an average duct Mach number, M_d = .36, which is entirely reasonable.
Higher frequency modes may be interpreted as multiple waves within the
duct.

Shear Layer Instability

The central role played by the separated boundary layer region has
been identified from the earliest experimental investigations. The
separation was found to be produced either by the slip line resulting
from the intersection of the bow and conical shocks (Ferri condition,
Ref 5) or as a result of separation on the centerbody induced by the
bow shock (Dailey condition, Ref 10). For the present off-design condi-
tion the Ferri-condition is not applicable since the slip line does not
enter the cowl. Dailey further postulated that the separated region
would instantaneously block the inlet flow as it became very large.

Separated flows possess a point of inflection in the velocity pro-
file, $u_{y_n y_n}$ = 0. Such flows have been known to be unstable since
Rayleigh (Ref 67) first proved "the existence of a point of inflection
as a necessary condition for the occurrence of instability," (Rayleigh's
first theorem). Spatial stability theory has been used by a number
of authors to predict the frequency at which the shear layer will
amplify small disturbances. Michalke (Ref 68) and later Roscoe and
Hankey (Ref 69) considered the hyperbolic tangent velocity profile. In
a subsequent study, Verma, Hankey, and Scherr (Ref 70) studied profiles
corresponding to the lower branch of the Falkner-Skan equations. The
approach was to linearize the governing equations about some known
parallel flow solution for small harmonic disturbances which, in the
inviscid limit, resulted in the Rayleigh equation. The eigenvalue problem

63

was then solved to predict the frequency range where disturbance amplification was possible. The frequency range at which amplification was a maximum, or "natural frequency", then corresponded to the most probable oscillation frequency. For a self-sustained oscillation to develop, the feedback must occur in proper phase and at a frequency where amplification is possible. The actual frequency of oscillation is then fixed at the nearest resonant mode, equation (4.4), where amplification is positive.

Although stability theory is a powerful tool for understanding shear layer instability, it is of limited value as a predictive tool. Instability growth is bounded by viscous dissipative effects and a limit cycle is reached which is not predicted by linear theory. For this reason, the theory can not predict the amplitude of the oscillations. A further problem is that the velocity profile of the separated shear layer at the time of the disturbance must be known before a stability analysis is possible. Normally this is not known unless the solution to the problem itself is known. Also, complex flowfields, such as the subcritical inlet, may exhibit a number of unsteady separated regions for which a time-independent mean flow profile can not be specified. Numerical solutions to the full governing equations are required to adequately describe the fluid dynamic behavior.

4.3 Numerical Results

Overview of Computational Results

Numerical calculations were performed over the range of conditions tested experimentally. One super-critical (near critical) case, TR = 1.42, was chosen because of its intrinsic interest and also to validate the code before attempting the unsteady cases. Subcritical flow was

64

investigated at both high (TR = .97) and low (TR = 0.0) values of inlet mass flow. Because computer time is proportional to the period of the oscillation and hence to the length of the inlet (Equation 4.3), a shorter configuration was considered before the full length inlet was attempted. The shorter inlet was obtained from the full scale model by removing the segment of length corresponding to the constant center-body radius section from 25 to 47.7 cm. This then corresponded to an inlet with an L/D ratio of 10.23.

Geometry for Numerical Models

The inlet geometry of the full scale configuration was identical with the experimental model with several exceptions which were made to facilitate the numerical calculations without significantly affecting the fluid dynamics. The struts which position the centerbody in the inlet were not and can not be modeled unless the full three dimensional equations are solved. Furthermore, the centerbody was extended to merge with the throttle valve, maintaining a minimum radius of .3 cm. This avoided the necessity of having to provide additional axial re-solution of the wake which resulted when the centerbody was terminated. It also avoided the potential difficulty of numerically resolving the region very near the coordinate system singularity with a highly stretched grid. The extended centerbody preserved 98% of the crossec-tional area in that region and had a negligible effect on the total volume of the diffuser.

The most important model difference concerned the downstream throat. For the conditions tested, this throat remained choked at all times. However, as shown in Appendix E, the choking area, upon which the sonic surface must terminate, is not the exit area, A_e, used in

equation (4.1). It is, rather, the area obtained by revolving about

the symmetry axis the normal to the throttle valve which intersects

the rear edge of the cowl. The two areas are related if the geometry

of the throttle valve and the blockage due to the presence of the struts

in the exit are known. Since this latter information was not given in

the report, a procedure was developed to find the actual choking area,

A_*, given the throttle ratio and hence the exit area, A_e, such that the

resulting pressure ratios agreed with those of Figure 7. The procedure

is outlined in Appendix E. This corrected throttle ratio is then

referred to as the area ratio, AR,

$$AR = A_*/A_c \qquad\qquad (4.5)$$

where

A_* - minimum downstream exit area upon which the sonic surface

       must terminate.

The choking condition is a sufficient constraint for the downstream

flow, both physically and numerically. It suffices to position the

shock within the duct, for given inflow conditions, such that mass con-

tinuity is preserved for the resulting distribution of shock and viscous

total pressure losses. In an unsteady flow, the choking condition will

correctly reflect rearward propagating compression and expansion waves.

If a divergent section is added downstream, the flow may be accelerated

to a supersonic exit condition. The no-change condition (Sec 3.3) may

then be implemented as a numerical boundary condition which has no effect

upon the flow upstream of the throat. This arrangement provides a natural

way to accomodate the large amplitude unsteady fluctuations which exit

through the downstream boundary in the subcritical regime.

Upon incorporating the changes outlined above, the geometries

corresponding to the full scale and short inlets computed numerically are shown in Figures 13 and 22. In the present approach, the throttle valve can not be continously varied, as was done experimentally, but must be changed impulsively.

Near-Critical Steady State Solution
(TR=1.42, AR=1.16, L/D=15.88)

One steady state condition was chosen for computation. Primary attention was focused upon the proper treatment of boundary conditions, mesh spacing, turbulence modeling, the extent of the computational domain and graphical display. In this manner, confidence in the solution procedure was established before attempting the unsteady calculations.

The case chosen for comparison corresponded to a throttle ratio, TR=1.42, which is equivalent to an area ratio, AR=1.162. The computational grid used is shown in Figure 14. There were 190 points in the axial direction and 64 points in the radial direction of which 30 were within the duct. Axial resolution was concentrated in forebody and nozzle regions of the inlet where large flow gradients, including the presence of shocks and separated boundary layers, were expected. Minimum axial step size was 0.1 cm and the maximum was 0.6 cm. Minimum radial step size at the wall boundaries was set by requiring a uniform step size across the duct height at the cowl lip. The resulting Δy_{min} = 0.015 cm was then maintained along the length of the inlet. This minimum step size, although necessary for reasonable computer time with an explicit code, resulted in somewhat marginal viscous resolution. For example the minimum step size was roughly twice the

67
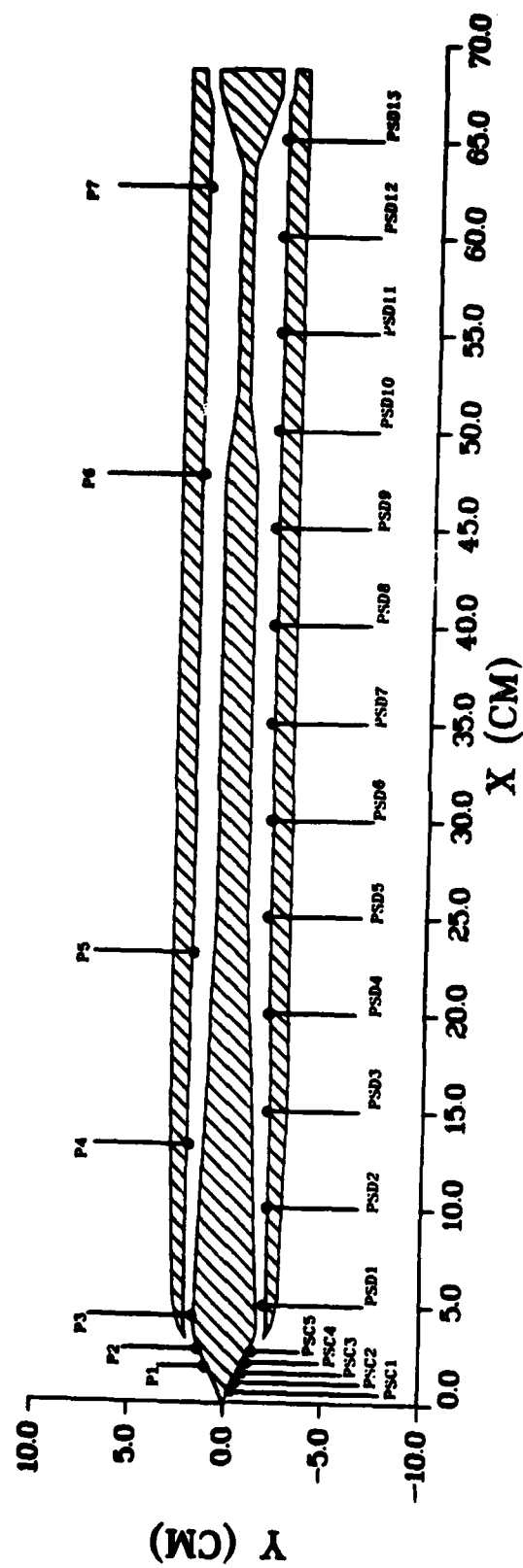
Fig. 13 Inlet Geometry (TR=1.42, AR=1.16, L/D=15.88) with Static Pressure Probe Locations

EXPERIMENTAL PROBE LOCATIONS

Probe	X (cm)	X/L
P1	1.90	.0284
P2	2.80	.0419
P3	4.50	.0673
P4	13.28	.1986
P5	23.28	.3481
P6	47.78	.7145
P7	62.58	.9358

CENTERBODY CONE LOCATIONS

Probe	X (cm)	X/L_{cone}
PSC1	.5468	.1667
PSC2	1.0935	.3333
PSC3	1.6403	.5000
PSC4	2.1870	.6666
PSC5	2.7338	.8333

DIFFUSER COWL LOCATIONS

Probe	X (cm)	X/L
PSD1	5.0	.0747
PSD2	10.0	.1493
PSD3	15.0	.2240
PSD4	20.0	.2987
PSD5	25.0	.3733
PSD6	30.0	.4480
PSD7	35.0	.5227
PSD8	40.0	.5973
PSD9	45.0	.6720
PSD10	50.0	.7467
PSD11	55.0	.8213
PSD12	60.0	.8960
PSD13	65.0	.9707

Table 1   Static Pressure Probe Locations
(L/D = 15.88, see Fig. 13)
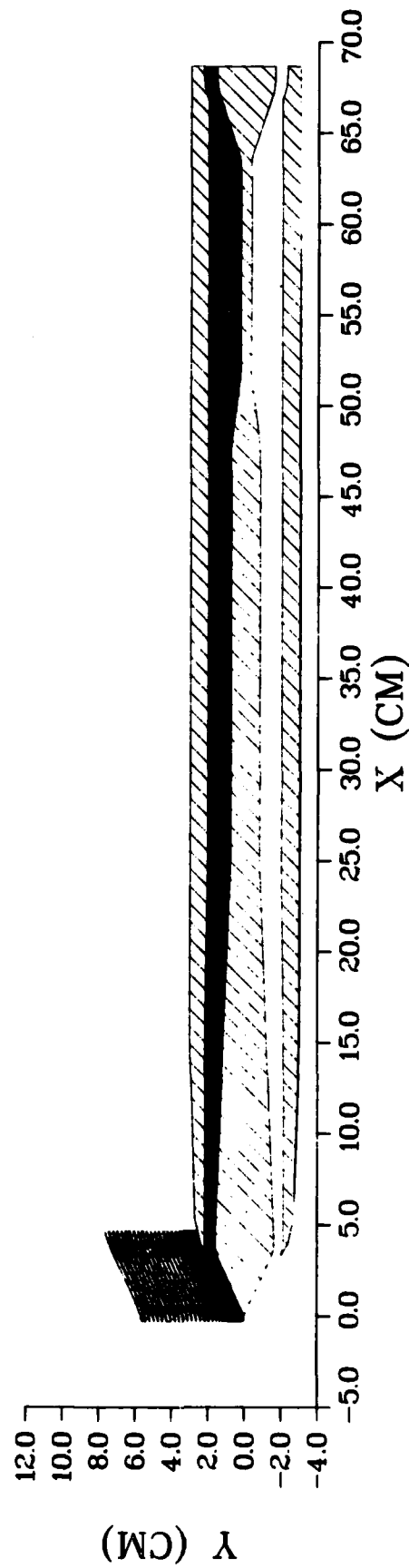
Fig. 14 Coordinate Grid (TR=1.42, AR=1.16, L/D=15.88)

theoretical boundary layer height on the centerbody at the cowl tip. Further downstream within the inlet, the turbulent non-dimensional step size was

$$\Delta y_{min}^{+} = \sqrt{\tau_w \rho_w} \; \frac{\Delta y_{min}}{\mu_w} \simeq 40$$

which is at the edge of the viscous sublayer of the turbulent boundary layer. Although skin friction and heat transfer rates could not be predicted accurately, the overall flow behavior, including the location and extent of separated regions, was presumed to be computed with sufficient resolution.

Figure 15 presents a Mach contour plot of the entire inlet flowfield. Expanded views of the forebody and nozzle regions are shown in Figure 16. The conical forebody may be compared with the Taylor-Maccoll inviscid solution for the cone. At Mach two, the 25° cone generated a conical shock at an angle of 42.5°. The flow behind the shock was then constant on rays eminating from the cone tip. The computed solution was in close agreement with the shock angle, surface pressure ratio and the cone surface Mach number exterior to the boundary layer

$$\Theta_s = 42.5°$$
$$P_c/P_{0_\infty} = 0.297$$
$$M_c = 1.4$$

A second oblique shock was generated by the upper surface of the cowl lip which intersected with the bow shock at some distance above the cowl lip. This intersection resulted yet another shock above the intersection. A slip line, across which magnitudes of velocity are discontinuous, also originated from the intersection since adjacent streamlines passing through the two different shock systems

71

MACH CONTOUR

MACH CONTOURS

Fig. 15 Near-Critical Steady State Solution (TR=1.42, AR=1.16)

72

MACH CONTOUR

MACH CONTOUR
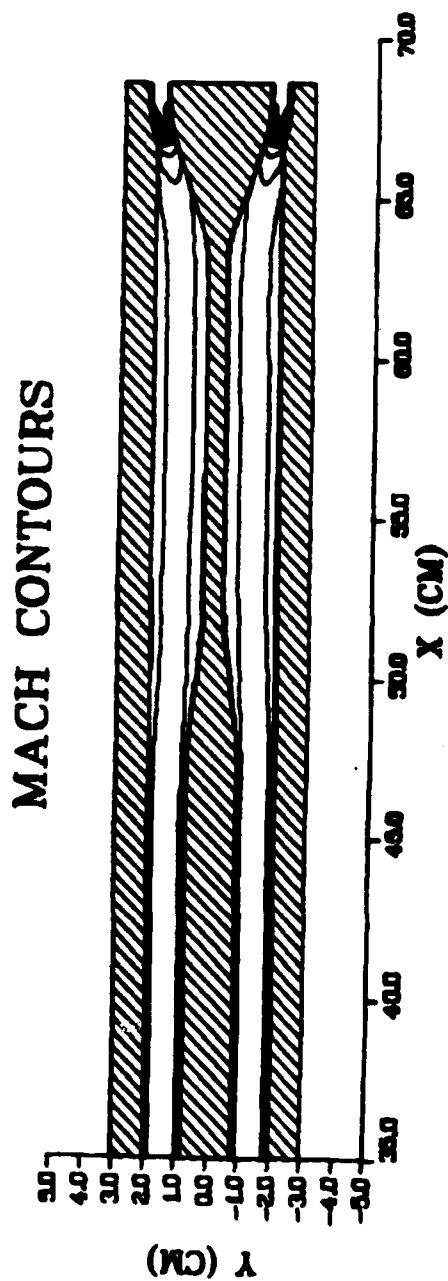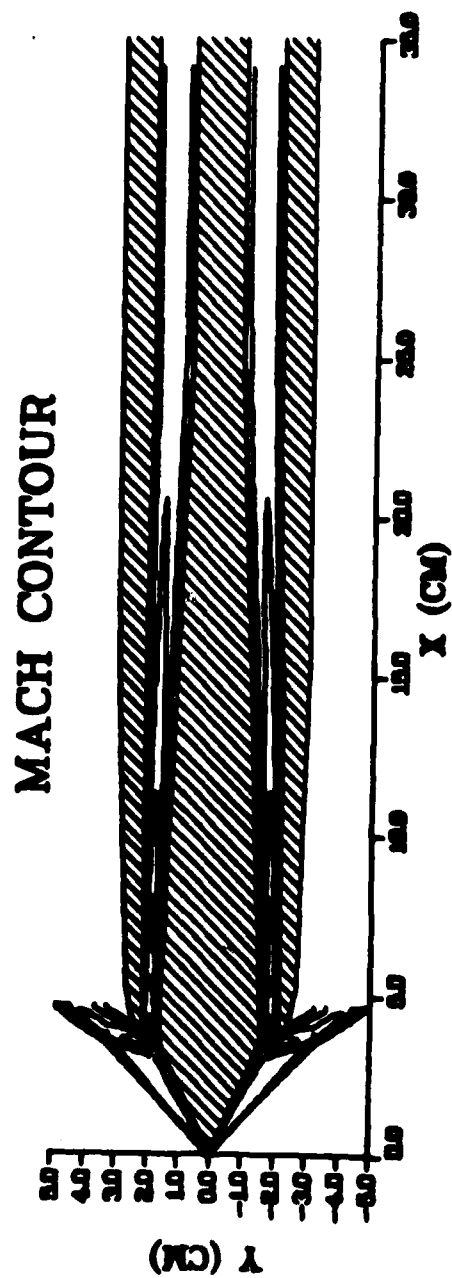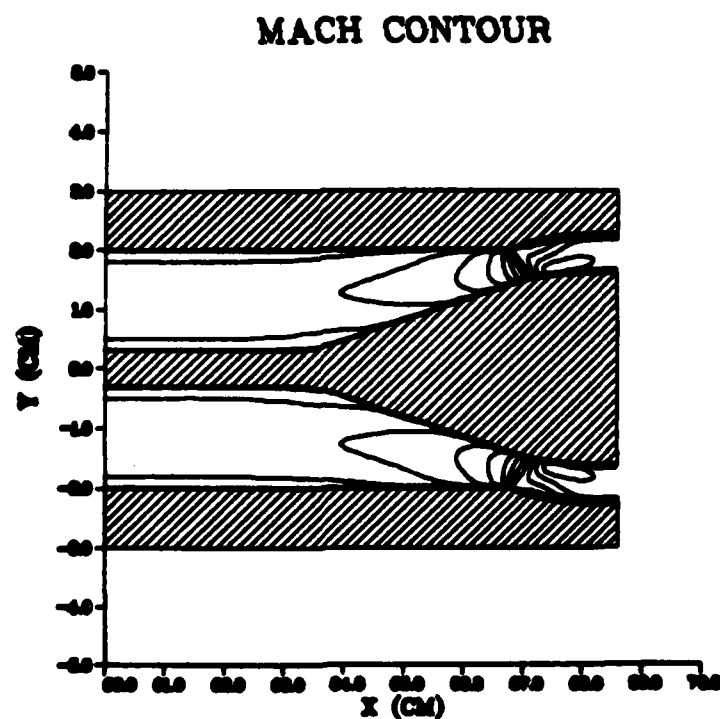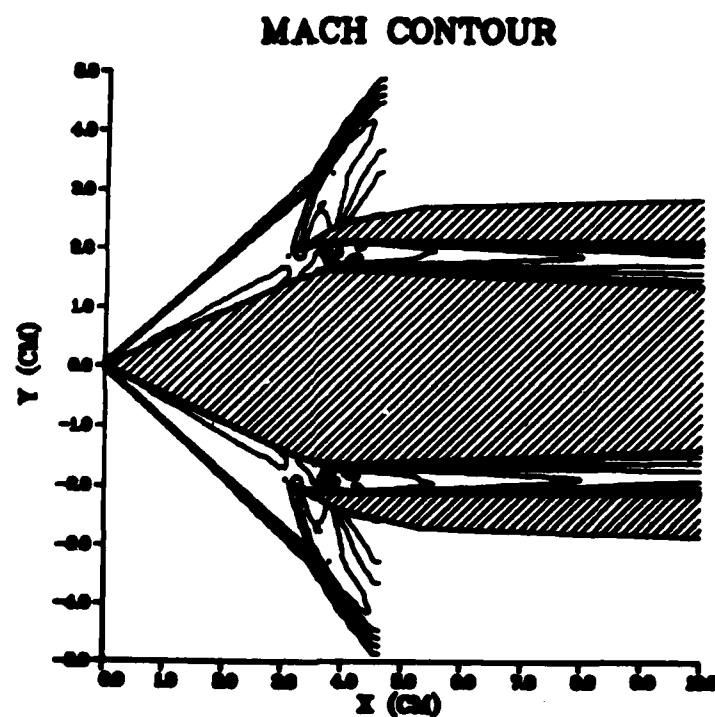
Fig. 16 Expanded Views of Forebody and Downstream Throat
Regions (TR=1.42, AR=1.16)

have the same pressures and flow direction but different values of entropy and total pressure. Further downstream, an expansion fan was generated as the flow was turned about the convex corner on the outer cowl surface. As a result of the interaction with the expansion, the outer shock was then curved and the flow downstream of the interaction rotational. The exterior flow fields of the computational and experimental results may be compared in Figures 8 and 16.

The flow interior to the duct was found to be strongly dependent upon the assumptions made concerning the nature of the flow, as to whether it was laminar or turbulent, where the transition region occurred, and how the turbulent eddy viscosity was modeled. Unfortunately, there was no experimental information to aid in this respect. Neglecting any tunnel-produced freestream turbulence, the flow was assumed to be initially laminar. At some point downstream, a critical Reynolds number was reached in which the laminar flow became unstable and began a transition to a turbulent state. A number of external effects may influence the process (Ref 71: Chap XVII). However, the large adverse pressure gradient associated with the normal shock structure is by far the dominant effect, which may be presumed to trigger the transition rather abruptly downstream from the shock. The shock occurred at a Reynolds number based upon forebody running length, $Re_s = 1.5 \times 10^6$. Since this is roughly half the value of Reynolds number at which transition begins on a cone of the same half angle and equivalent flight conditions (Ref 72), the assumption of laminar flow to this point appears to be valid. At the normal shock, the Cebeci-Smith eddy viscosity model of Section 2.4 was implemented on both the centerbody and cowl as an approximate representation of the Reynolds

stress terms in the mean flow equations. Transition was given by Equation 2.38 with the starting location (s_i) specified at the shock and the final location (s_f) a distance of $3\Delta x$ downstream.

With the assumed turbulence model, the internal flow structure appeared as in Figures 15 and 16. Because the internal cowl lip incidence angle, $\delta_c = 19.24°$, was aligned with the flow angle at the tip, no shock was generated on the lower surface of the cowl. The normal shock structure within the inlet is perhaps the most interesting aspect of the solution. Within the divergent section downstream of the lip, the flow accelerated to an inviscid core Mach number of 1.70 and a one dimensional mass averaged Mach number of 1.60. This was then followed by a normal shock. Although, with the contour levels displayed, this appears in Figure 16 as a single normal shock, the numerical solution displayed considerably more complexity. The dominant shock was followed by a region of roughly three duct heights at the cowl lip, $[y_{outer}-y_{inner}]_{lip}$, in which the flow oscillated within the Mach number range 1.1 to .9. A small separated region developed on the centerbody and extended downstream for a distance of nine duct heights before reattaching. The boundary layer on the cowl was thinner and remained attached. This large deviation from ideal shock behavior can be attributed to shock-boundary layer interaction. Generally, as the boundary layer becomes thicker, the single normal shock is replaced by a series of weak bifurcated normal shocks in which the normal component becomes progressively smaller. This shock structure, termed a "pseduo-shock" by Crocco, is illustrated in Figure 17 and has been discussed by several authors, (Ref 73: Chap 28, Ref 74: Sec B.5, Ref 75). Because of the relatively coarse grid

spacing, the detailed structure of the weak pseudo-shock region was smeared although it was presumed to be correct in an integral sense. The "pseudo shock" was then followed by a region of subsonic diffusion from the sonic condition with significant viscous dissipative losses.
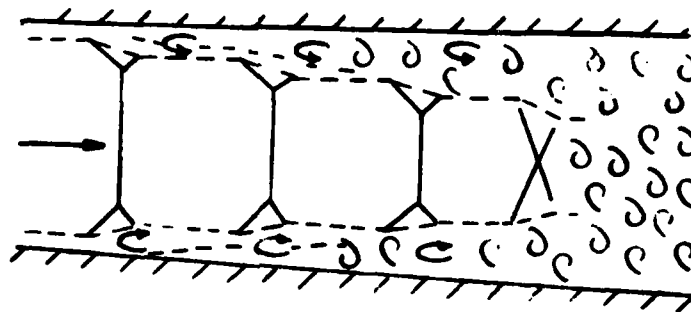
Fig. 17 Typical "Pseudo-Shock" Structure

As an important consequence of the deviation from ideal shock behavior, the pressure rise does not occur discontinuosly but gradually through the shock train and the subsequent subsonic diffusion. Static pressure on the centerbody and cowl surface is plotted in Figure 18. Experimental results from Figure 7 are also shown. The agreement between the two was quite good. One discrepancy was noted in that the shock was positioned slightly upstream of probe p_3 while experimentally it occurred somewhat downstream. This may be attributed to small inaccuracies in the computed total pressure loss due to shock and viscous effects which position the shock, and to some inaccuracy in the conversion of throttle ratio to an equivalent area ratio.

Near the exit, the flow reaccelerated from a low subsonic Mach number (0.3-0.4) to a sonic condition at the throat, Figure 16. Several mass-averaged quanities of interest are shown in Figures 19,
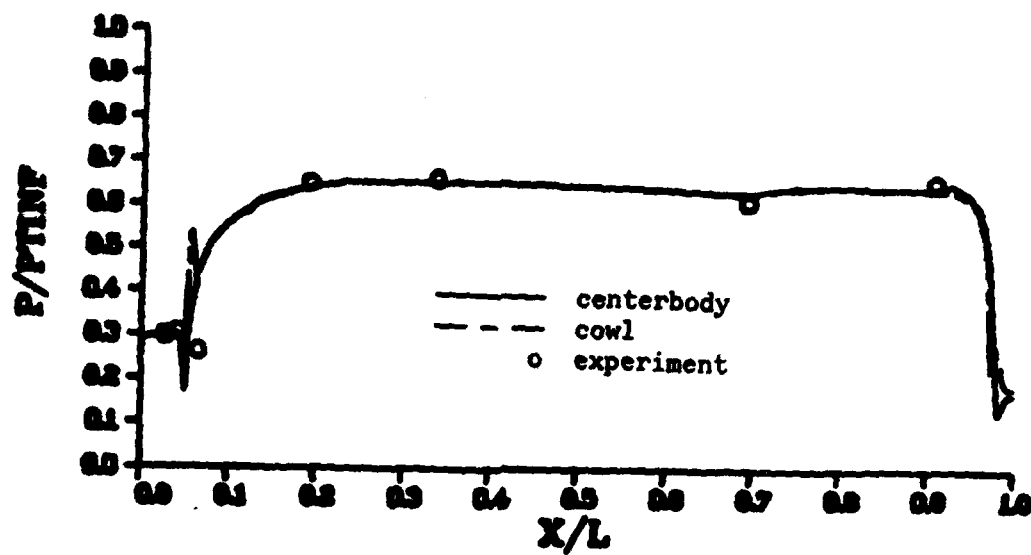
Fig. 18   Static Pressure Distribution (TR=1.42, AR=1.16)
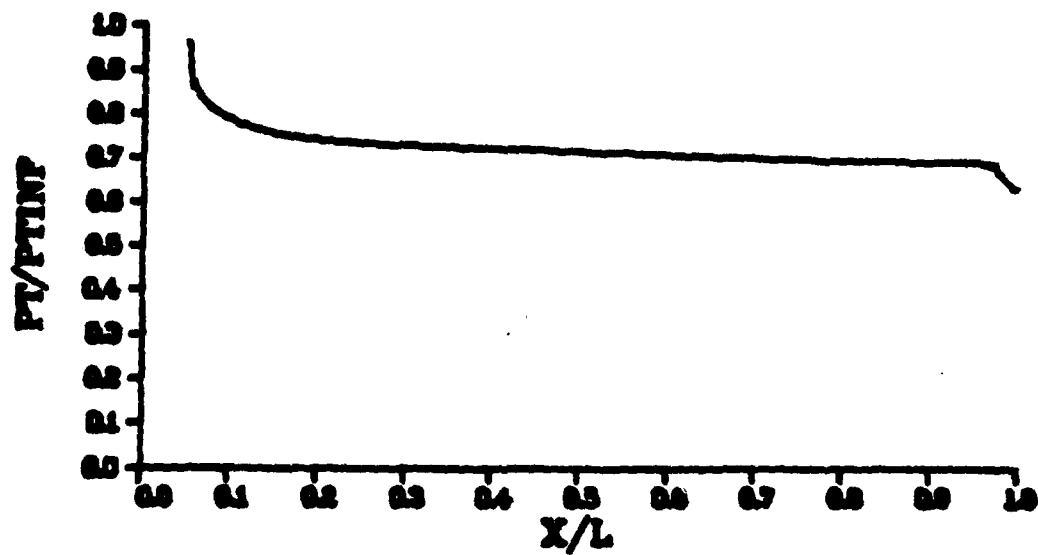
Fig. 19   Mass-Averaged Total Pressure Distribution
(TR=1.42, AR=1.16)
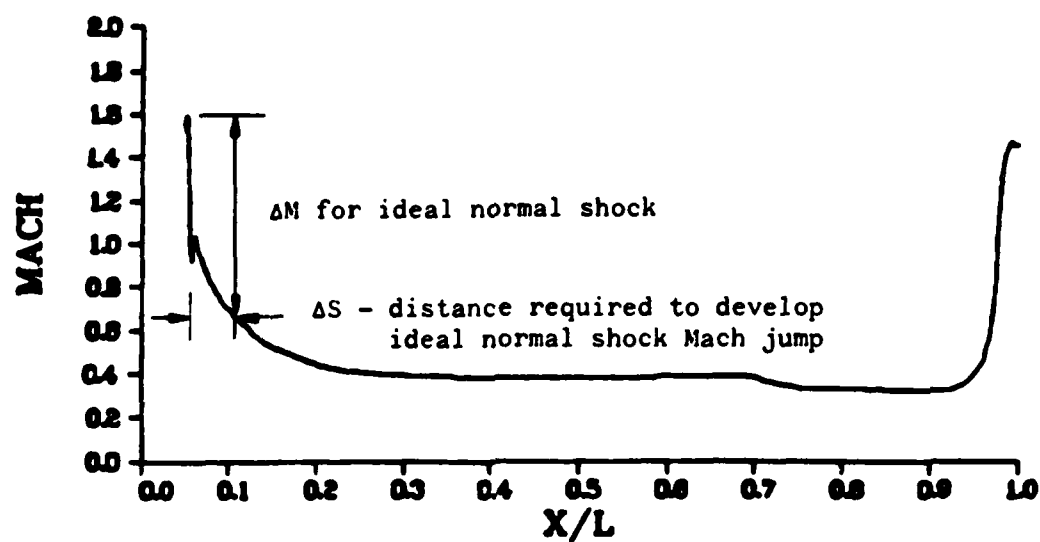
Fig. 20   Mass-Averaged Mach Number Distribution
(TR=1.42, AR=1.16)
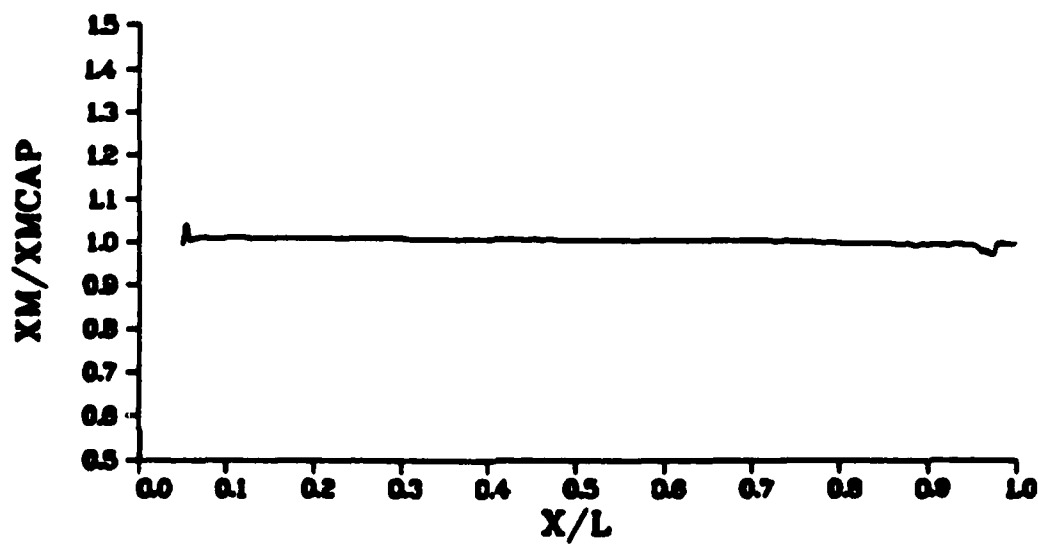
Fig. 21   Ratio of Mass Flux to Supercritically
Captured Mass Flux (TR=1.42, AR=1.16)

20 and 21. Figure 19 presents mass-averaged total pressure along the inlet length. The majority of the total pressure loss occurred in the "pseudo-shock" and subsonic diffusion regions with smaller dissipative and frictional losses through out the remainder of the duct. Figure 20 plots mass-averaged Mach number. It should be noted that the Mach number jump predicted for an ideal normal shock required a distance of 7.6 cowl lip heights over 28 axial grid stations to develop due to viscous-inviscid interaction. Figure 21, in which the ratio of mass flux to supercritically captured mass flux is plotted, demonstrates the steady state nature of the flow at this throttle ratio. The two "kinks" were due to truncation error in the vicinity of the shock and the nozzle throat. However, in keeping with the use of conservative variables and shock capturing methods, continuity was maintained globally.

Subcritical Regime (TR = .97, AR = .83, L/D = 10.23)

In the higher throttle ratio subcritical regime, nearly all the experimental data was for the condition TR = .97. This case was then chosen for numerical comparison. As explained earlier, a shorter inlet, Figure 22, was computed before considering the full scale model. This approach provided a modest saving in grid points and a substantial reduction in the fundamental period of the oscillation, Equation (4.3) and, consequently, computer time. In experimental studies in which the effect of L/D was studied (Refs 9, 10), the onset of the instability was unchanged and the shock wave movement and pressure trace history were similar but occurred at a corresponding higher frequency as L/D was decreased.
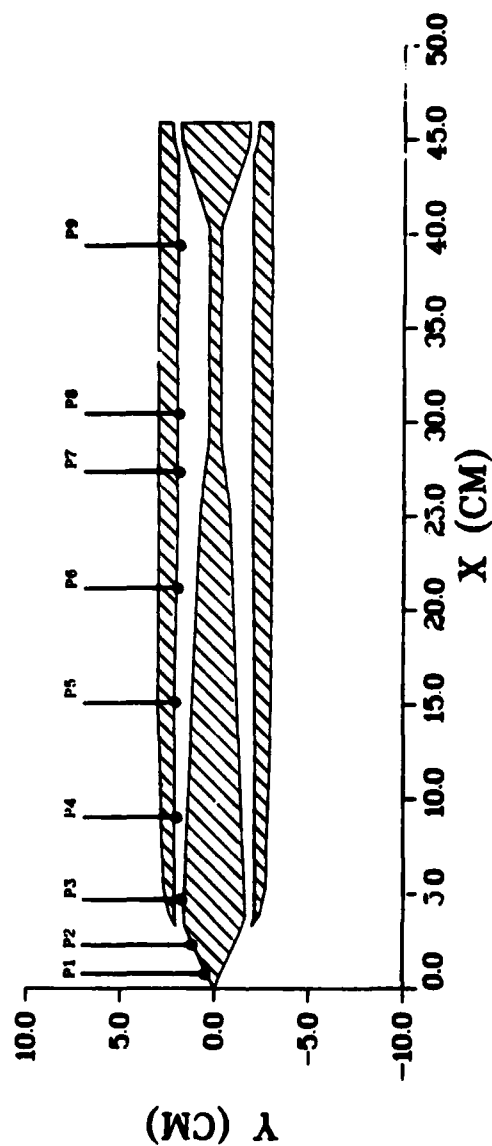
Fig. 22   Inlet Geometry (TR=.97, AR=.83, L/D=10.23)
with Static Pressure Probe Locations

While the numerical simulation was not successful in capturing the naturally occurring self-sustained oscillations reported experimentally, it did provide insight into two important aspects of the phenomenon. First, the calculation was found to be extremely sensitive to turbulence modeling for which no experimental guidance was available. Although the adequacy of a simple algebraic eddy viscosity model is also questionable, the stability of the flow was found to be dependent upon the location and extent of the transitional region. Second, numerical evidence was found to support the contention that the separated boundary layer instability and the resulting flow blockage is the mechanism by which the buzz cycle is triggered.

A grid of dimensions 154 x 64 was used in this case. It was similar to Figure 14 but the external domain was larger to contain the anticipated shock movement. As in the steady state case, the flow was assumed to be turbulent downstream from the normal or bow shock on both the centerbody and cowl. A starting solution was obtained from the previous steady state solution with the downstream throat area impulsively decreased. This generated a compression wave which traveled forward to force the normal shock out onto the centerbody. The solution was continued and converged to a subcritical steady state in which the duct pressure corresponded to the experimentally determined maximum value before buzz onset. Mass flux through the inlet was reduced to 85% of that captured in the supercritical regime. Unfortunately, the experiment indicated that the flow was unstable and buzz present at this condition. The computed turbulent boundary layer profile exhibited only a small separated region on the centerbody. This is normally what is expected, since the turbulent boundary layer is
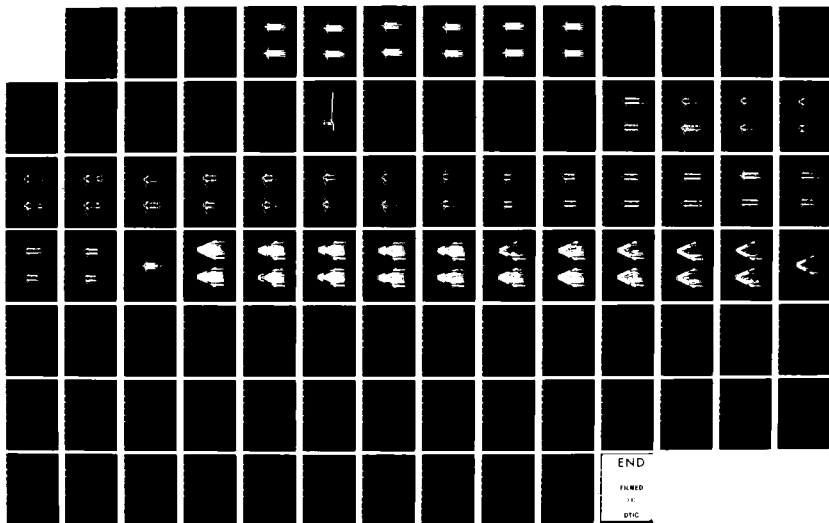
MICROCOPY RESOLUTION TEST CHART
NATIONAL BUREAU OF STANDARDS-1963-A

less prone to separate than its laminar counterpart in the presence of adverse pressure gradients.

A key hypothesis presumed a large region of separated flow as a necessary condition for buzz, (Sec 4.2). Consequently, the transition region was moved downstream beginning at 6 cm ($Re_{s_i} = 2.3 \times 10^6$) and ending at 12 cm ($Re_{s_f} = 4.7 \times 10^6$). Although these locations were rather arbitrary, the intent was to allow a large region of separated flow to develop just downstream of the cowl lip where blockage might then occur. The solution was restarted from the previous solution near the time at which the normal shock had been forced from the inlet.

As expected, the flow was no longer steady. Figure 23 presents a sequence of Mach contour plots which trace the flow development in response to the shift in transition location. A very large region of unsteady separated flow developed on the centerbody downstream from the shock and extended to the arbitrarily prescribed location for fully turbulent flow before reattaching. Separation appears in the Mach contour plots of Figure 23 as a series of irregular and closely-spaced lines of constant Mach number. In results to be presented later (Figures 28, 29) this can be verified by direct comparison of Mach contour and velocity plots. Separation also occurred on the cowl and the core flow followed a sinuous path through this region. Figure 24 plots the instantaneous mass flux through the inlet at times corresponding to Figure 23. Taken together it is possible to at least partially confirm a hypothesis made by Dailey (Ref 10). Referring to Figure 24, the large separated region was found to reduce, or block, the mass flow through the inlet to a value less than half that captured when the separated region was not present. In direct response to this blockage, the shock was forced to

its most forward position at frame $t = .494 \times 10^{-2}$ sec before retreating to its most rearward position at frame $t = .805 \times 10^{-2}$ sec. It thus appears that the origin of the instability was within the unsteady separated boundary layer region just inside the duct. The bow shock remained in a stable subcritical position until forced forward by the momentary downstream blockage associated with the unsteady motion of the separated boundary layer.

If the departure from equilibrium were of sufficient magnitude the inlet would then be expected to enter the buzz cycle. However, the globally organized buzz motion did not occur. As can be seen from Figure 23, the instability remained relatively weak and localized near the laminar cowl lip region and, in particular, did not propagate to the aft end of the duct. Although the duct flow is almost certainly turbulent, the turbulence model appeared to artificially damp the instability. Liou and Coakley (Ref 38) also noted a substantial sensitivity in the degree separation and unsteadiness to the turbulence model.

An additional difficulty is evident in Figure 11 in which the experimental shock wave structure and the flow field are seen to be asymmetric. This was noted in Reference 1 and attributed to slight centerbody ecentricity. Nevertheless, an axi-symmetric solution was computed since this was not thought to be a dominant mechanism. It is clear that the asymmetric shock structure would produce a larger region of separated flow on the leeward side of the inlet and in turn affect the downstream blockage. Given the sensitivity of the flow field simulation to the adequacy of the turbulence modeling and the complete lack of flow field information, the exact nature of the instability process is likely to remain unknown until a more detailed experimental study is undertaken. Because buzz was not found at this condition, the full length inlet was not computed.

MACH CONTOUR - TIME=.286E-02
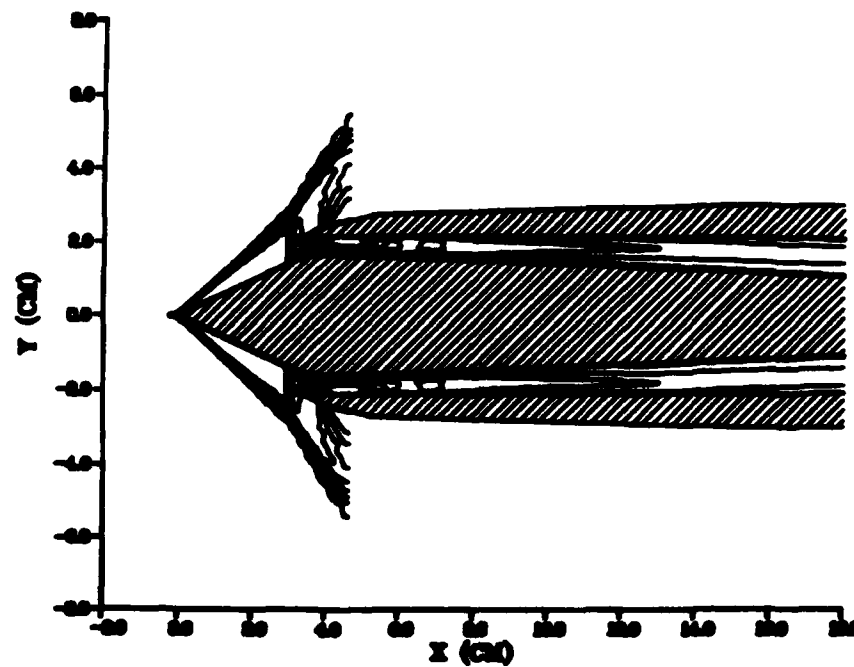
MACH CONTOUR - TIME=.336E-02
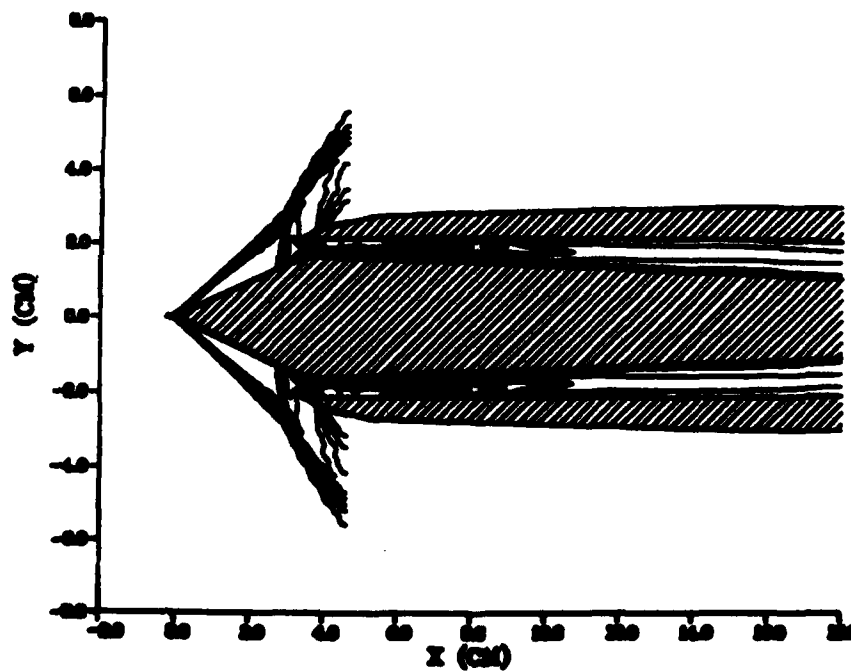
Fig. 23   Shock Movement due to Flow Separation
and Blockage (TR=.97, AR=.83, L/D=10.23)

84

MACH CONTOUR - TIME=.390E-02
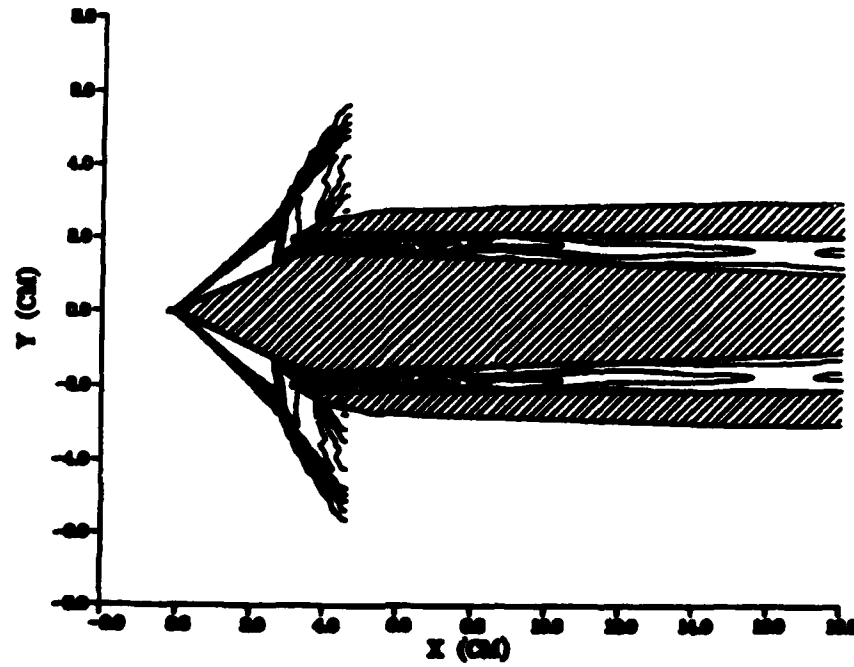
MACH CONTOUR - TIME=.442E-02

Fig. 23 (cont.)

85
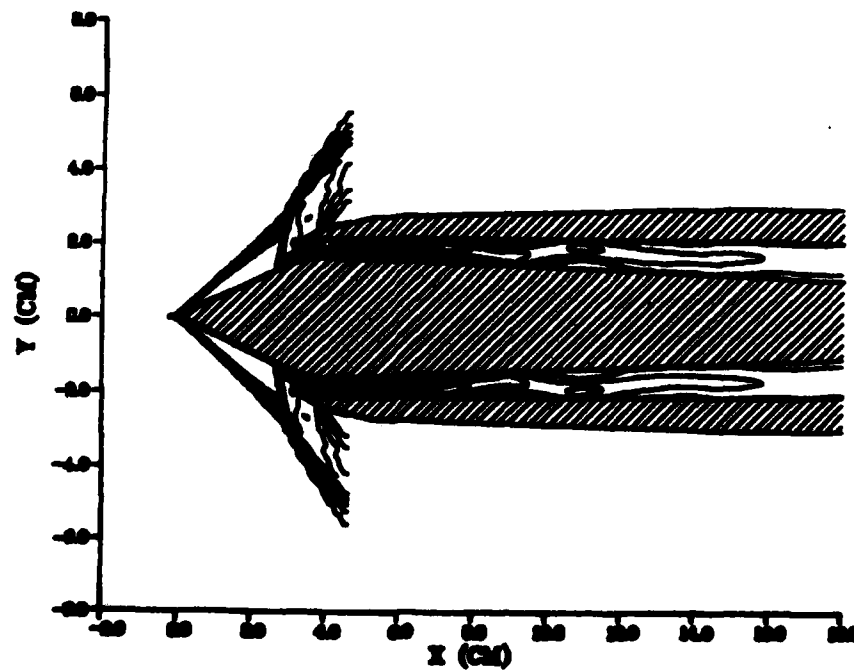
MACH CONTOUR – TIME=.494E-02
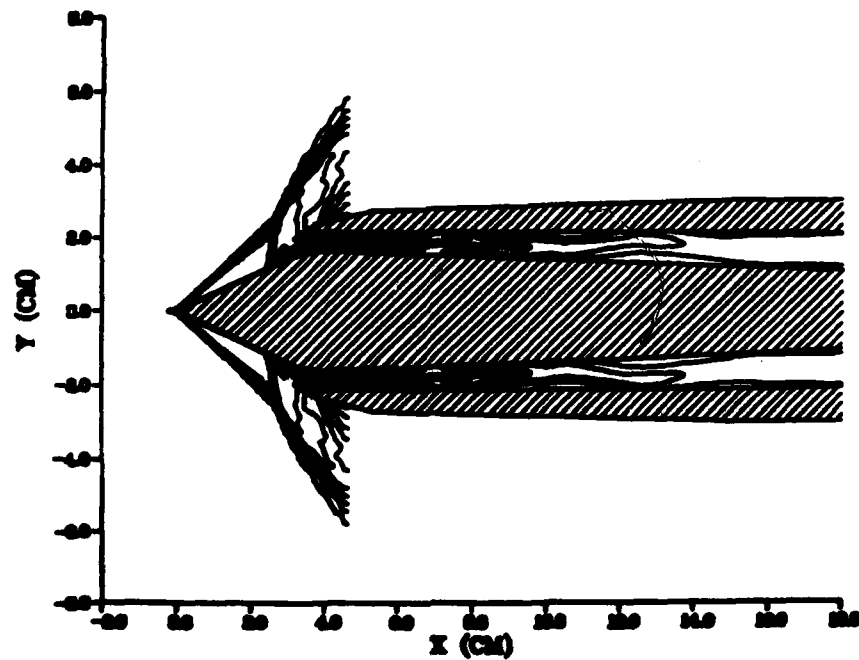
MACH CONTOUR – TIME=.546E-02
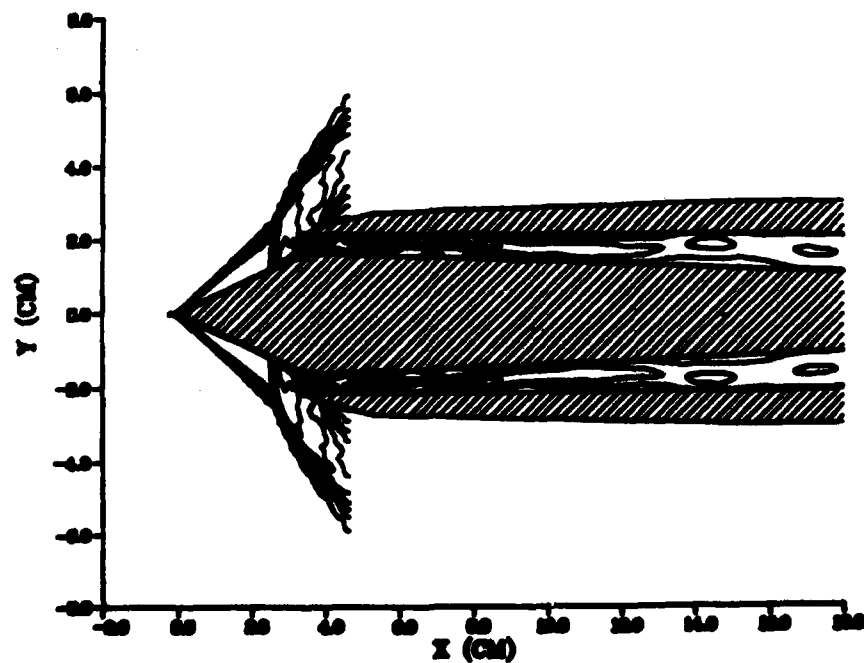
Fig. 23 (cont.)

MACH CONTOUR — TIME=.597E-02
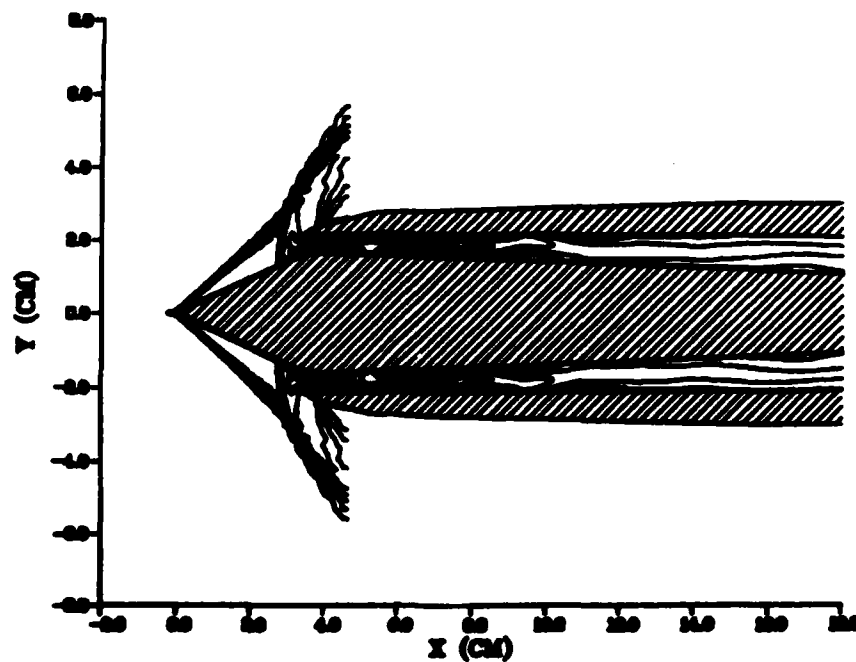
MACH CONTOUR — TIME=.649E-02

Fig. 23 (cont.)

87
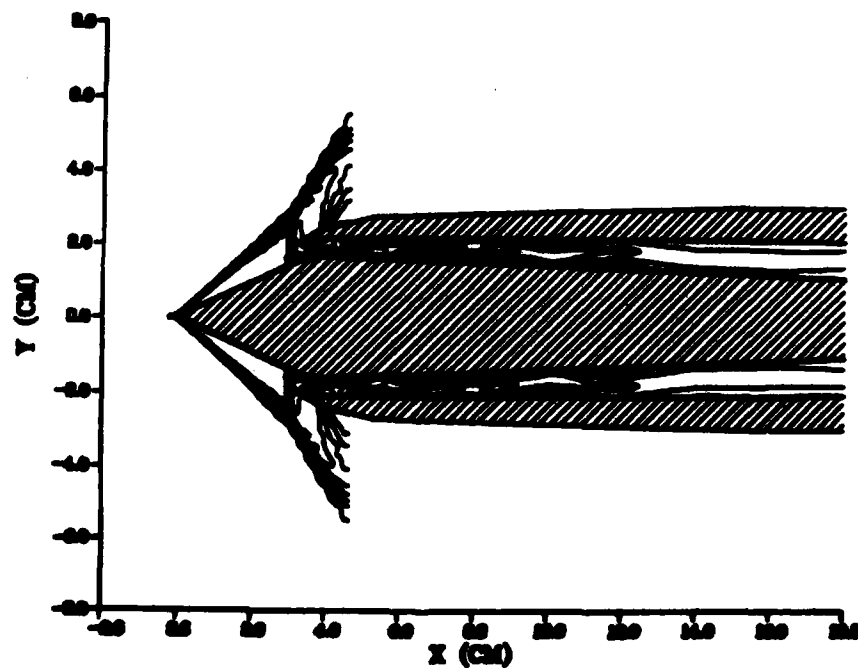
MACH CONTOUR - TIME=.701E-02
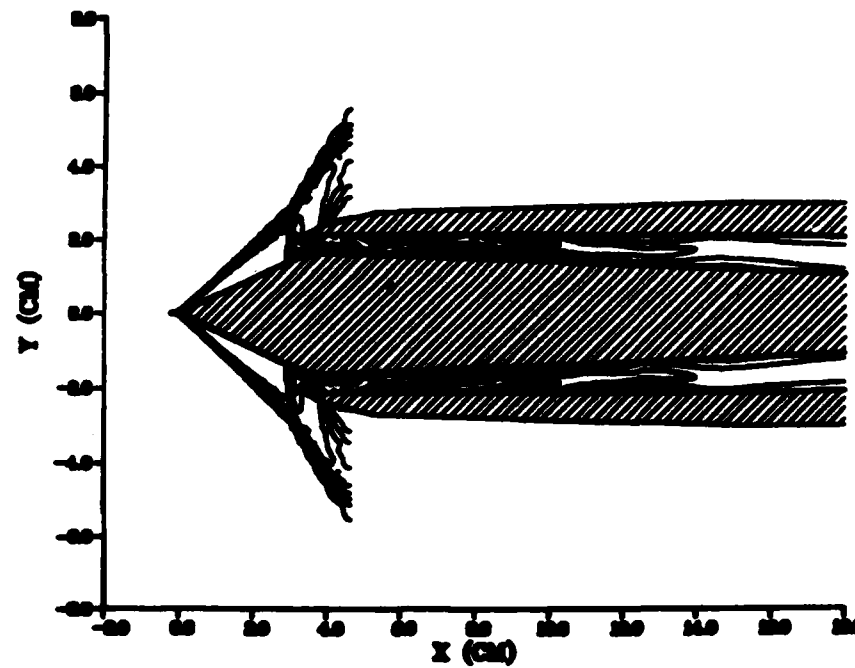
MACH CONTOUR - TIME=.753E-02

Fig. 23   (cont.)

88
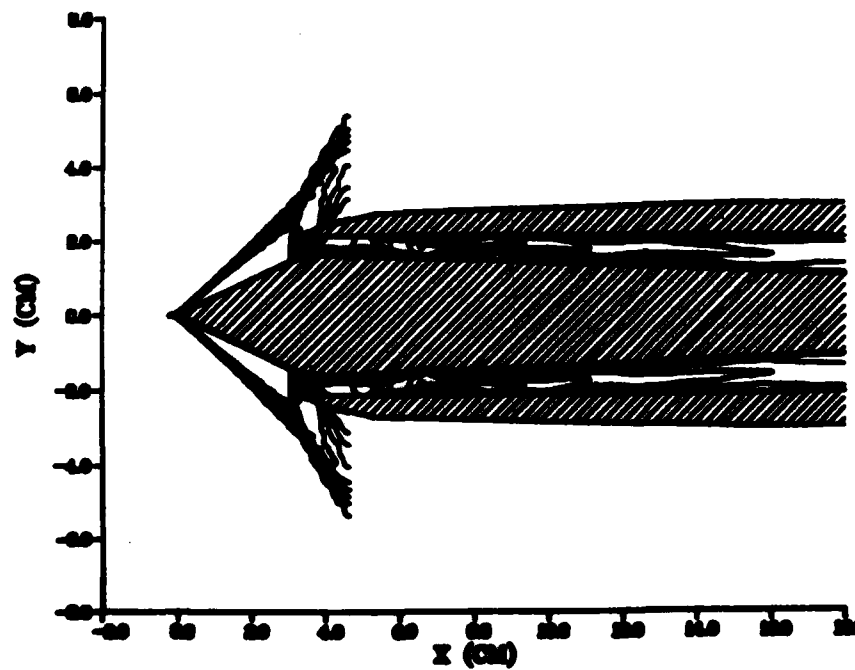
MACH CONTOUR - TIME=.805E-02
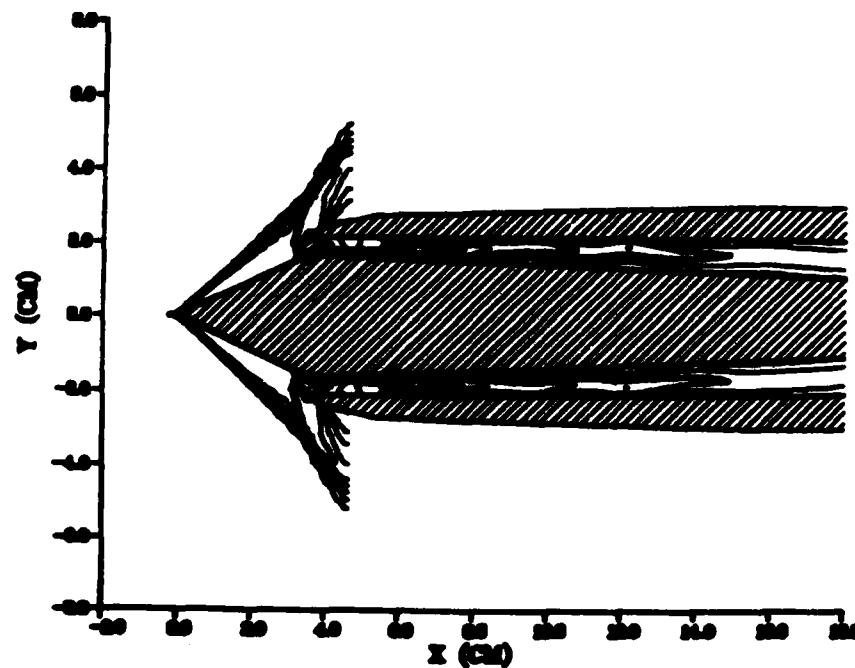
MACH CONTOUR - TIME=.857E-02

Fig. 23 (cont.)

89
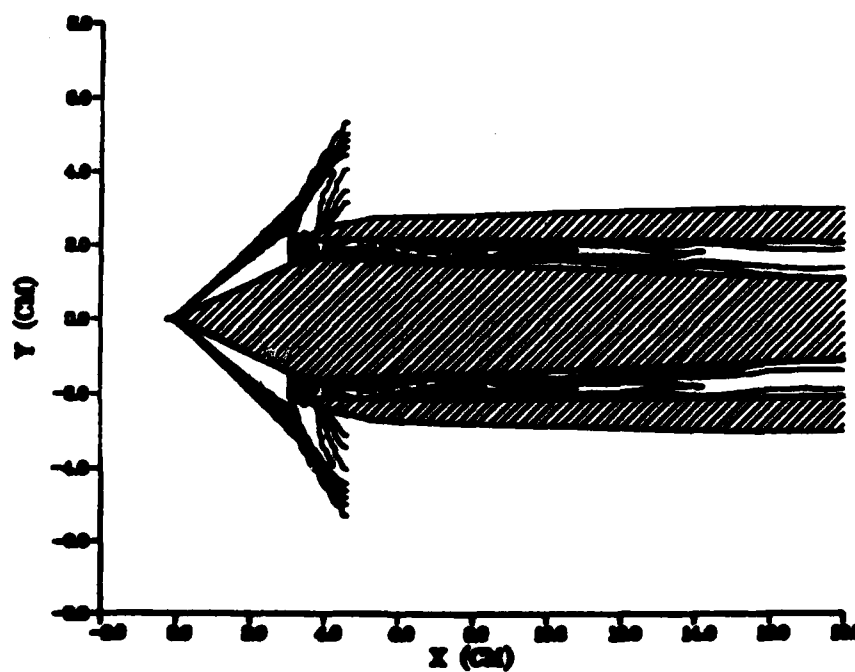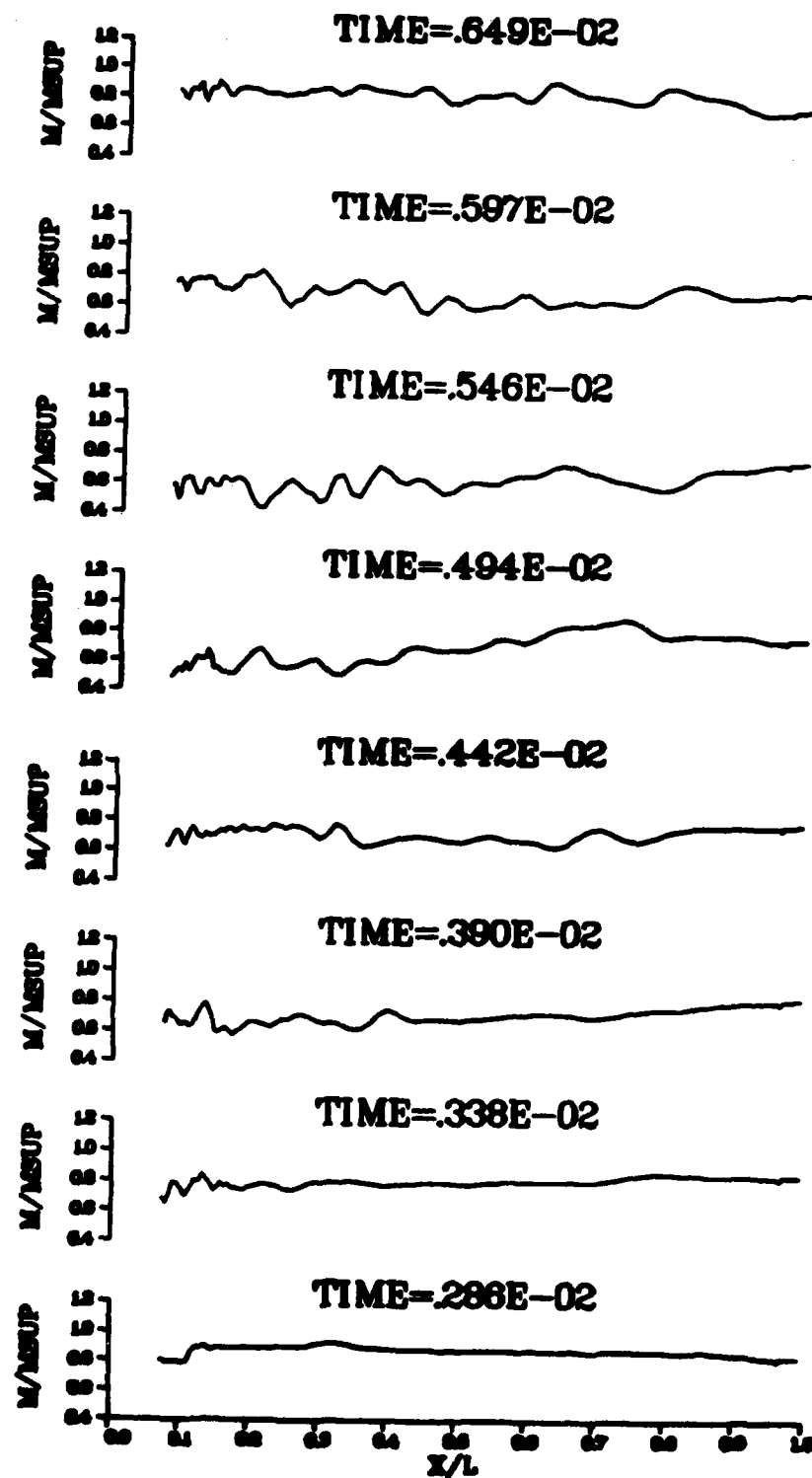
Fig. 24 Ratio of Instantaneous Mass Flux to Supercritically
Captured Mass Flux (TR=.97, AR=.83, L/D=10.23)

Fig. 24 (cont.)

91
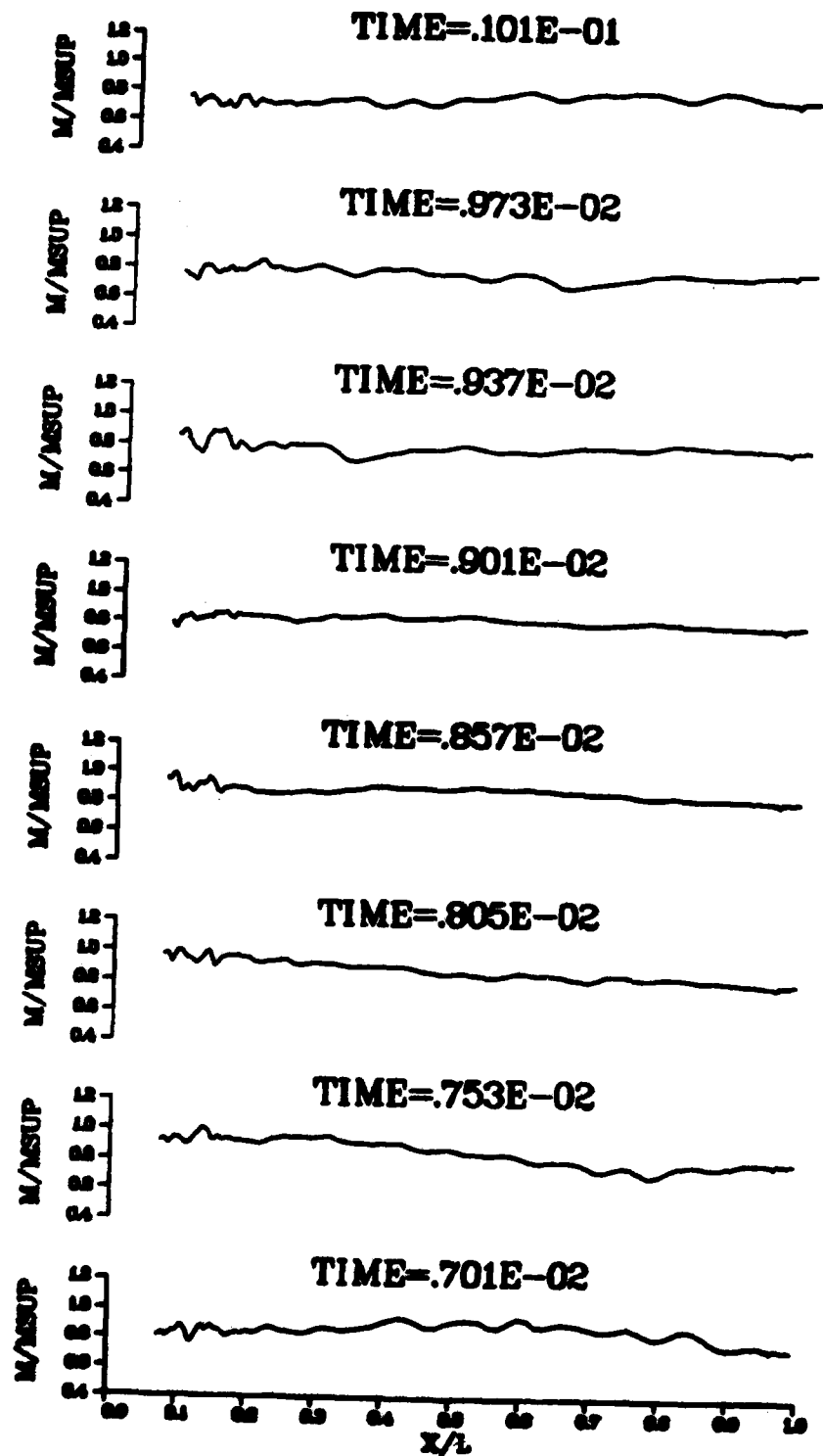
Subcritical Regime (TR = 0.0)

One flow condition at very low throttle ratio was chosen for numerical investigation. Referring to Figure 10, the oscillations observed at this condition were considerably larger than at the higher subcritical throttle ratios.

A decision was made to compute the case in which the throttle valve was completely closed for several reasons. From Figure 10, it can be seen that the amplitude of the oscillations was similar to that obtained when the throttle valve was nearly closed (TR = .35, .55). Experimentally, at low throttle ratios, the frequency was observed to jump to the third and higher modes. This also held true at TR = 0.0 except that the fundamental mode was again evident at the two downstream probes. The primary reason for choosing this case, however, was economy. In order to compute the flow through the very small nozzle throat at low throttle ratios, the minimum step size across the throat would be further reduced. Because the code was explicit, the allowable time step size would then be set by the throat at a much smaller value than was necessary for the remainder of the inlet. The smaller time step would have resulted in unacceptable increases in computer time. As an alternative, the nozzle configuration used in the near-critical solution (TR = 1.42) was also used in this case. A solid wall boundary condition was imposed at the throat station and the computational domain terminated at that point.

Self-sustained oscillations were found at both L/D ratios (15.88, 10.23) for this throttle condition. The discussion will concentrate on the full length inlet which corresponds with the experimental test. A brief discussion of the shorter inlet will then be given.

Full Length Inlet (L/D = 15.88)

The downstream grid for the full length inlet was identical to that of Figure 14 with the divergent section aft of the sonic throat omitted. The upstream region was enlarged to contain the shock structure during the buzz cycle and is shown in Figure 25. Total grid dimensions were then 202 x 64. Initial conditions were fixed assuming stagnation conditions within the inlet:

$u = v = 0$

p = maximum pressure at buzz onset from experimental results

T = adiabatic wall temperature

The external flow field was initialized from previous solutions in which the shock had been forced into a subcritical position on the centerbody.

Because the turbulence model had previously been found to damp the occurrence of the instability it was not applied in the present case. It was expected that the unsteady flow would consist of a large scale organized motion of discrete low frequency peaks and a broad band of higher turbulent frequencies. The numerical code is capable of directly calculating a finite number of low frequency components up to the shortest wave length which can be resolved by the grid. The turbulence model should then only simulate the smaller scale turbulent structure of the unsteady flow. For example, the nth Fourier component of a longitudinal wave propagating with acoustic speed may be expressed as

$$A_n e^{IK_n(x-ct)} = A_n e^{I(k_n x - \omega_n t)} \tag{4.6}$$

where

$I = \sqrt{-1}$

c = acoustic velocity

93

$$k_n = \frac{2\pi}{\lambda_n} \text{ - wave number of nth mode}$$

$$\lambda_n = \frac{L}{n} \text{ - wave length of nth mode}$$

The smallest wave length which is spatially resolved by the mesh is

$\lambda = 2\Delta x$, where Δx is the largest step size on the non-uniform mesh.

Thus, $k_{max} = \pi/\Delta x$ and the corresponding frequency is established from

$$f_n = \frac{\omega_n}{2\pi} = \frac{k_n c}{2\pi} \tag{4.7}$$

For the present case $(\Delta x)_{max} = 0.6$ cm and $f_{max} \simeq 25$ KHz.

On the other hand, Chapman (Ref 39) has quoted a Strouhal number for the

mean frequency of the turbulent eddies for flow over a flat plate as

$$St_\delta = \frac{f\delta}{U} \simeq 0.2 \tag{4.8}$$

If the shear layer thickness, δ, is taken as that of the separated

boundary layer thickness near the cowl lip, and the above formula

assumed valid then $f_{t.e.} \simeq 30$KHZ. Thus the lowest Fourier components

which provide the principle transport of momentum and energy are

resolved while the higher Fourier components which contain the dis-

sipative processes are not resolved and should properly be modeled.

This implies that the period over which the fluctuating quantities are

averaged should be grid and problem dependent (Ref 46). Existing tur-

bulence models, derived from stationary data bases, may overpredict

the appropriate eddy viscosity. If the turbulence model is omitted, the

transport processes are resolved while the dissipative processes are not.

Shang (Ref 36) has recently shown that solutions to the laminar Navier-

Stokes equations can reproduce some "large-scale" turbulent statistical

properties for an unsteady oscillatory flow in the transitional Reynolds

number range. Although the fundamental frequency of the buzz motion is

on the order of 100 HZ, the small scale motion of the separated boundary

layer occurs at a much higher frequency. This motion should not be

94

supressed by the turbulence model in the numerical simulation of the instability.

Under these assumptions, numerical solutions were computed through three complete buzz cycles. The instability was found to develop immediately as a consequence of the non-equilibrium state of the initial conditions. Figure 26 presents pressure-time traces at locations corresponding to the seven experimental pressure probes. Additional locations are shown in Figure 27 for five forebody stations and thirteen equally spaced locations within the duct on the cowl surface. All probe locations are shown in Figure 13. As can be seen from the pressure traces, the instability was first evident near the cowl lip region with rapid shock expulsion on the centerbody well before the disturbance was felt downstream. The oscillation was found to quickly reach a bounded state in which the amplitude was constant. The oscillatory motion may be described as quasi-periodic since the pressure-time traces do display a definite period but are not repeatable due to the irregular superposition of higher frequency components. The dominant step-like behavior of the wave form is obvious at all locations except in the region near and immediately downstream from the cowl lip. The frequency of this dominant mode can be accurately established by evaluating the period at which the shock just crosses any of the forebody locations on successive cycles. The calculated frequency was found to be 128 HZ. This agrees closely with the simple theoretical prediction, Equation (4.4), of $f_1 = 127$ HZ. Additional higher frequency modes were introduced by the unstable separated boundary layers near the cowl lip region where no recognizable pattern was evident. Since only three cycles were computed, there was insufficient data to perform a Fourier analysis of the wave form.

95

A sequence of 41 Mach contour plots, defining the third buzz cycle is shown in Figure 28. The bow shock was forced to the tip of the centerbody as a result of interaction with the reflected compression wave. In the explusion phase, a region of reverse flow was found to extend between the base of the shock and the cowl lip. The strong shear layer dividing the two flow regions is clearly visible in frames $t = .159 \times 10^{-1} \rightarrow t = .171 \times 10^{-1}$ sec. In frame $t = .173 \times 10^{-1}$ sec, the shock has been pushed to the tip, at which point the shear layer ruptured and flow was then expelled radially outward from the inlet. The shock then remained near the centerbody tip and flow expulsion continued until frame $t = .197 \times 10^{-1}$ sec. At this point the inlet started to ingest mass again and the shock began a rearward retreat towards the cowl. The shock then assumed a position just forward of the cowl lip where it remained throughout the remaining half of the buzz cycle. During this part of the cycle, the presence of several separation cells was clearly visible. The first extended from the base of the shock and successive cells alternated between the center- body and the cowl out to about 10 to 12 cm. The core flow followed a sinuous path through this region. The cell length was found to be roughly 3 cm. There is some evidence that the frequency ($\simeq$ 2800 HZ) associated with this length scale through Equation 4.4 may correspond to some of the more random small amplitude oscillations evident in Figures 22 and 23. A 16 mm color graphics movie was also made from this same contour sequence. In the movie, the lower leg of the bow shock was observed to undergo a small amplitude oscillatory movement in addition to the basic buzz cycle movement. This motion was apparently in response to the transient flow blockage caused by the unsteady motion of the separated boundary layers downstream.

96

Figure 29 consists of a sequence of 21 velocity plots again covering the third buzz cycle. Many of the previously described features are also evident here as well. In particular, the reverse flow region which forces the shock forward, the radial outflow of the expelled mass, and the separation cells within the inlet are obvious. As a result of the mass expulsion, a vortex structure situated on the cowl lip can also be seen in frames $t = .167 \times 10^{-1} \to .179 \times 10^{-1}$ sec.

Figure 30 provides a time history of mass flux through the inlet (cowl lip to nozzle throat) for the computed three cycles. The propagation of disturbances through the inlet can be tracked by following successive time frames although this becomes more difficult as additional disturbances are introduced. One suprising result was the magnitude of the mass flux through the inlet. It was found that the maximum mass flux in both the expulsion and ingestion phases was consistently near the same magnitude as the supercritically captured mass flow. The separated boundary layer, depending upon the extent of separation, appeared to control the mass flux ingested by the inlet. Since the downstream throat was closed, once the oscillation reached a bounded limit cycle, the expelled mass flux must necessarily be equal to that ingested. Given the bounded nature of the pressure oscillations, this apparently held true although the first cycle shock expulsion was somewhat weaker and the second somewhat stronger than that shown for the third cycle.

The only experimental information available for this case appears in Figure 10. The dominant frequency was apparently three times the fundamental mode although the fundamental mode was observed at the two downstream probes (p6, p7). The numerical solution appeared to be a hybrid of the two buzz regimes shown in Figure 9. The fundamental mode was dominant and there was considerable similarity in both the waveforms

97

and the phase relationships with the TR = .97 case. Figures 9 and 26 are replotted in Figure 31 for side-by-side comparison. The amplitude of the oscillations from the numerical solutions more closely resemble the experimental result, TR = 0.0. The oscillation amplitude, as obtained from Figure 26, is plotted in Figure 32 and compared with experimental values from Figure 10. Because the computed wave form is different, the point by point correspondence with Figure 10 is not particularly good, although the maximum and minimum bands are in agreement. Figure 33 depicts the time averaged values of the pressure traces given in Figures 26 and 27 with the $2\Delta P_{rms}$ band superposed on the average valve. Numerically, the oscillation amplitude steadily increased along the duct length while the experiment displayed an antinode at probe 4 as well as probe 7.

The sudden frequency shift as throttle ratio is decreased at low mass flows has also been observed in other experimental works. Dailey, (Ref 10), reported that the higher frequency does not scale with L/D but remains relatively constant as length is changed, suggesting a local instability mechanism. Trimpi (Ref 9) found the high frequency motion to intermittently break down and reform. Nagashima, (Ref 1), was unable to capture the higher frequency motion when the centerbody was removed. Although several hypotheses, such as vortex shedding, (Ref 10), or an edge tone phenomenon, (Ref 13), have been advanced to explain the frequency shift, this mechanism is still not understood today. It was speculated that the higher frequency might be triggered numerically by an initial condition consisting of several spatial waves along the inlet length, but this has not been tested. Given the complexity of the physical mechanisms involved, numerically capturing the fundamental mode is thought to be an encouraging first step.
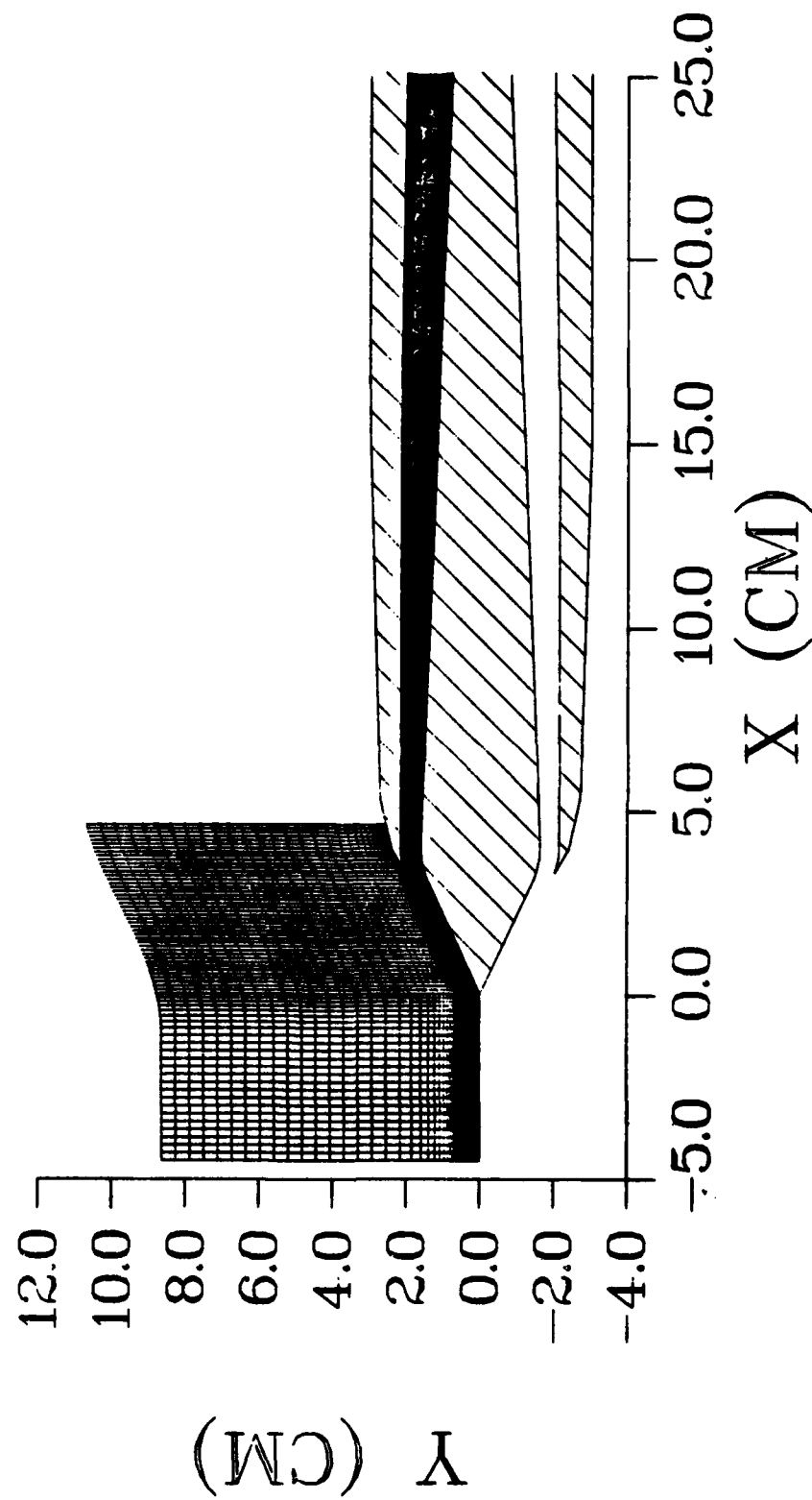
Fig. 25 Computational Grid in Upstream Region (TR=0.0)
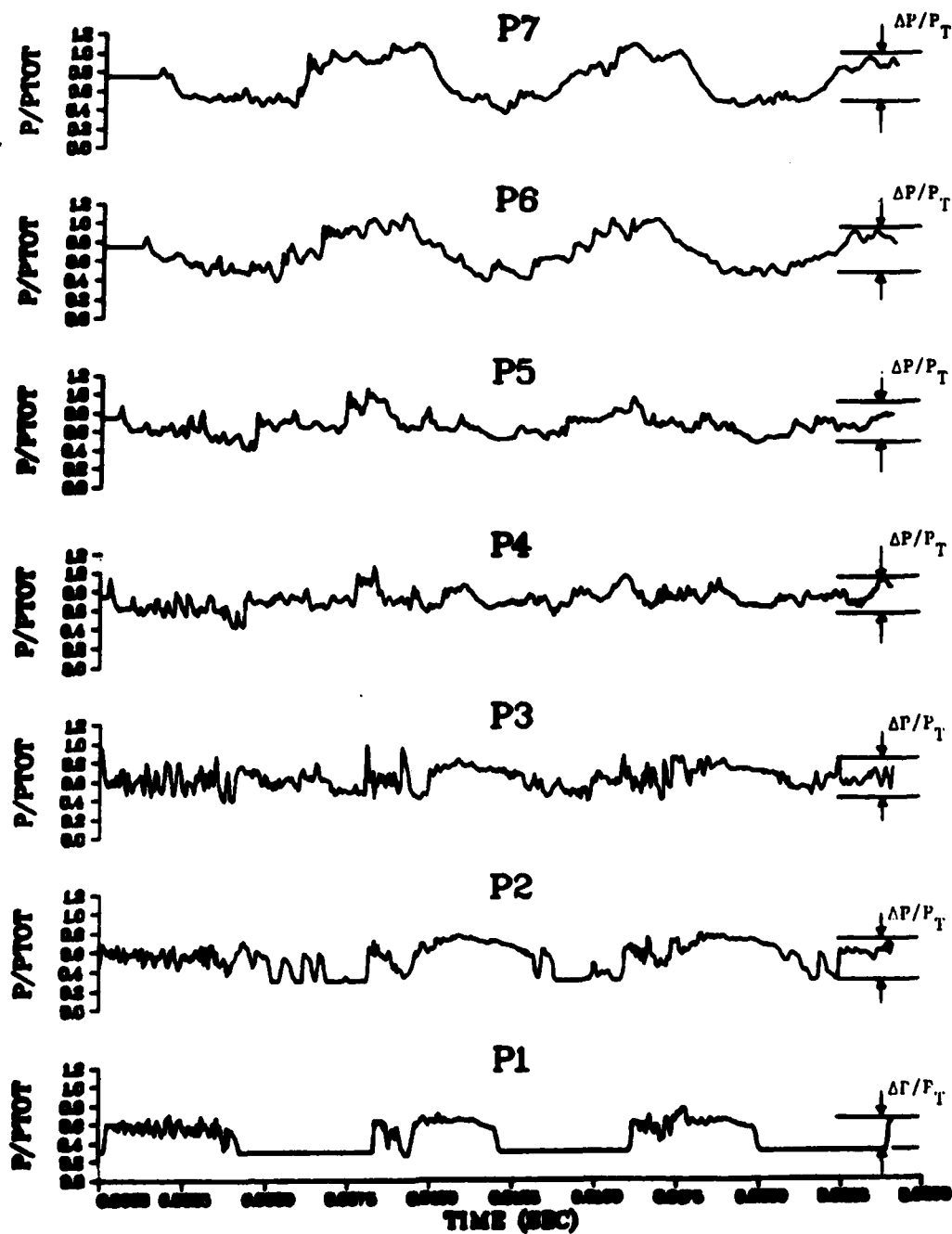
Fig. 26 Computed Pressure Fluctuations for Experimental Probe
Locations (see Fig. 13), (TR=0.0, L/D=15.88)
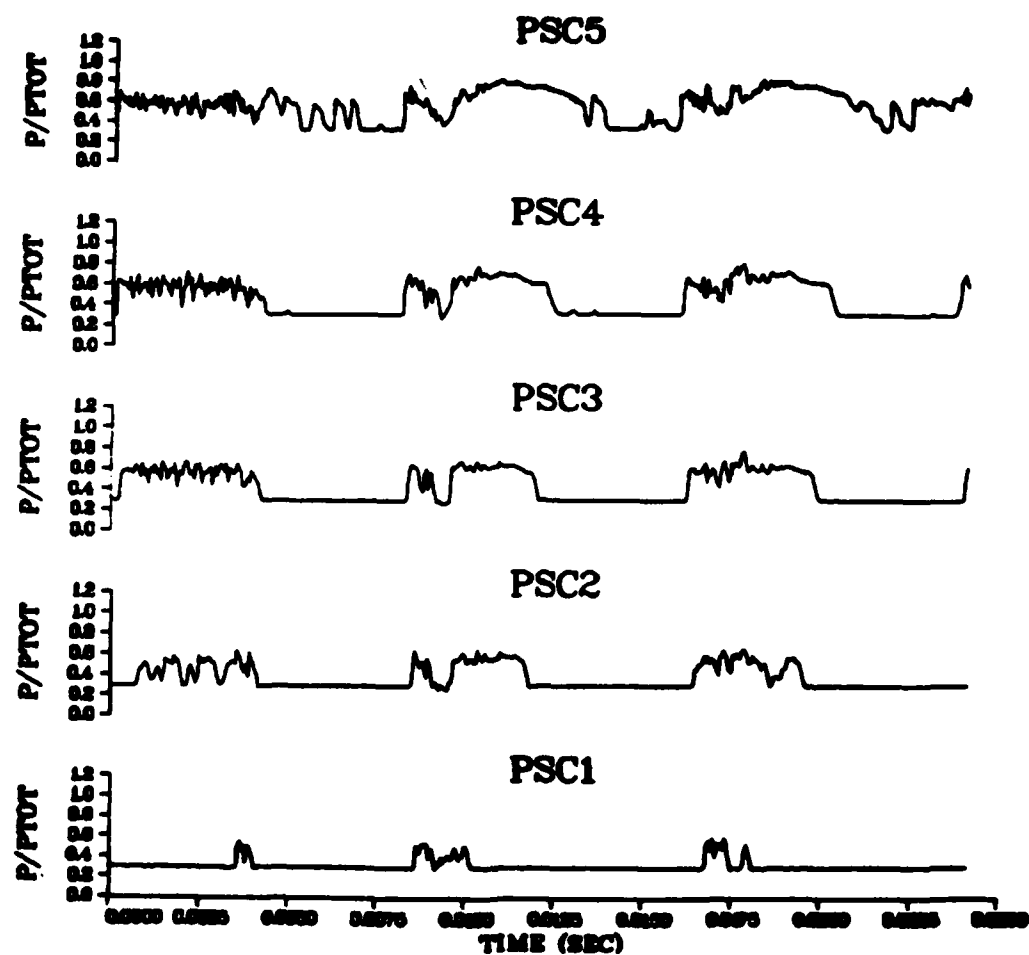
Fig 27 Computed Pressure Fluctuations for 5 Centerbody and 13
Diffuser Locations (see Fig. 13), (TR=0.0, L/D=15.88)

101
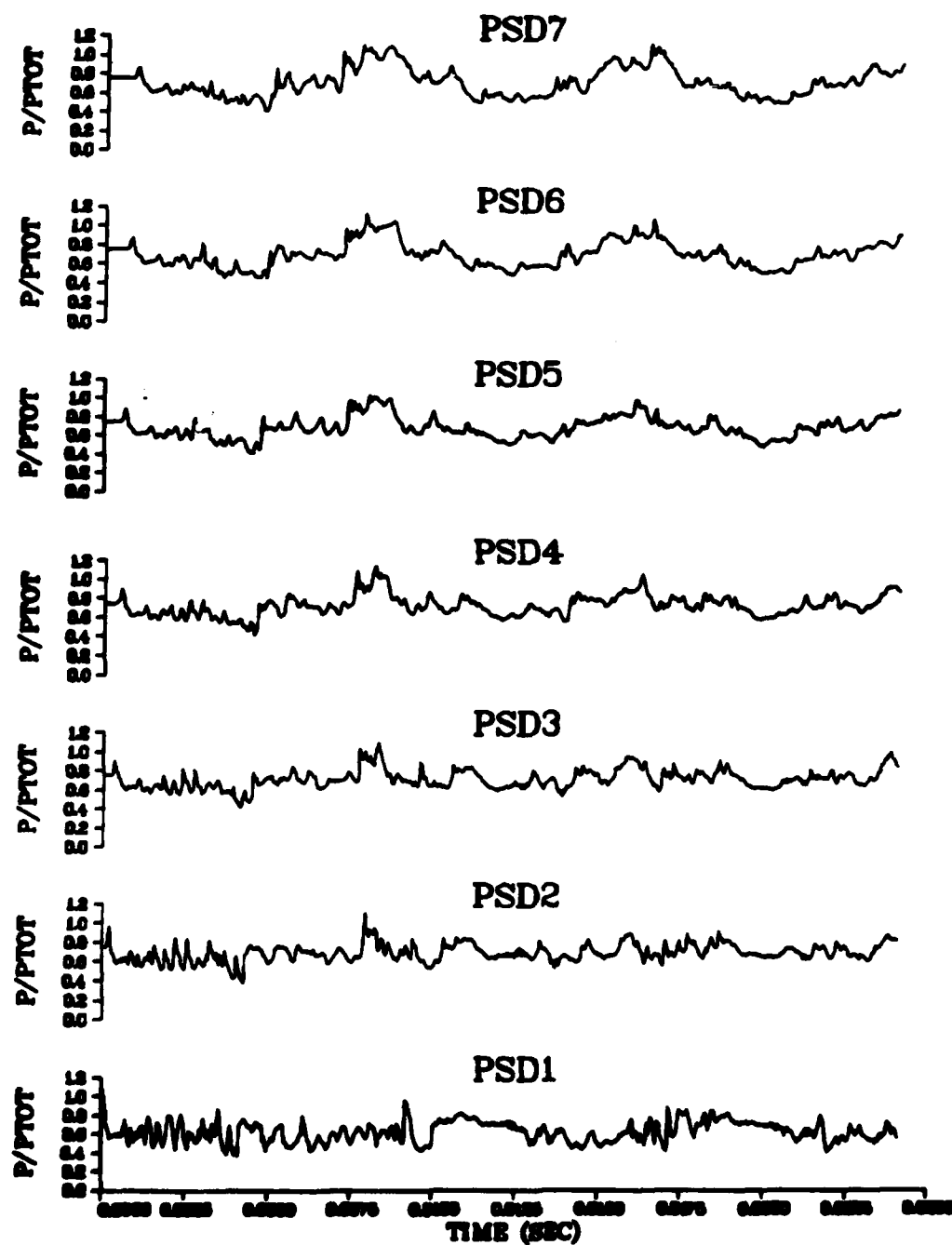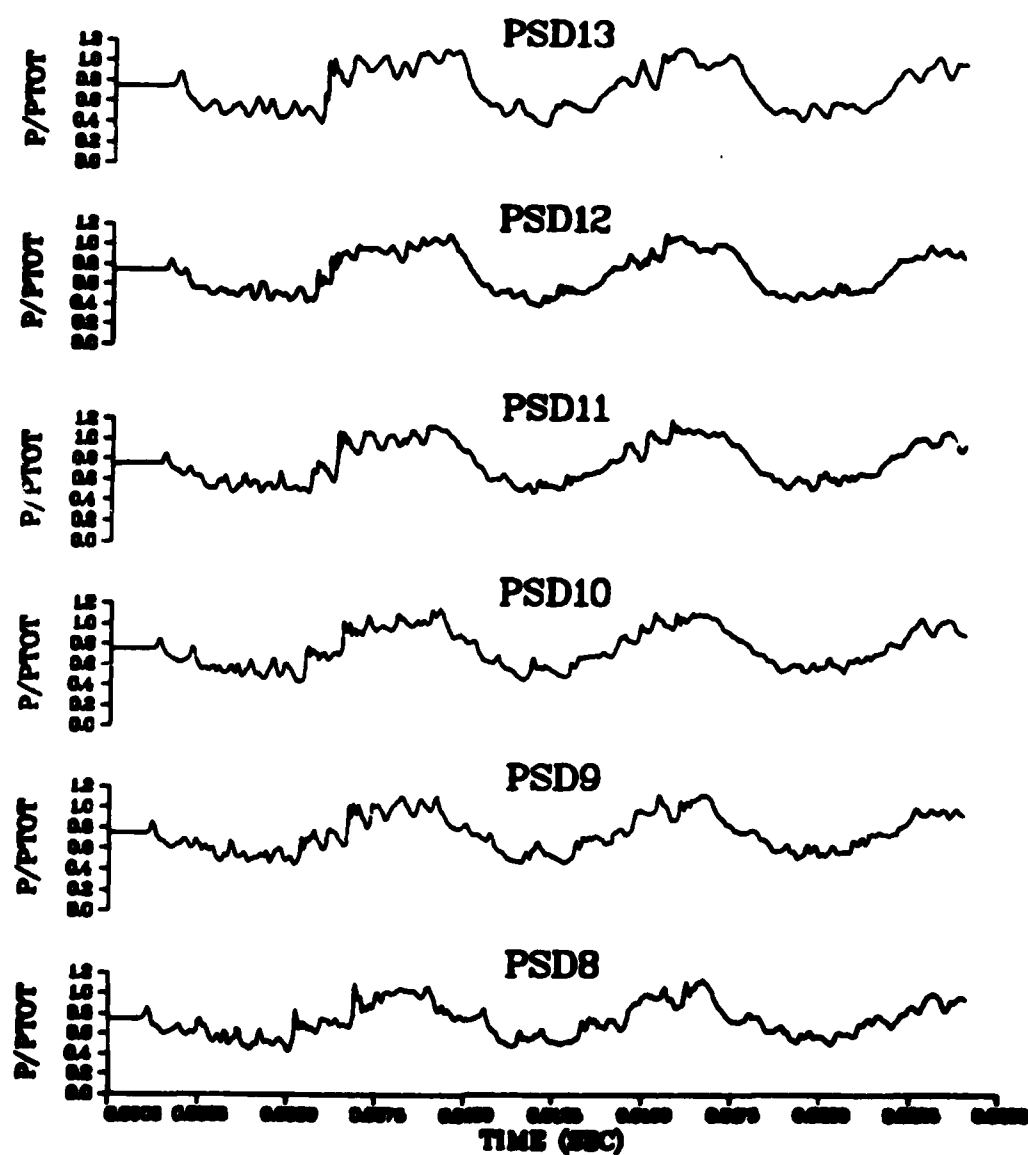
Fig. 27 (cont.)

Fig. 27 (cont.)

MACH CONTOUR - TIME=.159E-01
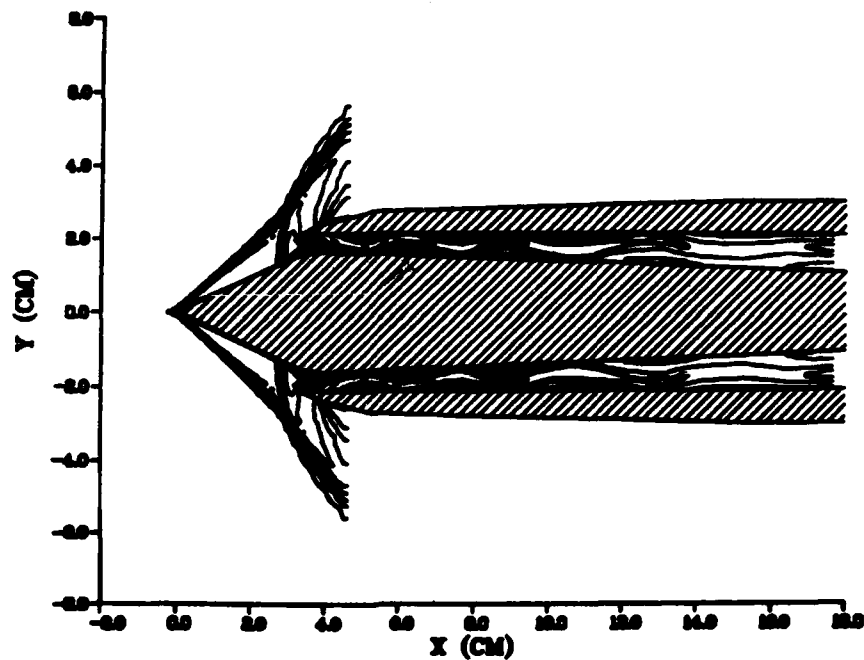
MACH CONTOUR - TIME=.161E-01
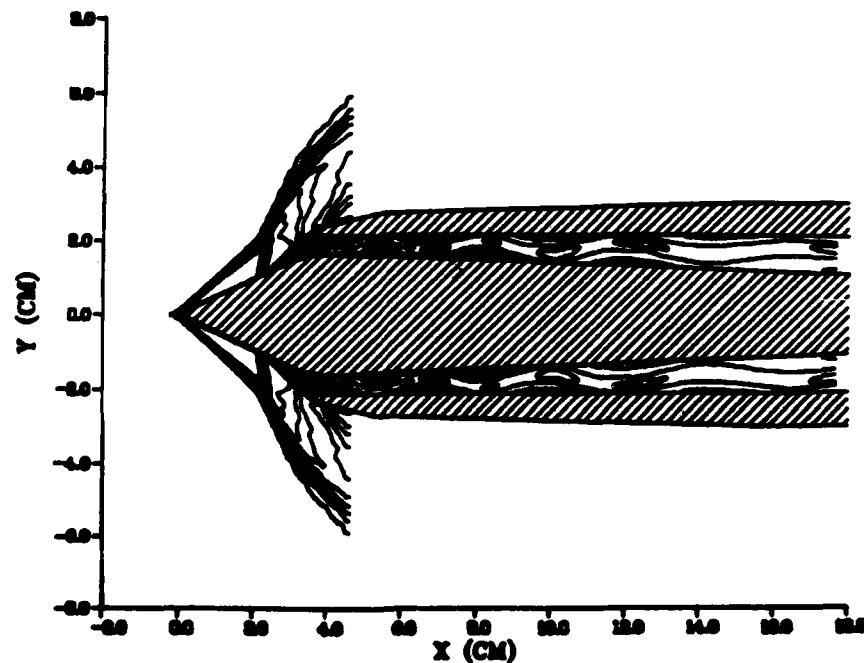
Fig. 28 Forebody Flow Field, Third Buzz Cycle
(TR=0.0, L/D=15.88)

MACH CONTOUR – TIME=.163E–01
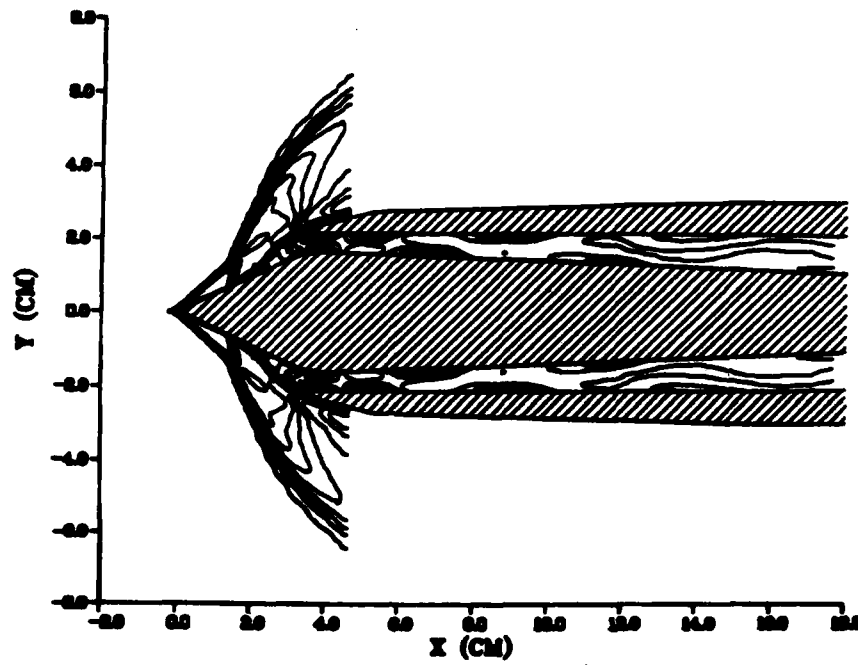
MACH CONTOUR – TIME=.165E–01
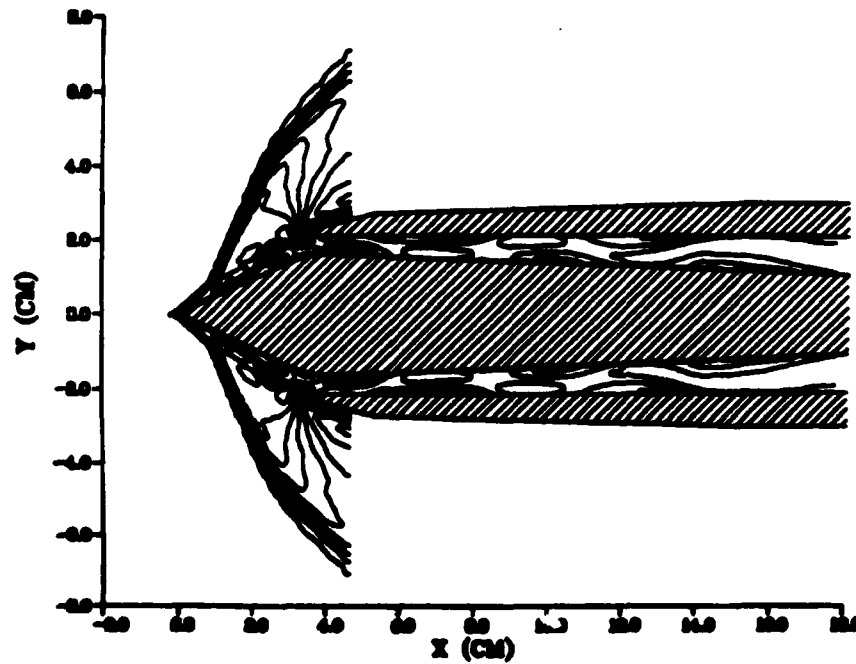
Fig. 28   (cont.)

MACH CONTOUR - TIME=.167E-01
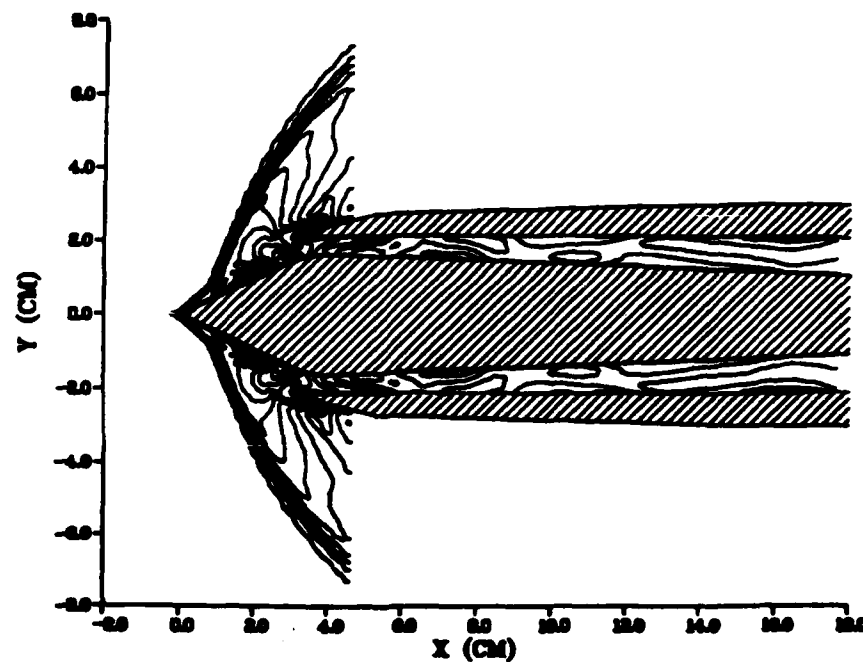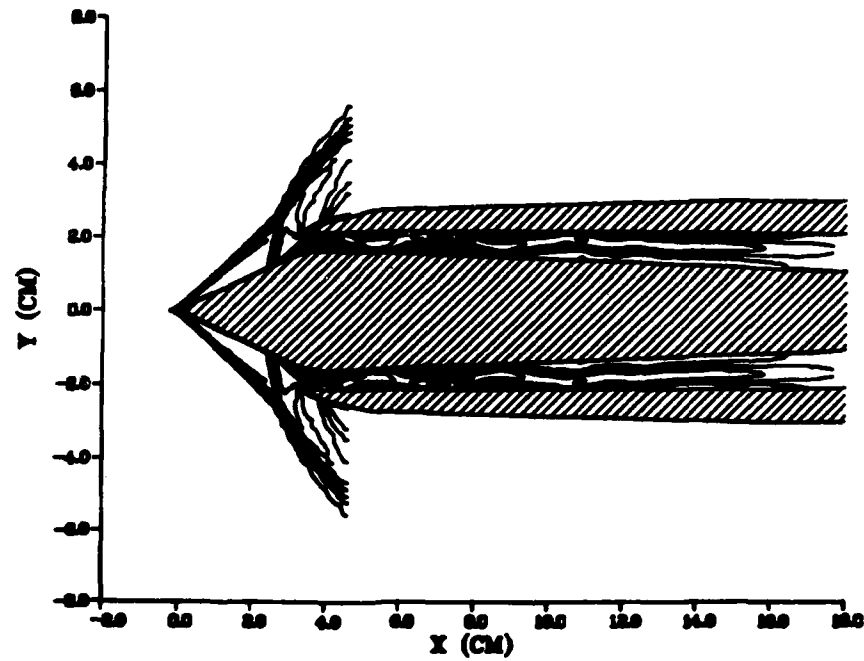
MACH CONTOUR - TIME=.169E-01

Fig. 28 (cont.)

106
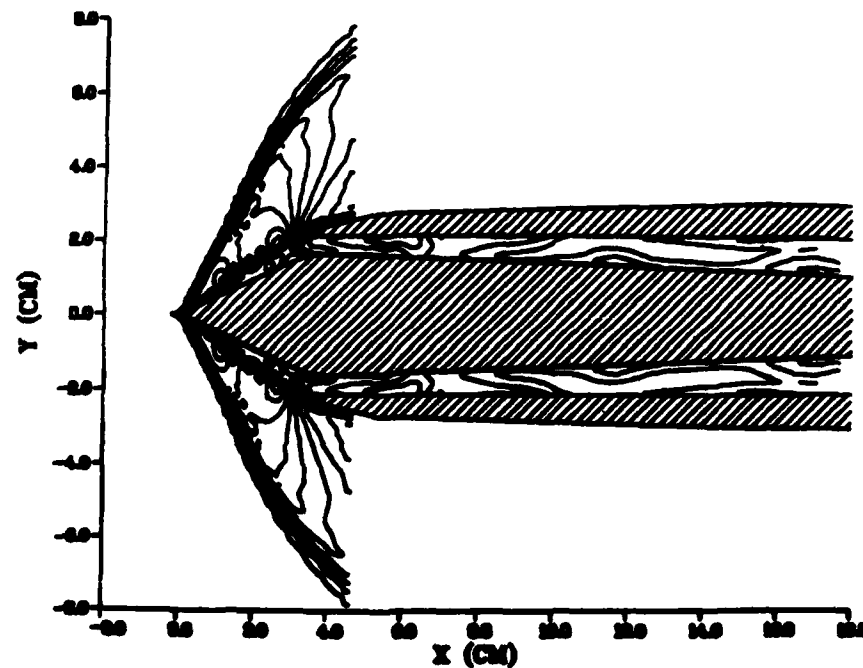
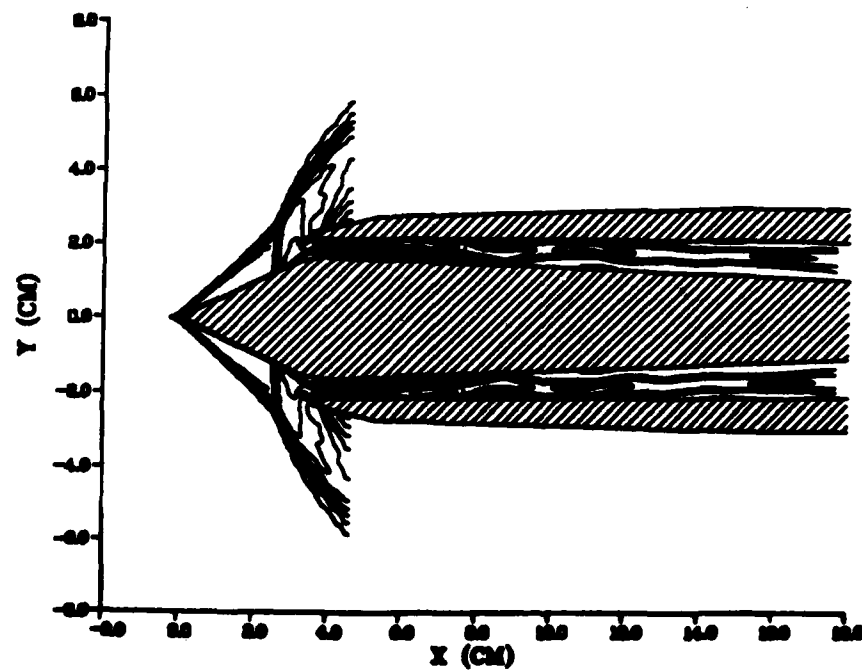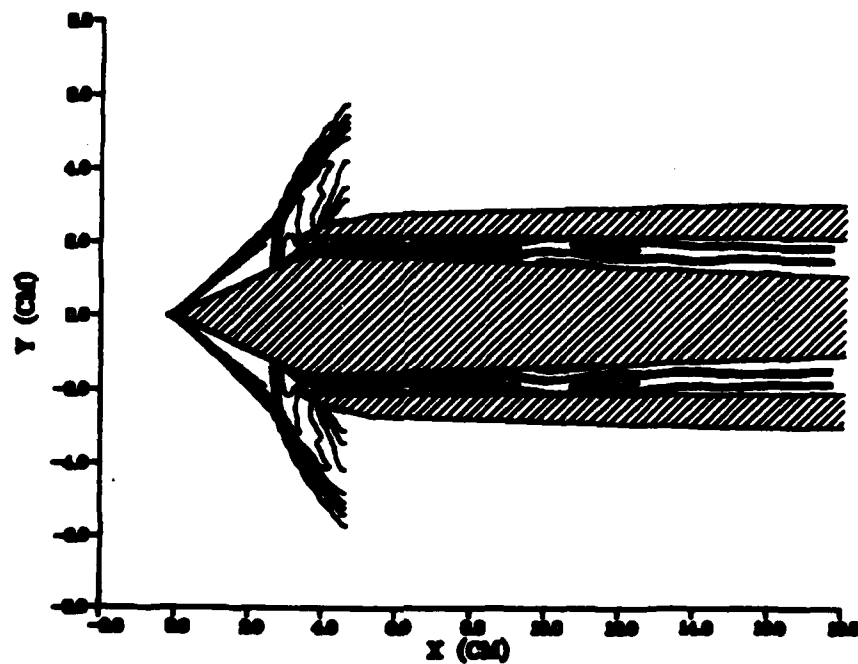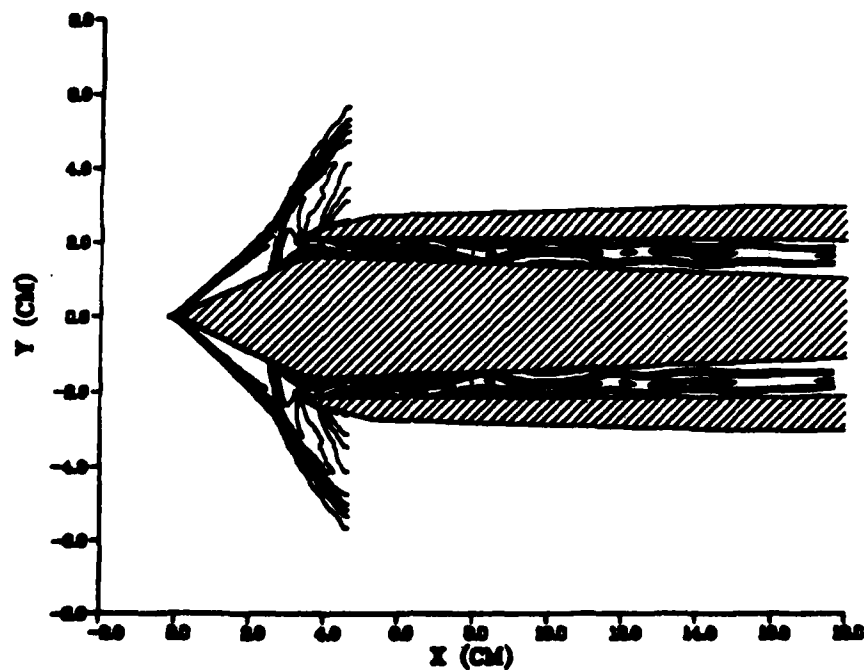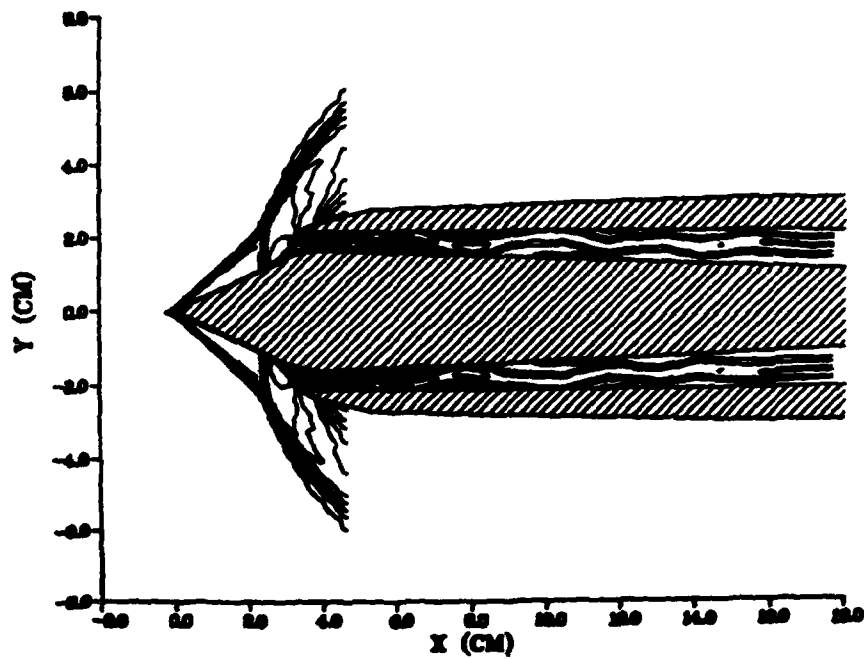MACH CONTOUR - TIME=.171E-01
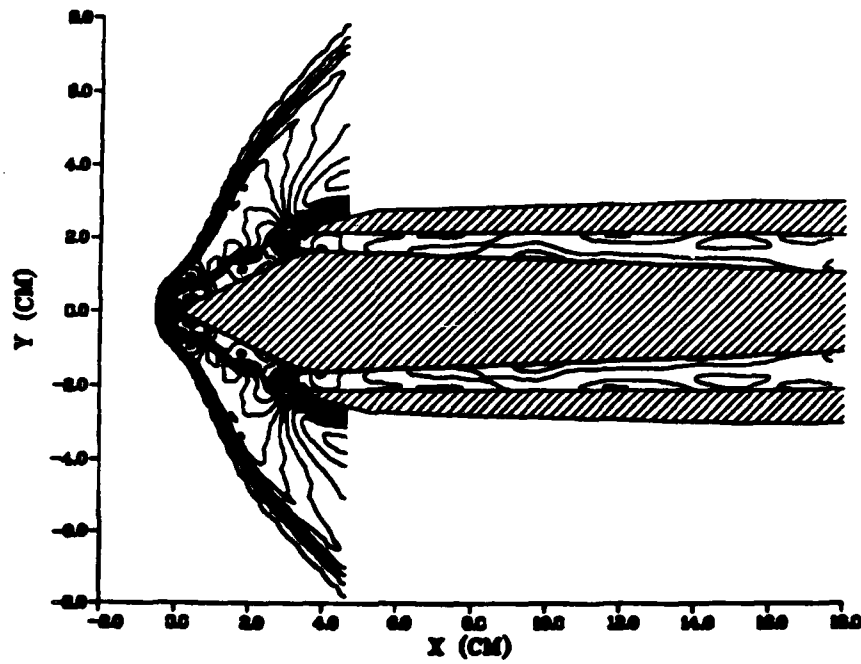
MACH CONTOUR - TIME=.173E-01

Fig. 28 (cont.)

107
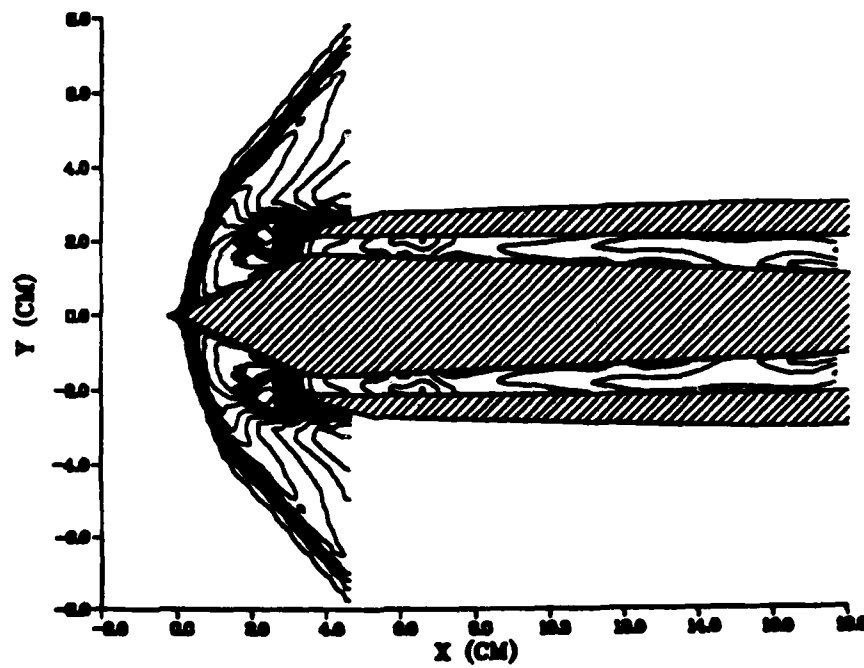
MACH CONTOUR – TIME=.175E-01
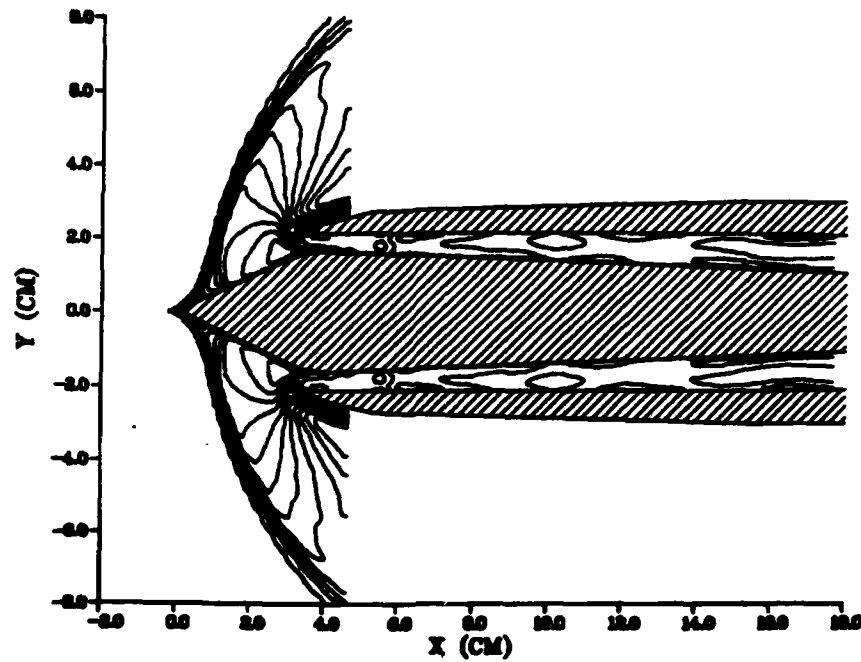
MACH CONTOUR – TIME=.177E-01

Fig. 28   (cont.)

108
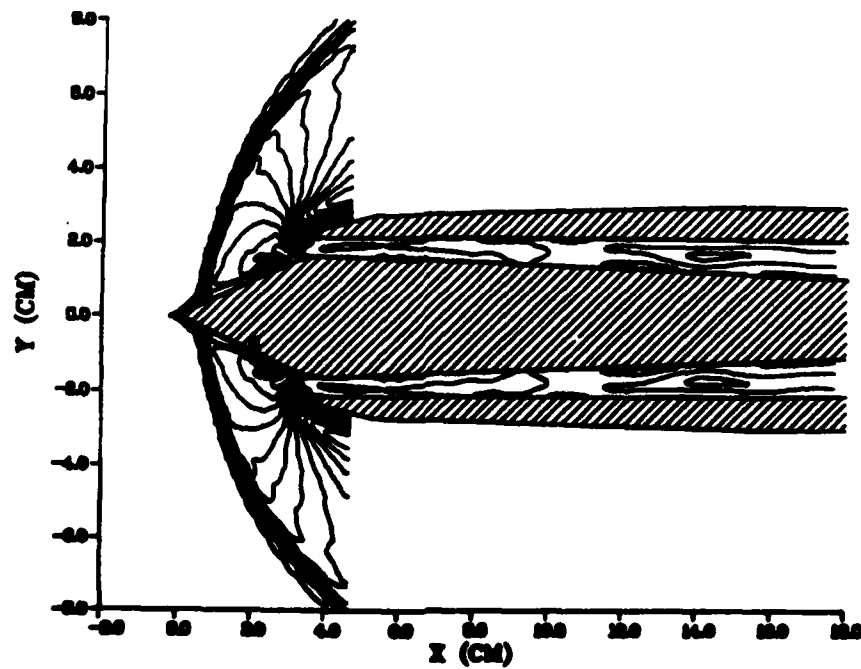
MACH CONTOUR — TIME=.179E-01
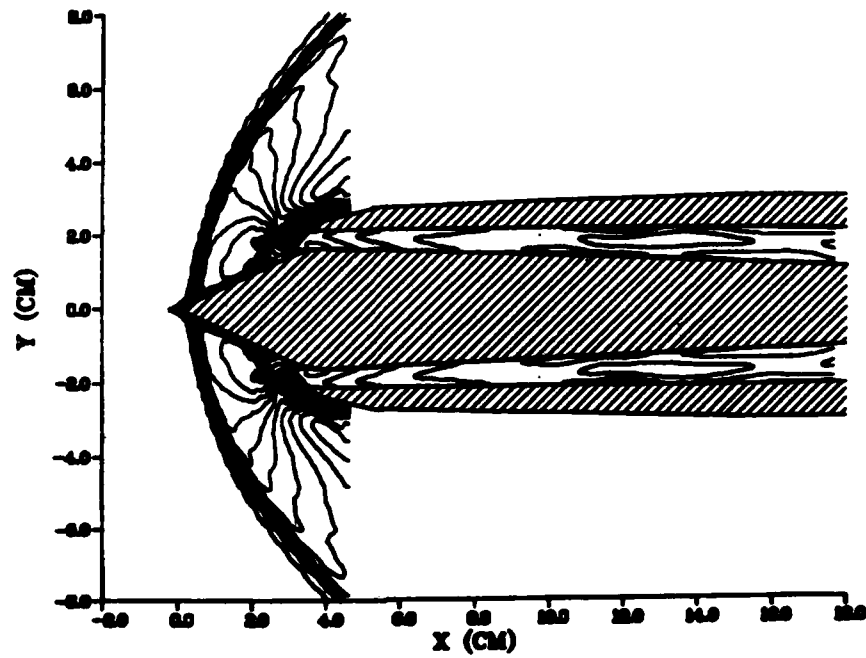
MACH CONTOUR — TIME=.181E-01

Fig. 28 (cont.)

109
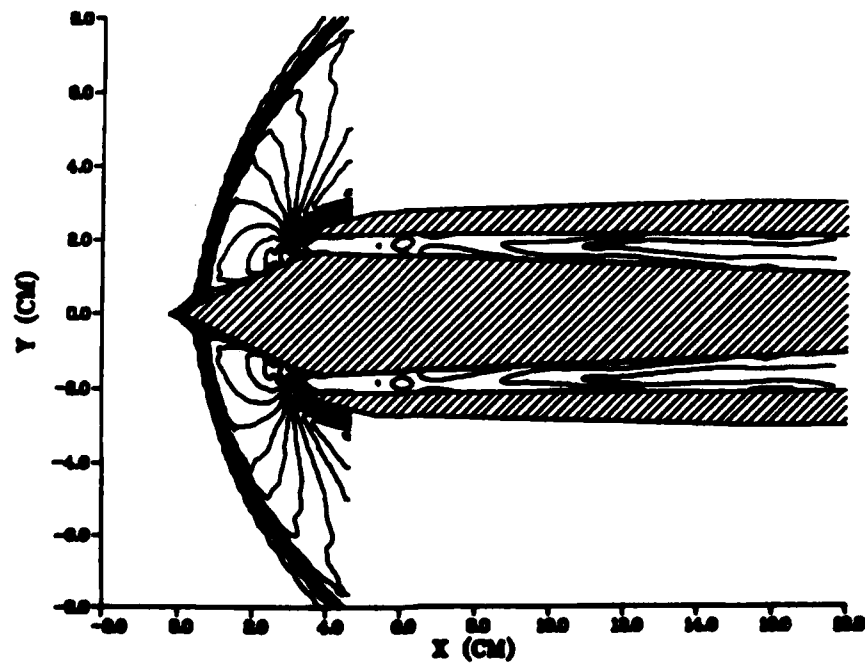
MACH CONTOUR – TIME=.183E–01
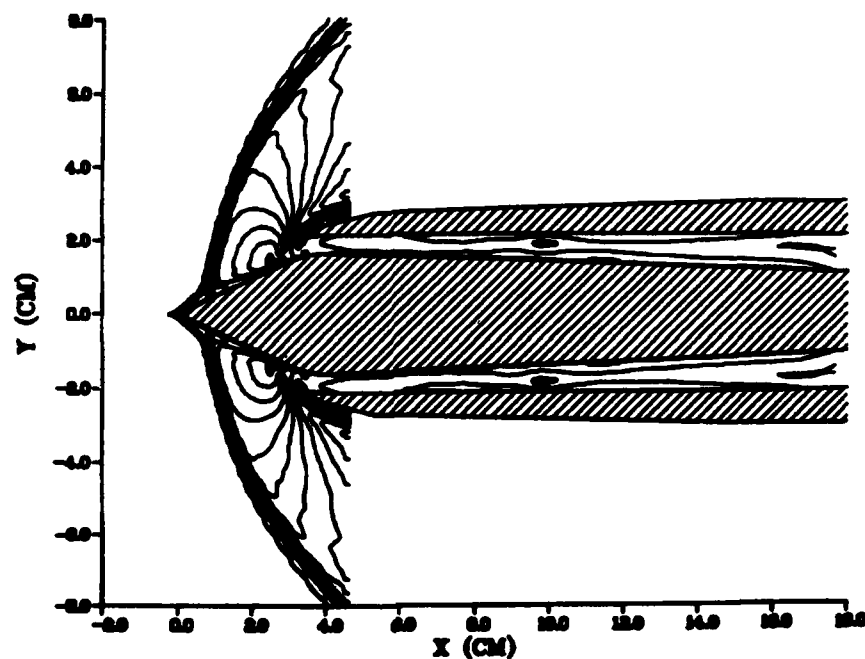
MACH CONTOUR – TIME=.185E–01

Fig. 28 (cont.)

110

MACH CONTOUR – TIME=.187E–01

MACH CONTOUR – TIME=.189E–01

Fig. 28 (cont.)

111

MACH CONTOUR — TIME=.191E−01

MACH CONTOUR — TIME=.193E−01

Fig. 28 (cont.)

112
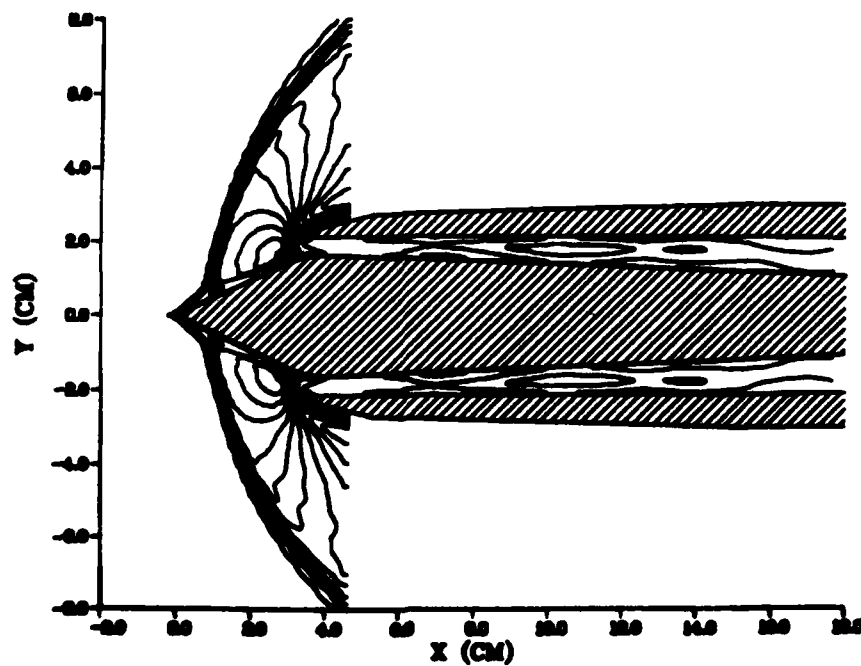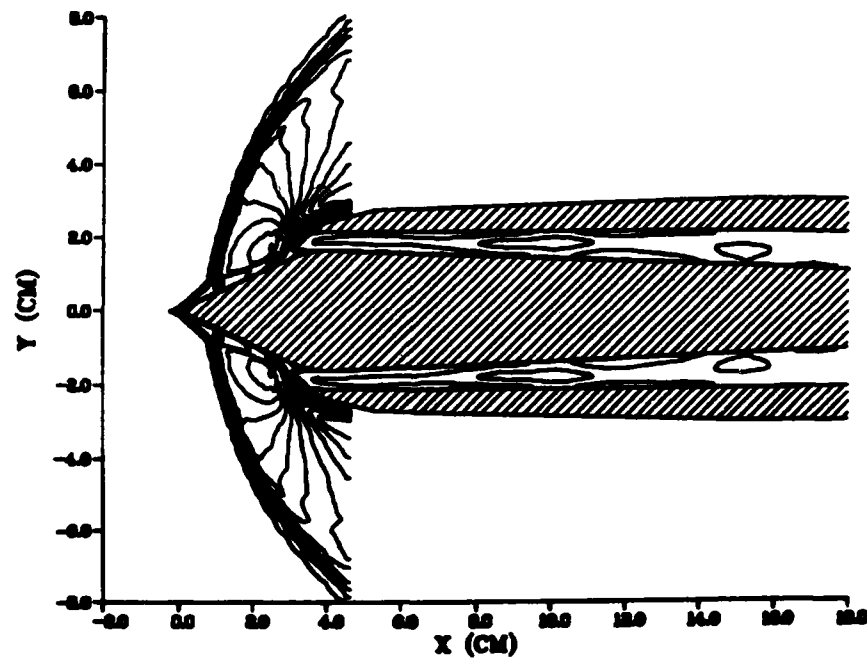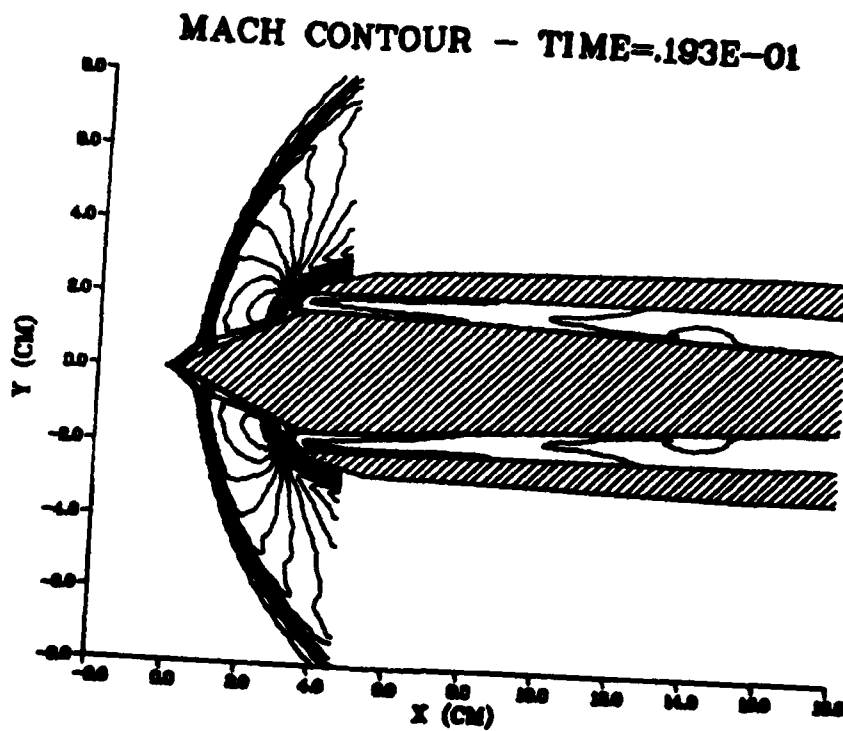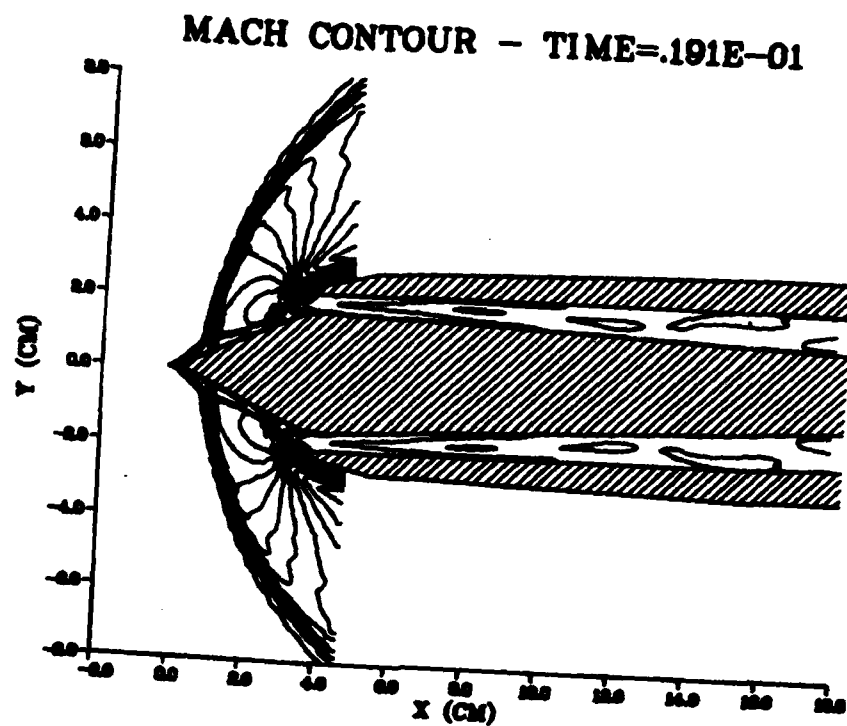
MACH CONTOUR – TIME=.195E–01
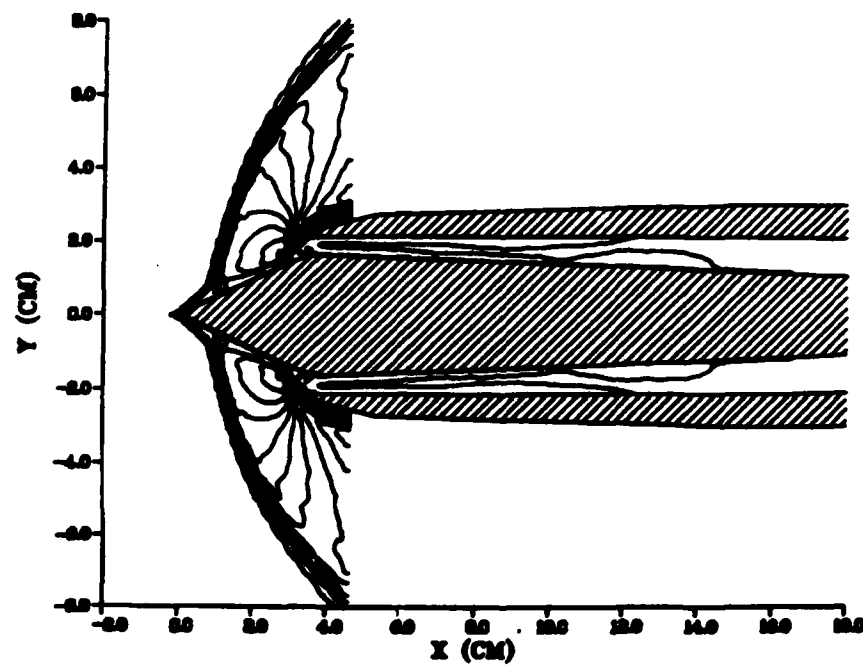
MACH CONTOUR – TIME=.197E–01

Fig. 28 (cont.)

113
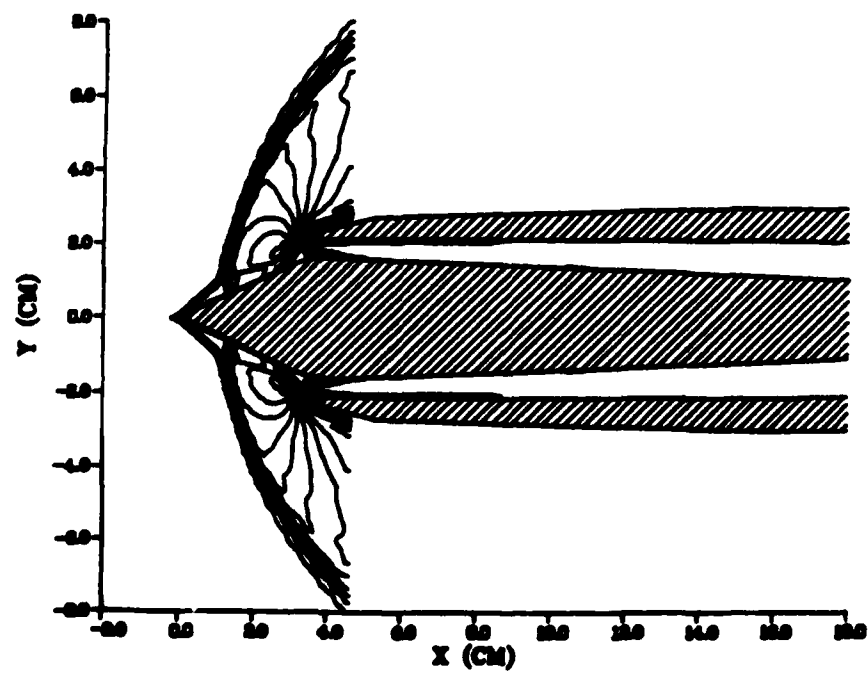
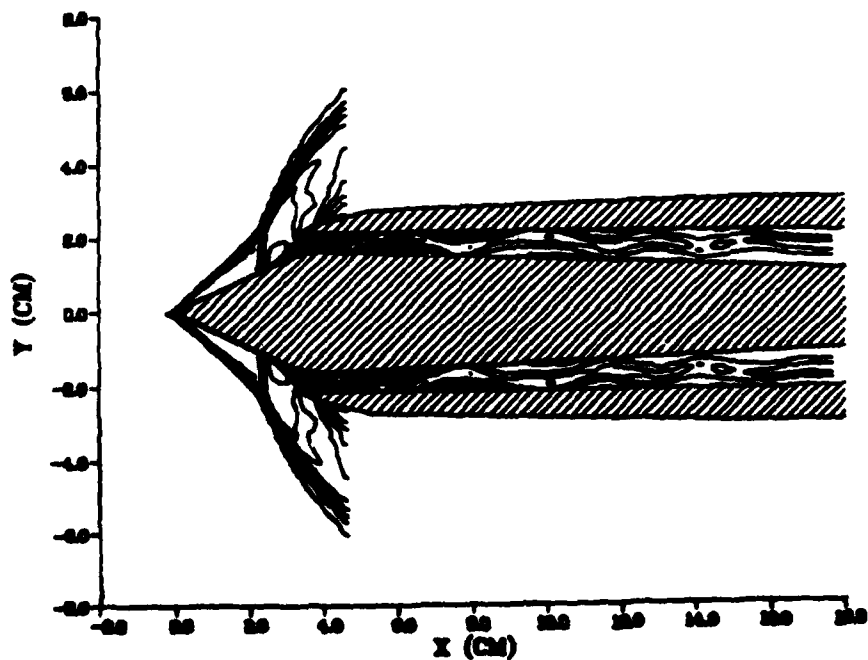MACH CONTOUR – TIME=.199E–01
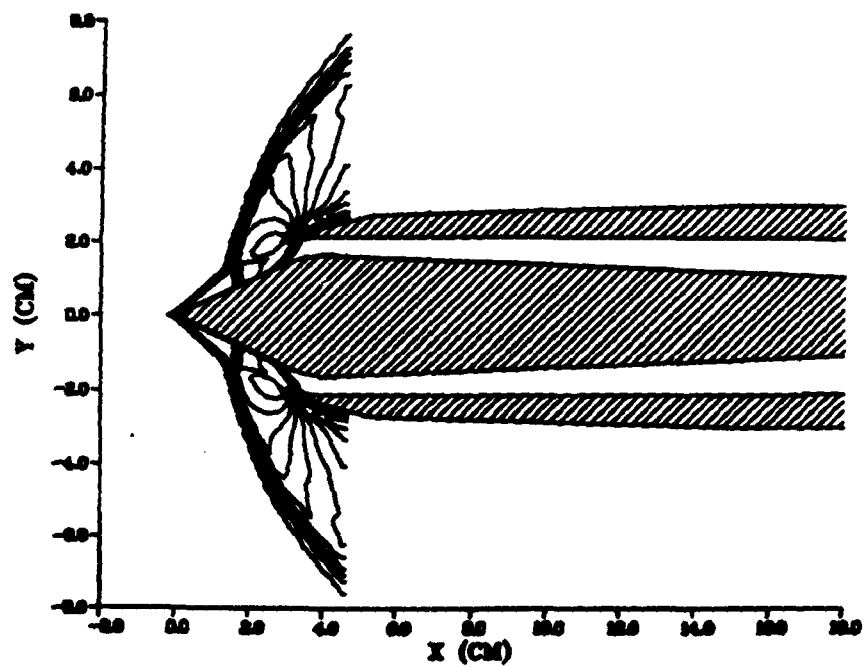
MACH CONTOUR – TIME=.201E–01

Fig. 28 (cont.)

114
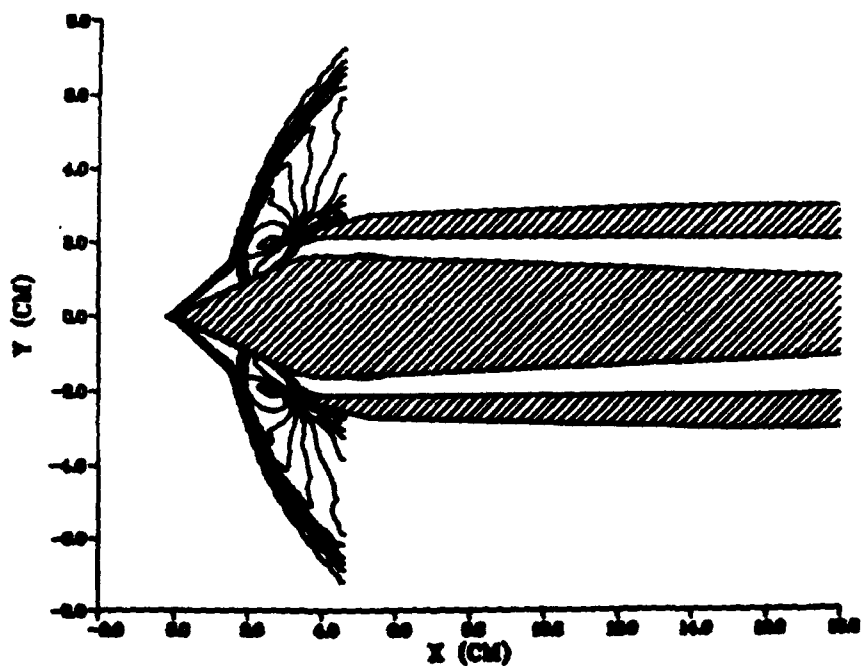
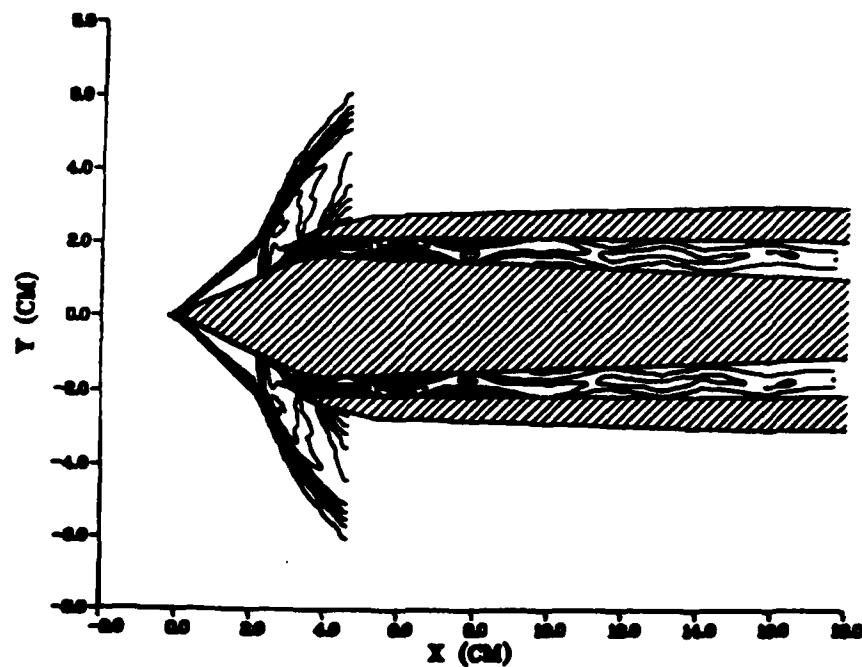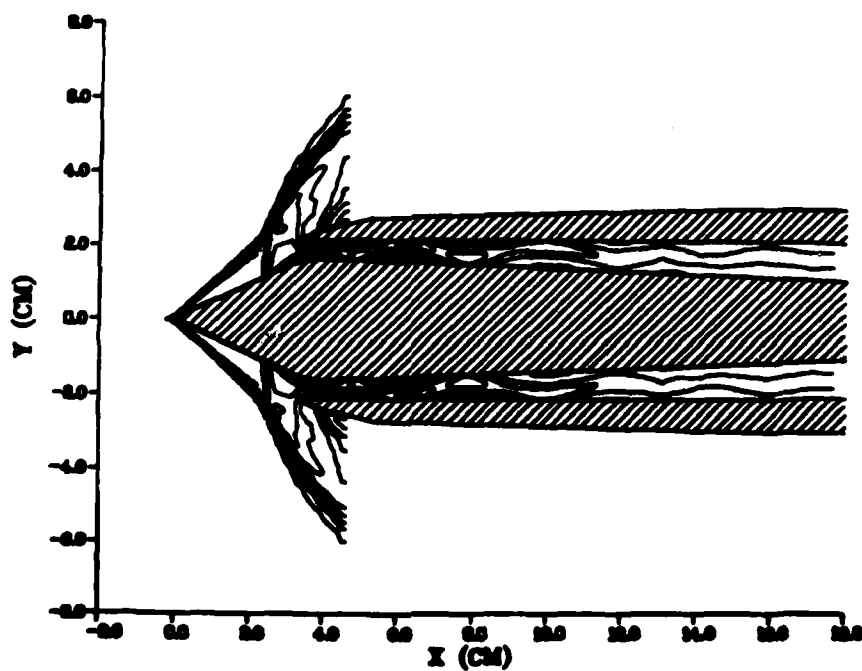MACH CONTOUR - TIME=.203E-01
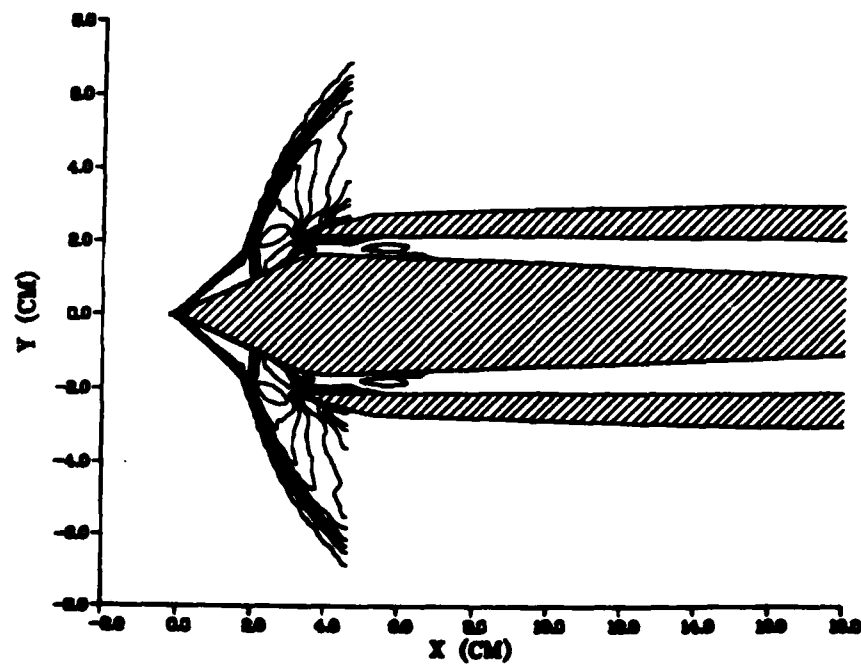
MACH CONTOUR - TIME=.205E-01

Fig. 28 (cont.)

115
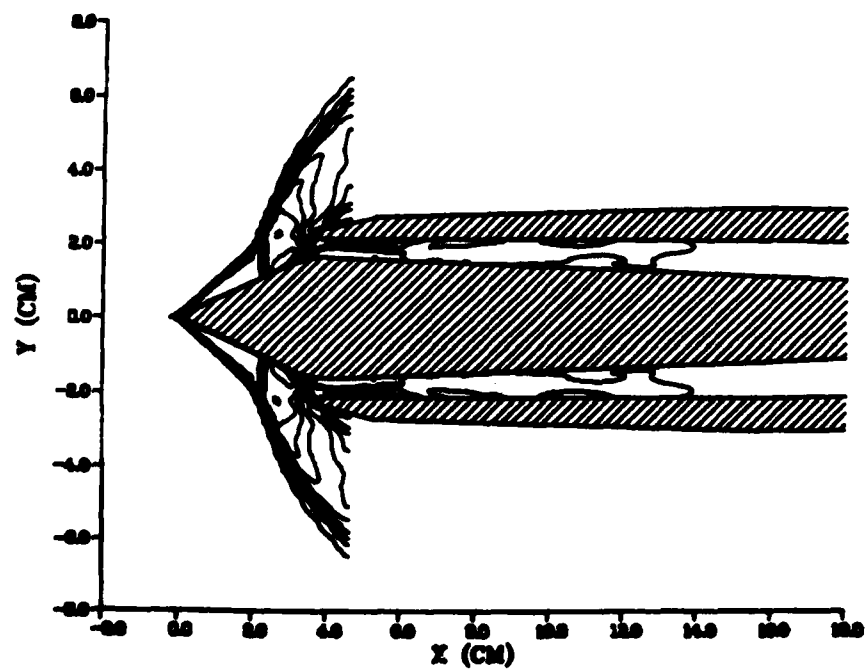
MACH CONTOUR - TIME=.207E-01
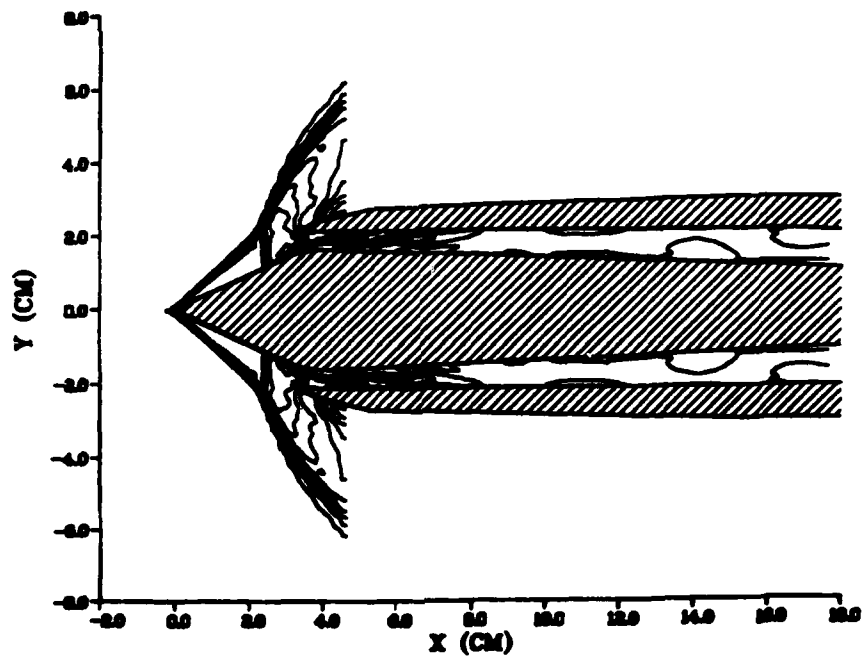
MACH CONTOUR - TIME=.209E-01

Fig. 28   (cont.)

116
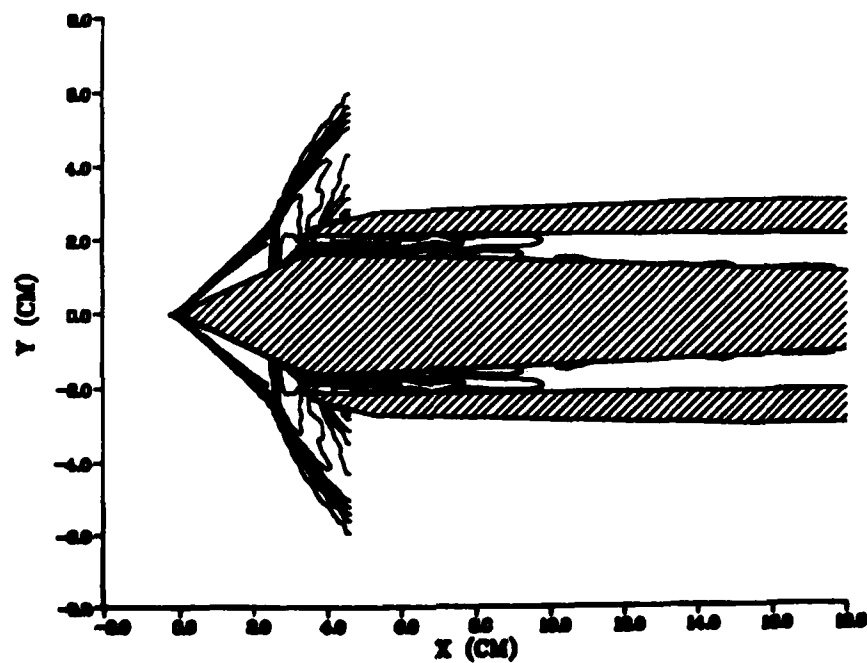
MACH CONTOUR — TIME=.211E—01
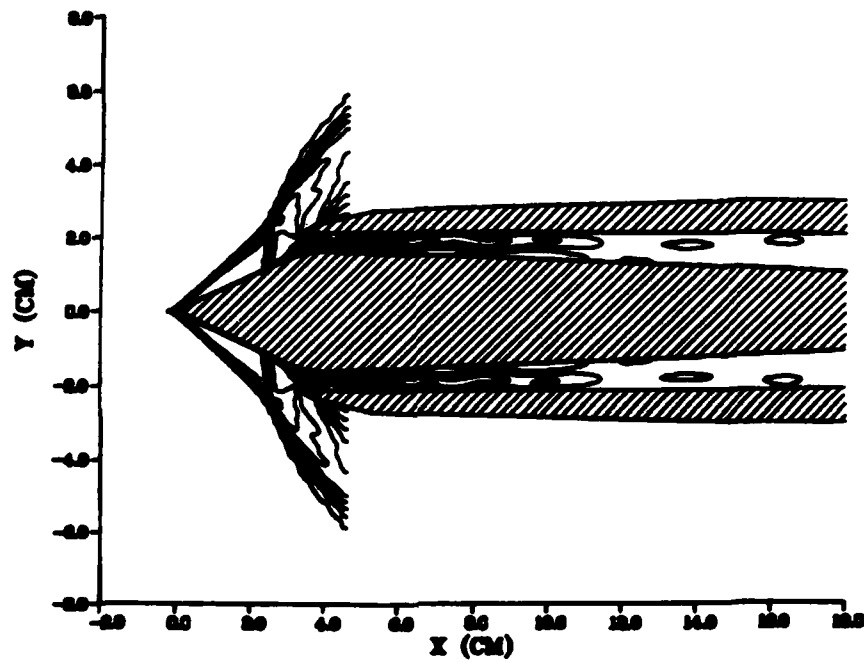
MACH CONTOUR — TIME=.213E—01
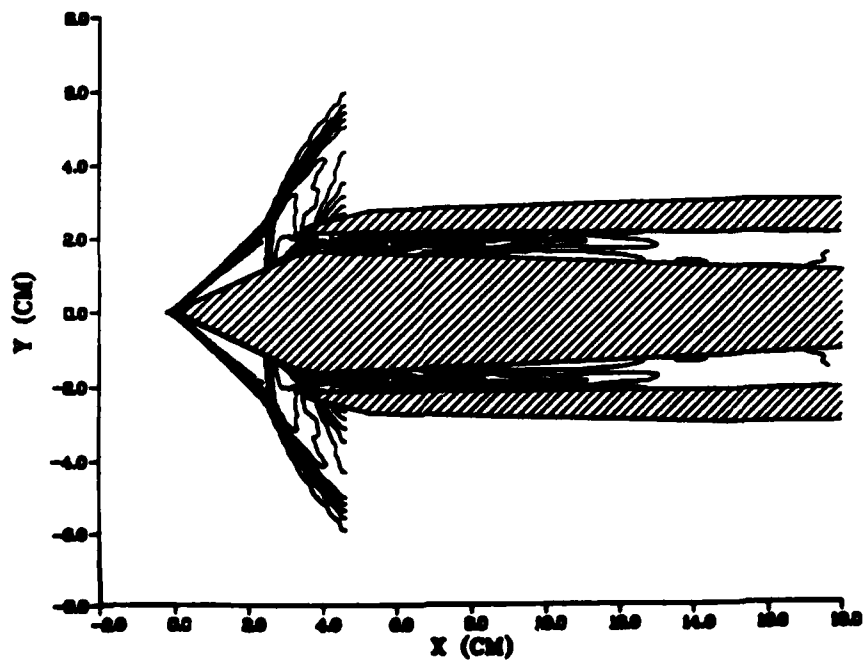
Fig. 28   (cont.)

MACH CONTOUR – TIME=.215E–01
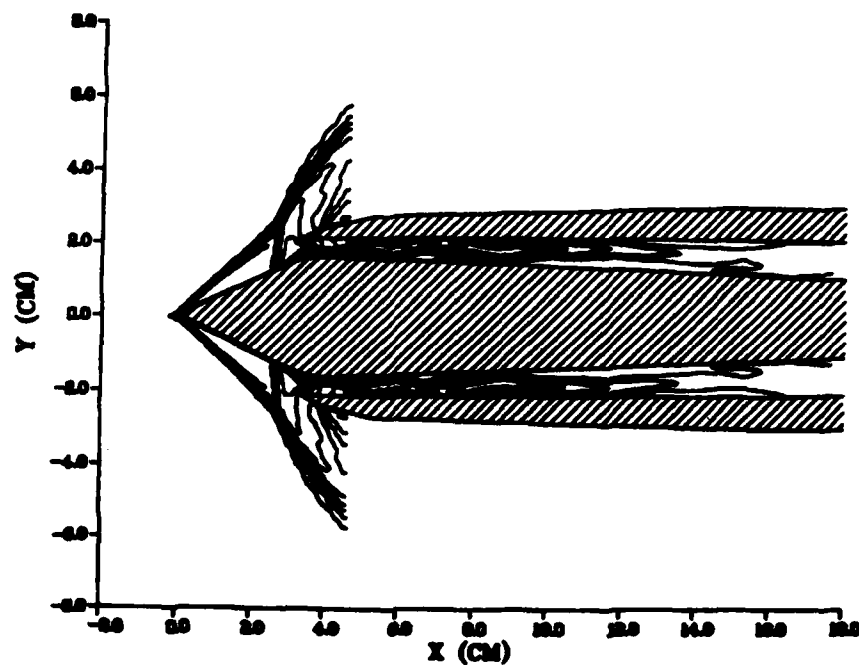
MACH CONTOUR – TIME=.217E–01

Fig. 28 (cont.)

118
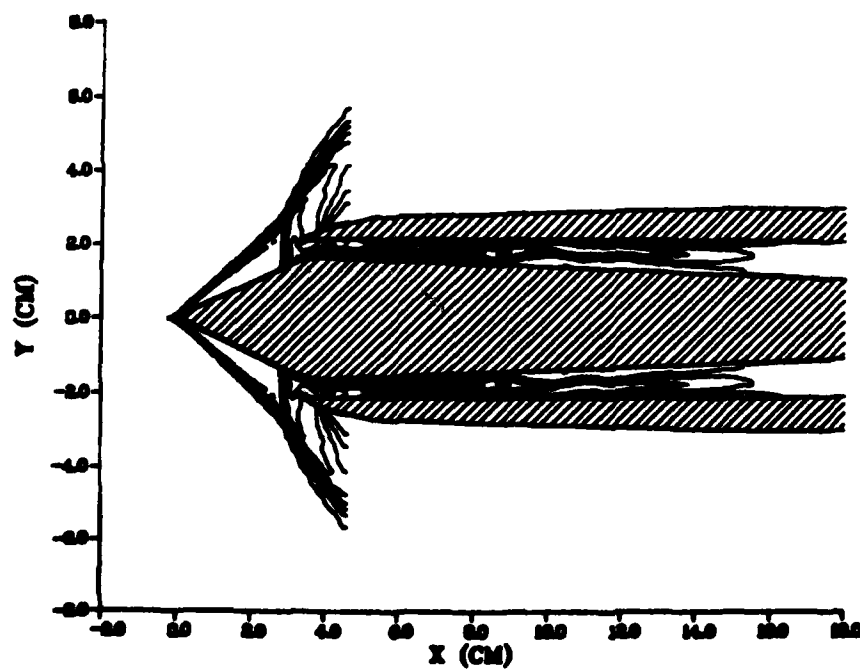
MACH CONTOUR – TIME=.219E-01

MACH CONTOUR – TIME=.221E-01

Fig. 28 (cont.)

119

MACH CONTOUR – TIME=.223E–01

MACH CONTOUR – TIME=.225E–01

Fig. 28   (cont.)

MACH CONTOUR — TIME=.227E-01
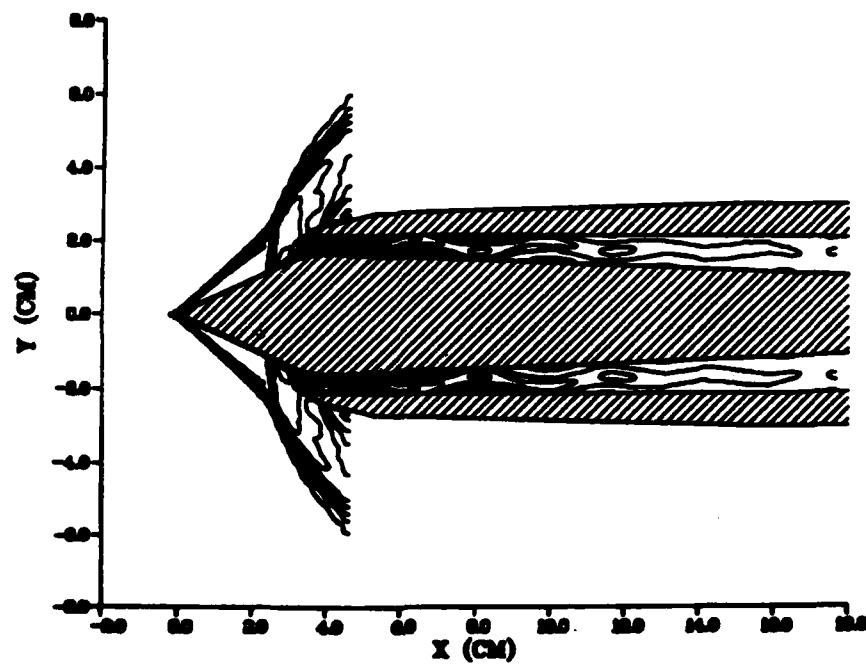
MACH CONTOUR — TIME=.229E-01

Fig. 28   (cont.)

121

MACH CONTOUR – TIME=.231E–01

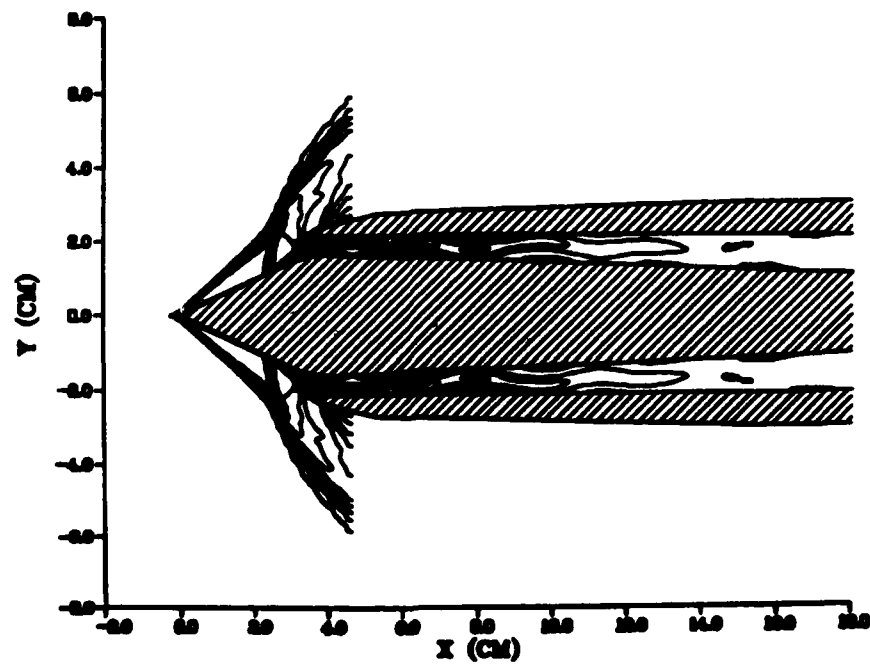## MACH CONTOUR – TIME=.233E–01

Fig. 28   (cont.)

122

MACH CONTOUR – TIME=.235E–01

MACH CONTOUR – TIME=.237E–01

Fig. 28   (cont.)

123

MACH CONTOUR — TIME=.239E—01

Fig. 28   (cont.)

124

VELOCITY – TIME=.159E–01

VELOCITY – TIME=.163E–01
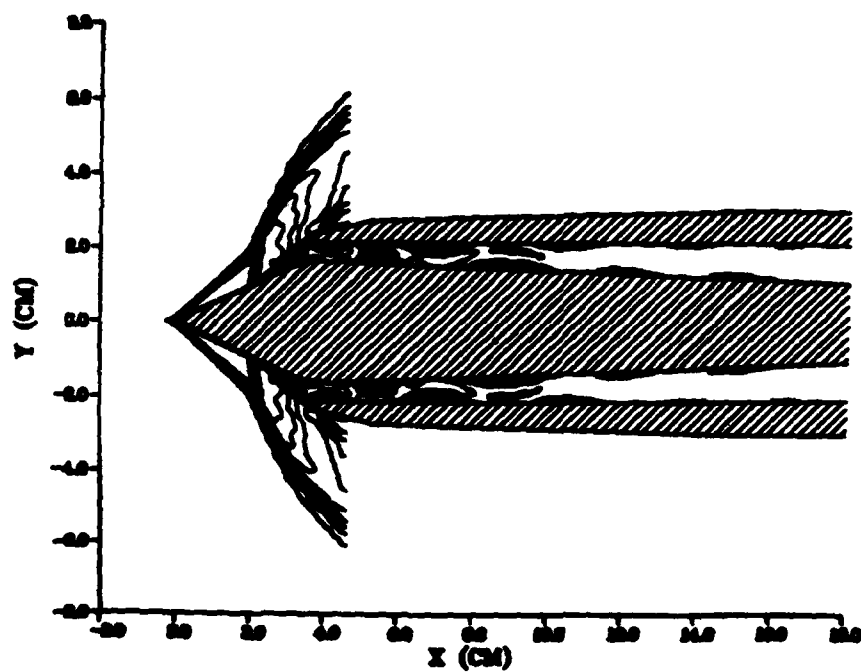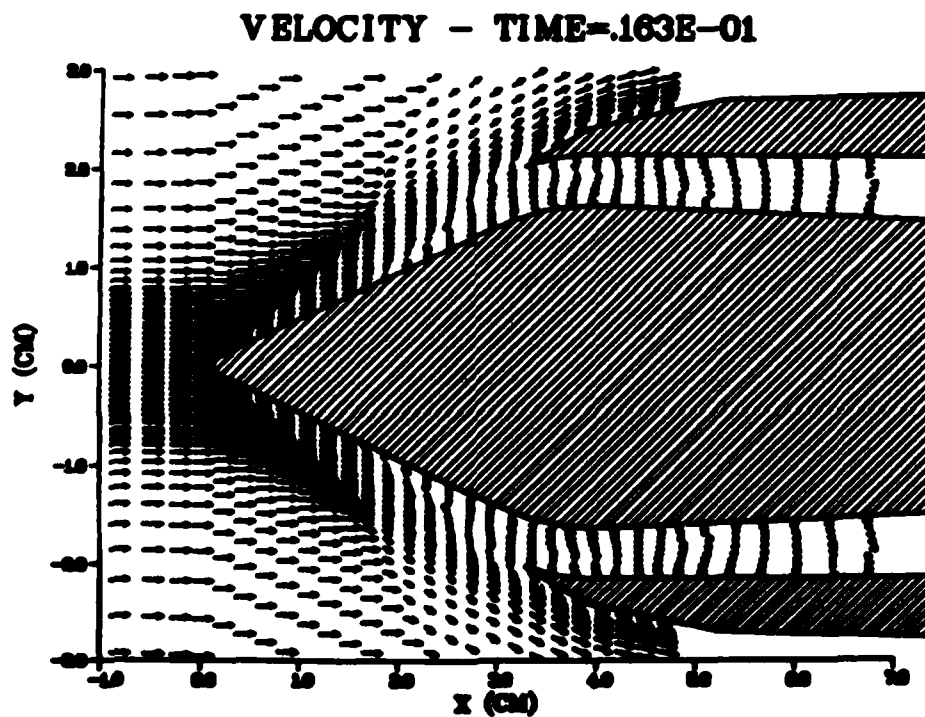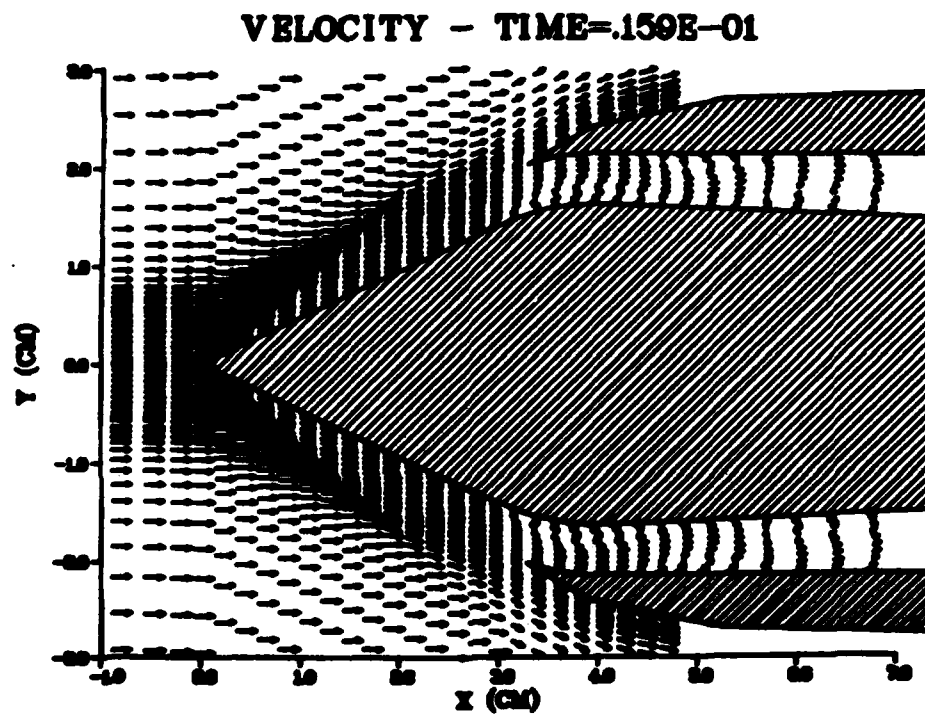

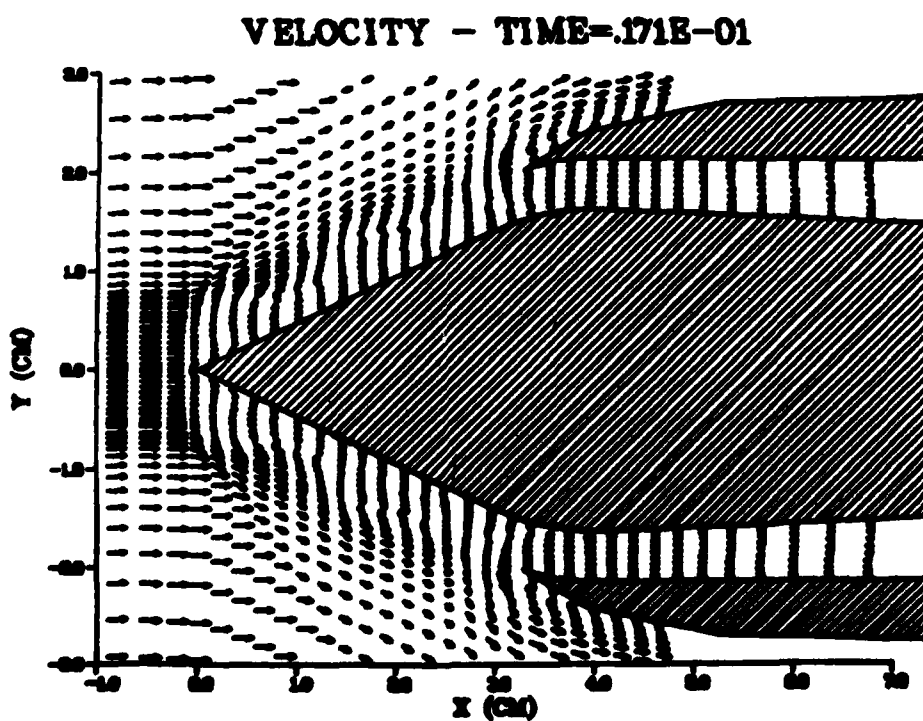Fig. 29   Forebody Flow Field, Third Buzz Cycle
(TR=0.0, L/D=15.88)

125

VELOCITY — TIME=.167E—01

VELOCITY — TIME=.171E—01

Fig. 29 (cont.)

126

VELOCITY – TIME=.175E–01

VELOCITY – TIME=.179E–01

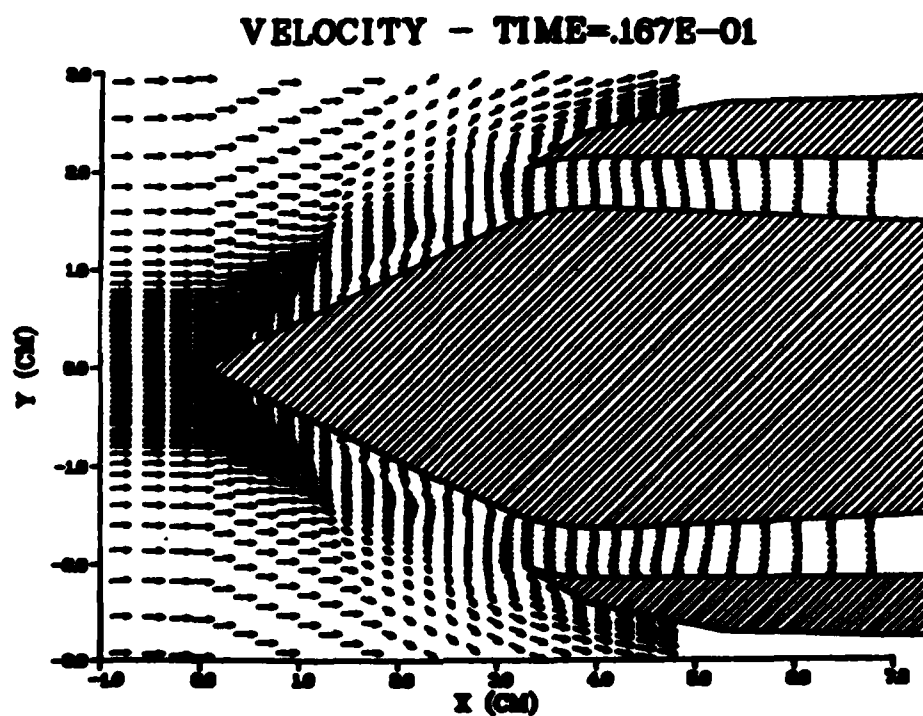Fig. 29 (cont.)

127

VELOCITY - TIME=.163E-01

VELOCITY - TIME=.167E-01

Fig. 29 (cont.)

128

VELOCITY - TIME=.191E-01

VELOCITY - TIME=.195E-01

Fig. 29   (cont.)

129
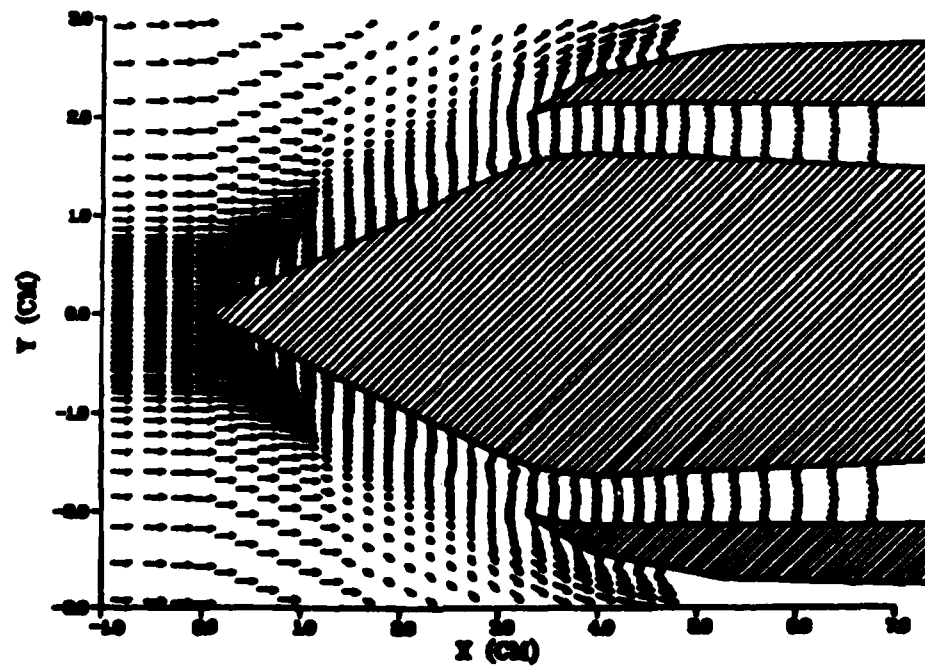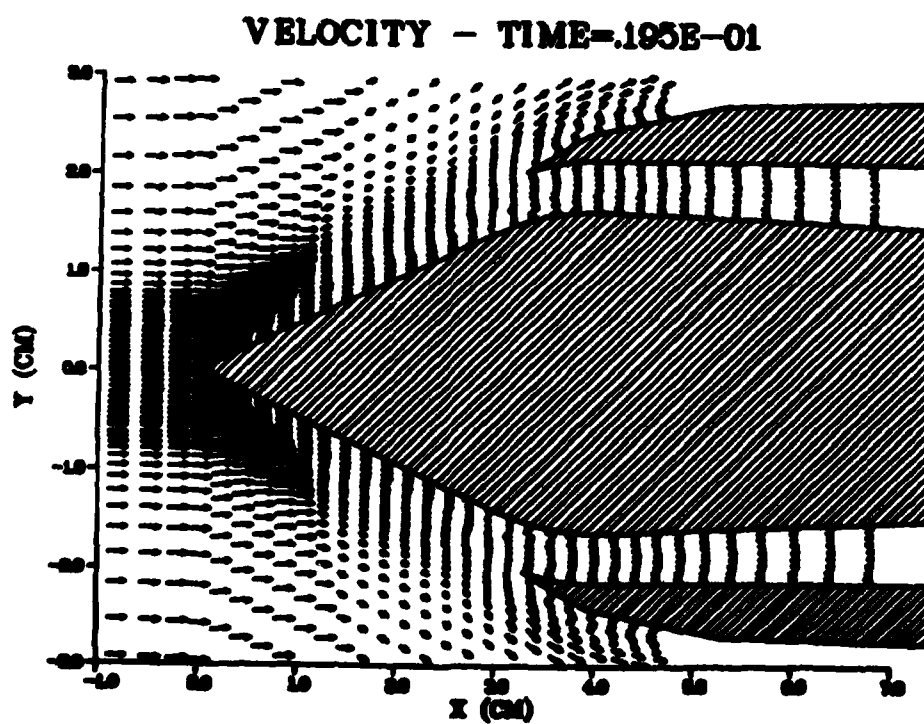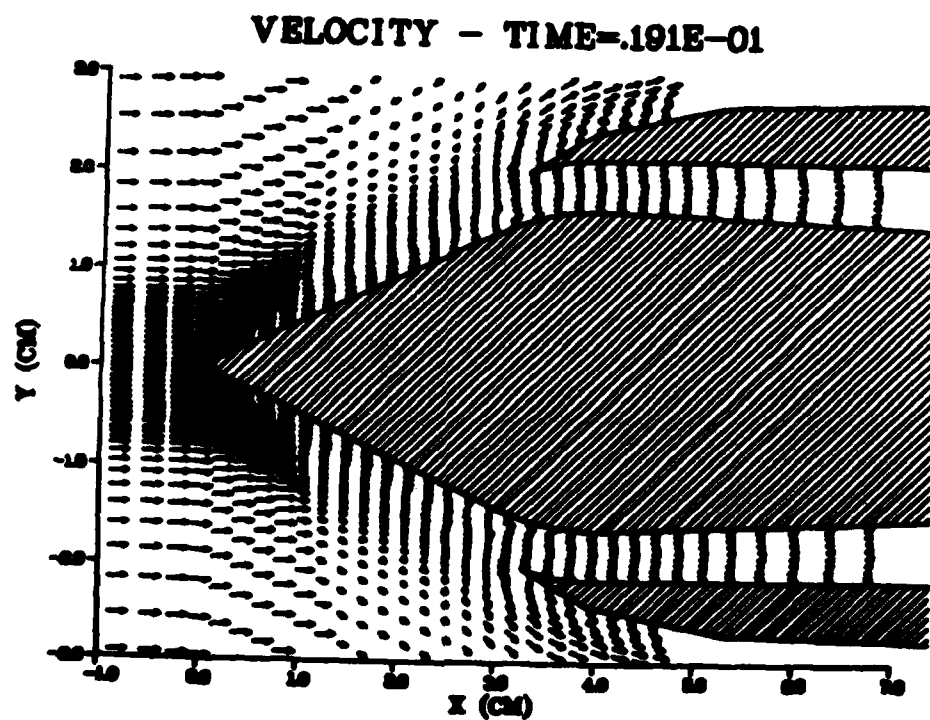
VELOCITY — TIME=.199E—01
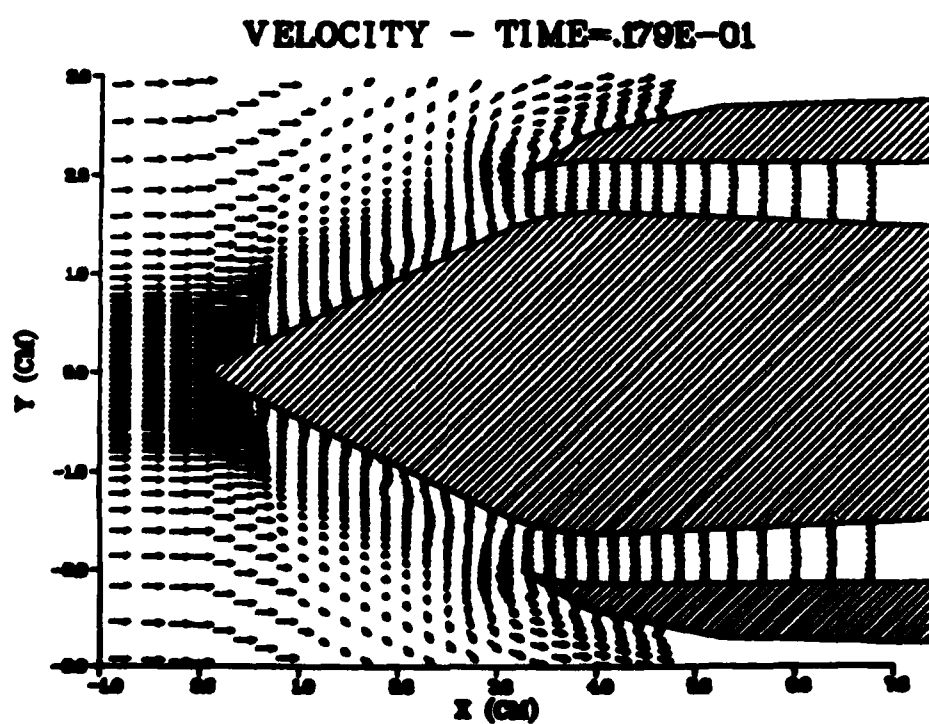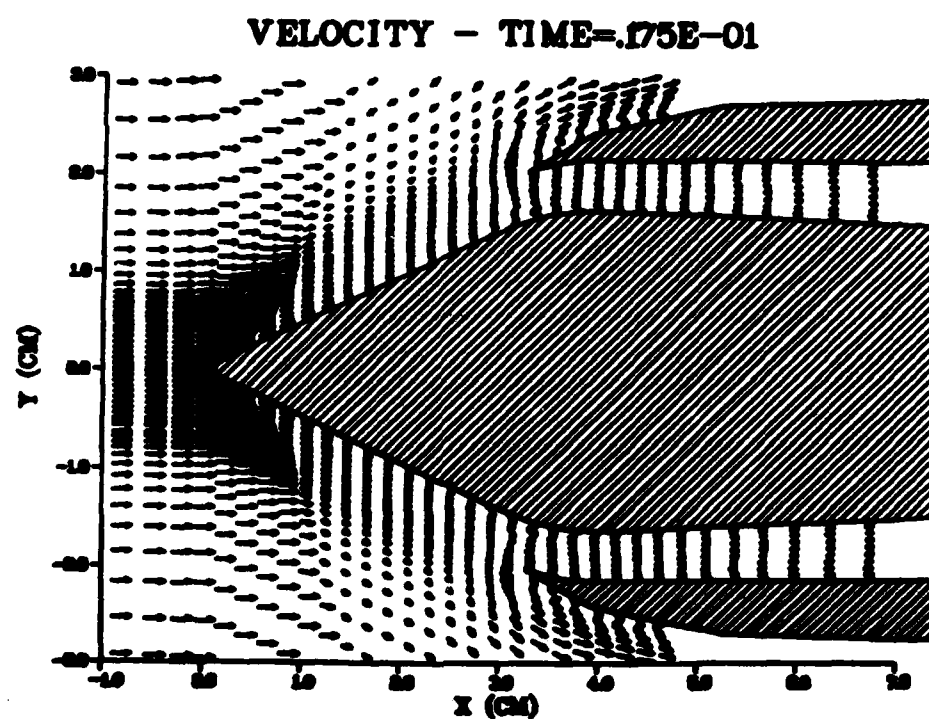

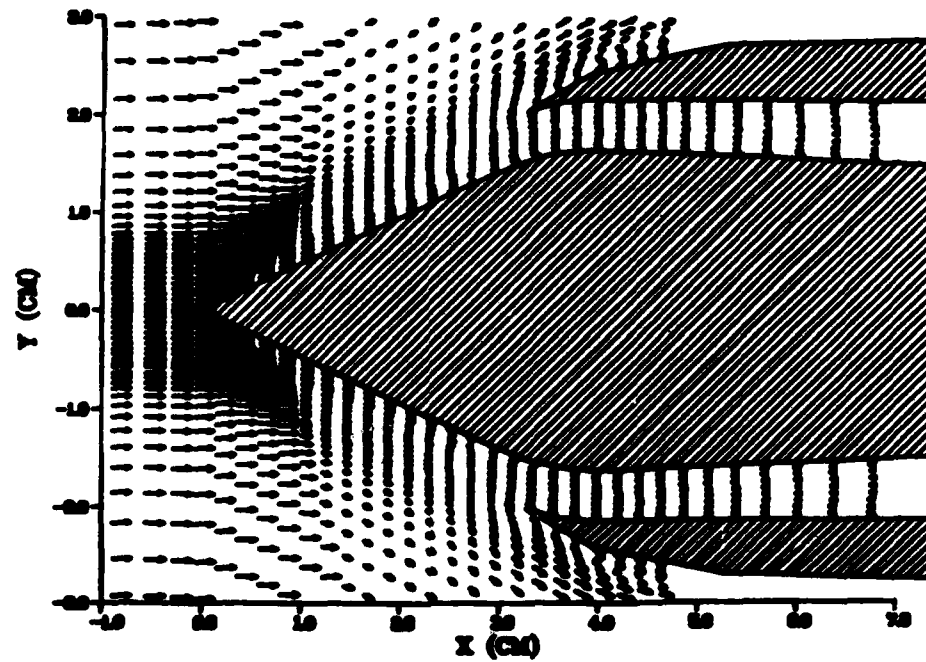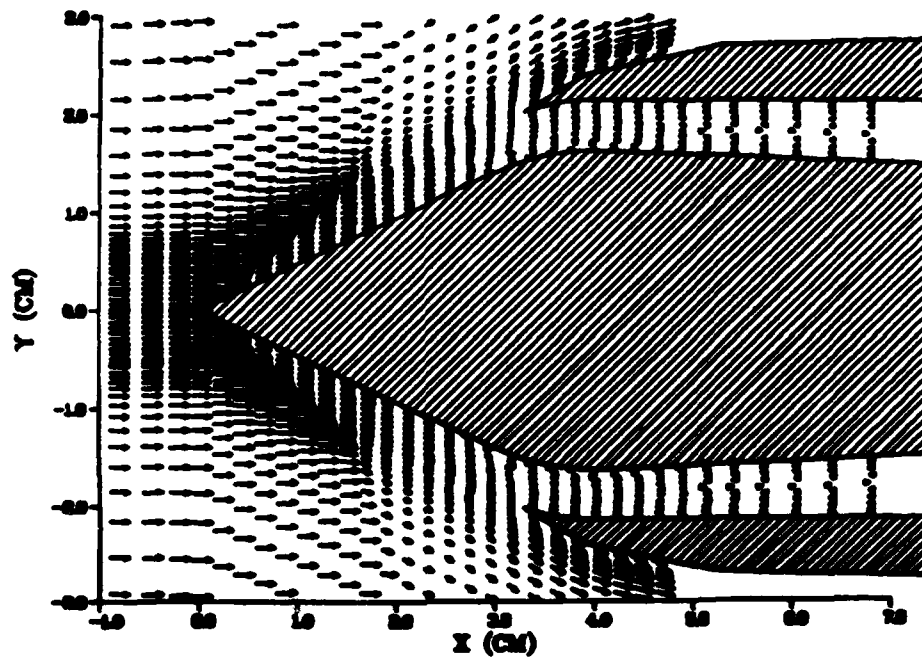**VELOCITY — TIME=.203E—01**

Fig. 29 (cont.)

130
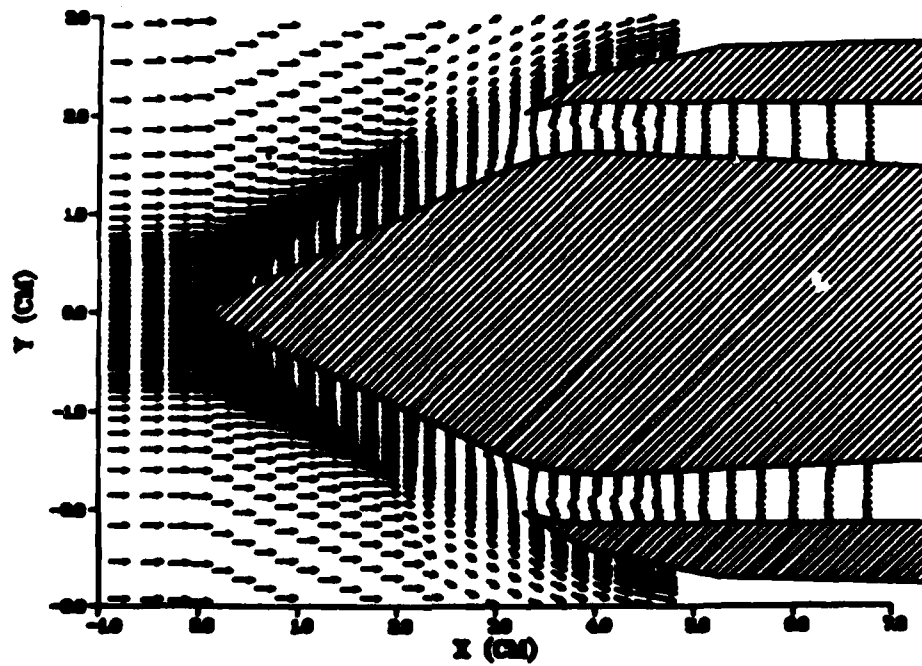
VELOCITY - TIME=.207E-01
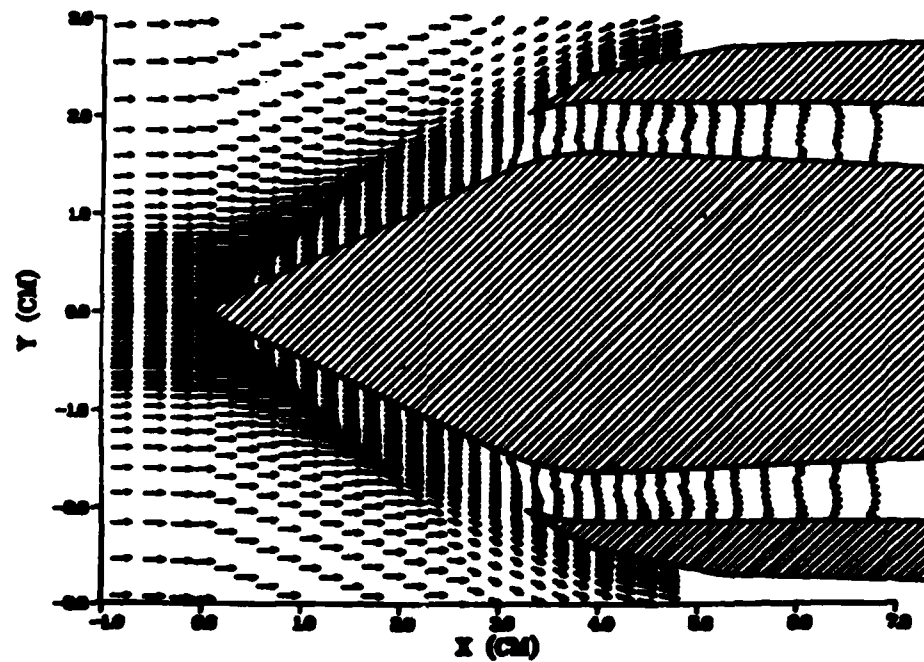
VELOCITY - TIME=.211E-01

Fig. 29 (cont.)

131

VELOCITY – TIME=.215E–01

VELOCITY – TIME=.219E–01

Fig. 29 (cont.)

132
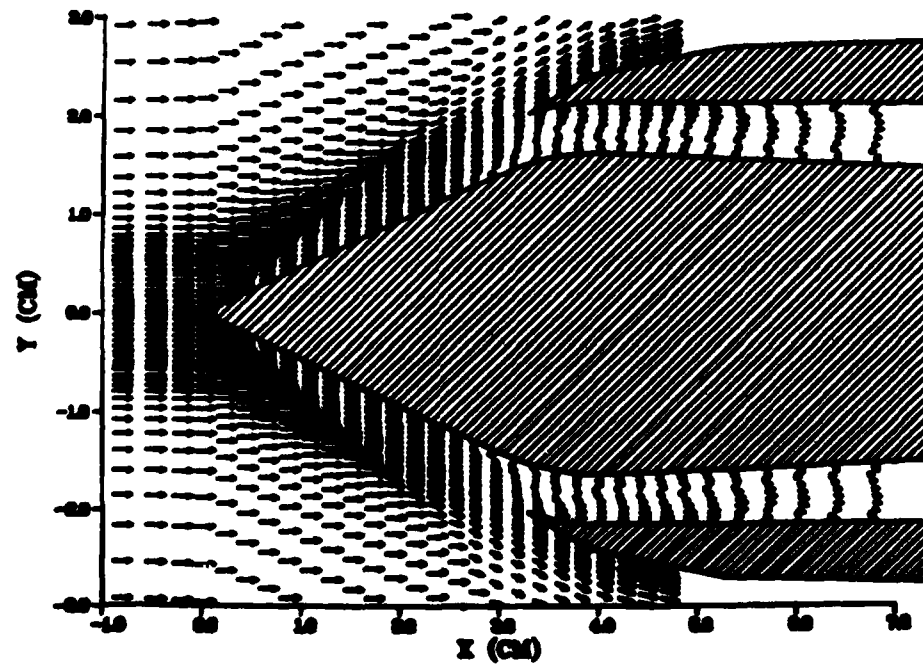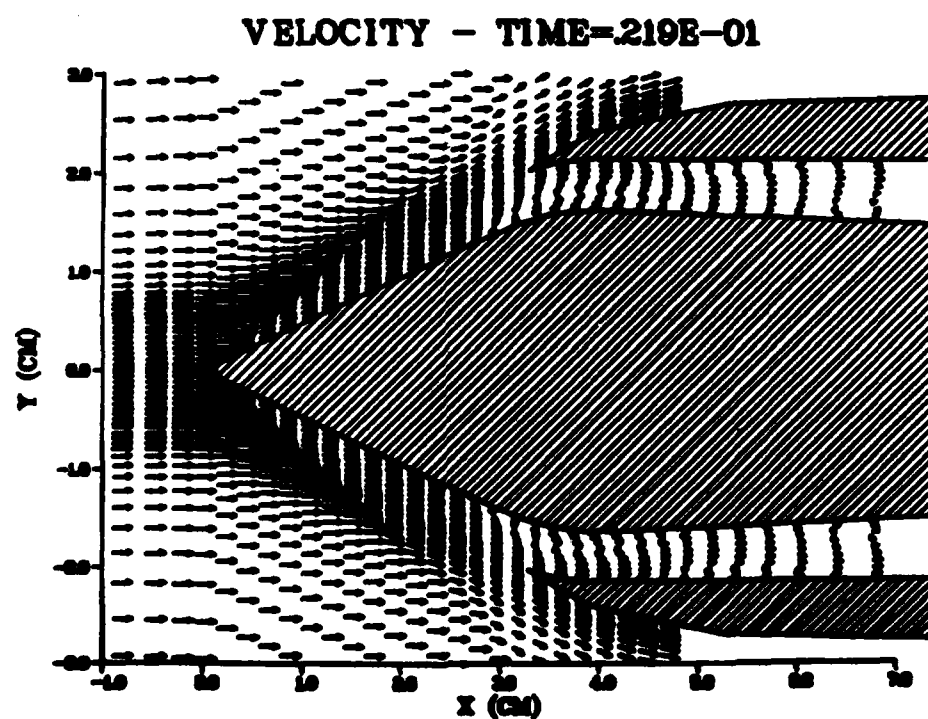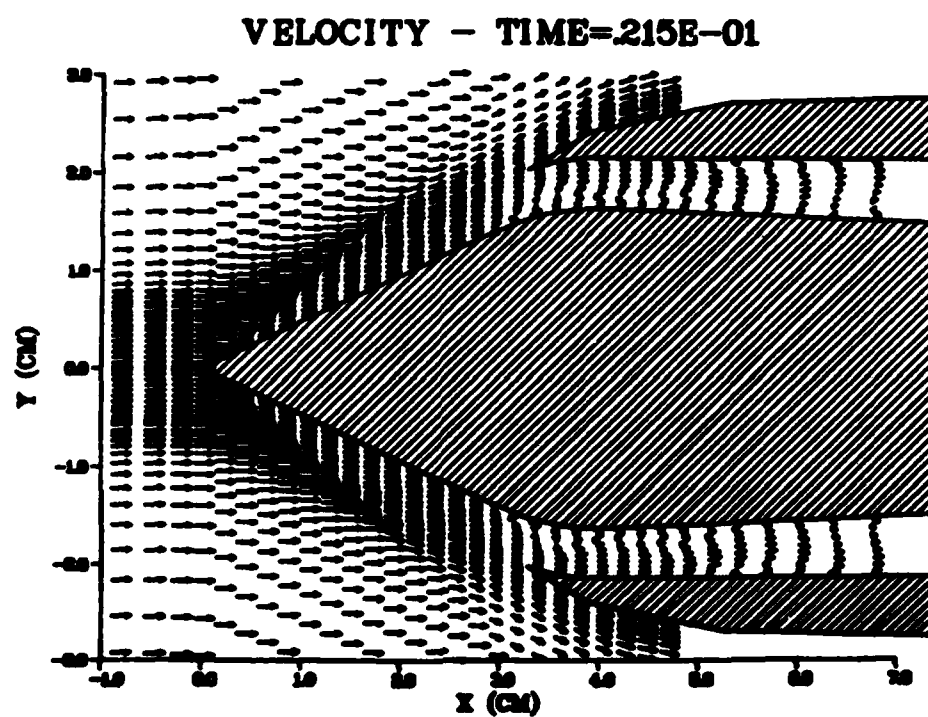
VELOCITY – TIME=.223E–01
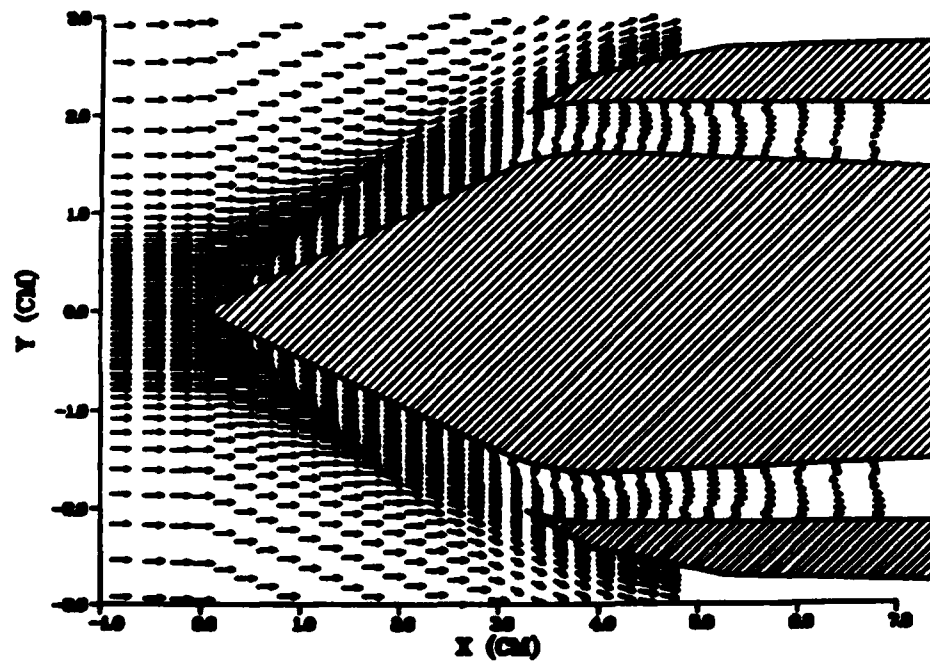
VELOCITY – TIME=.227E–01

Fig. 29 (cont.)

133
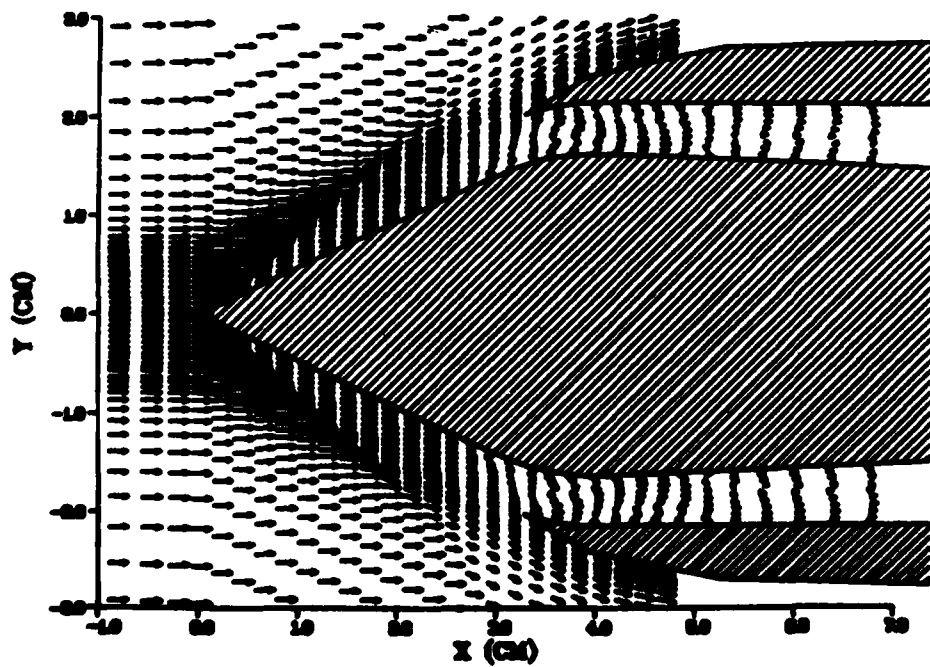
VELOCITY — TIME=.231E−01
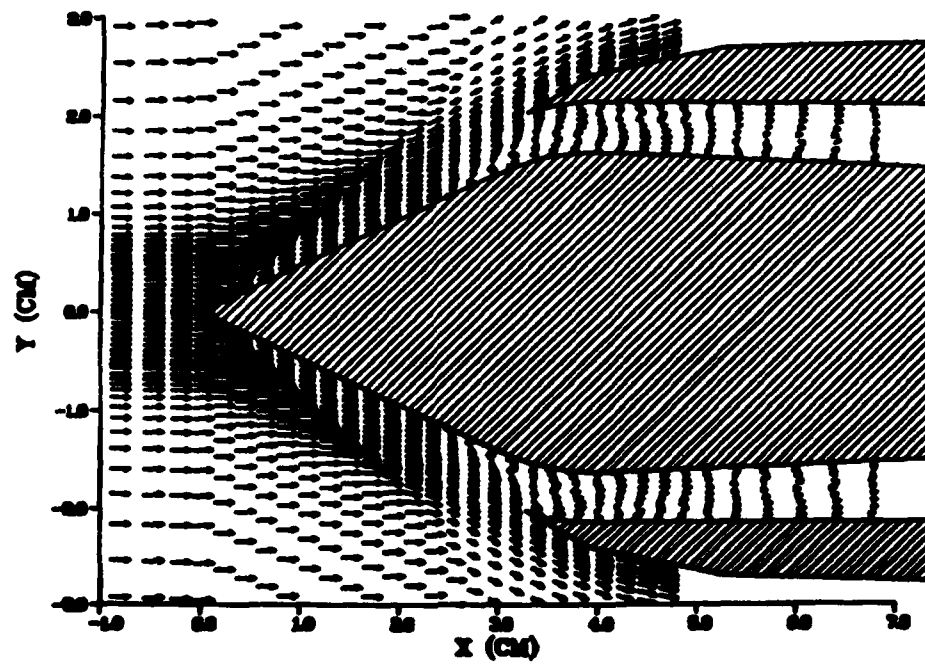
VELOCITY — TIME=.235E−01

Fig. 29   (cont.)

134

VELOCITY – TIME=.239E-01

Fig. 29 (cont.)

135
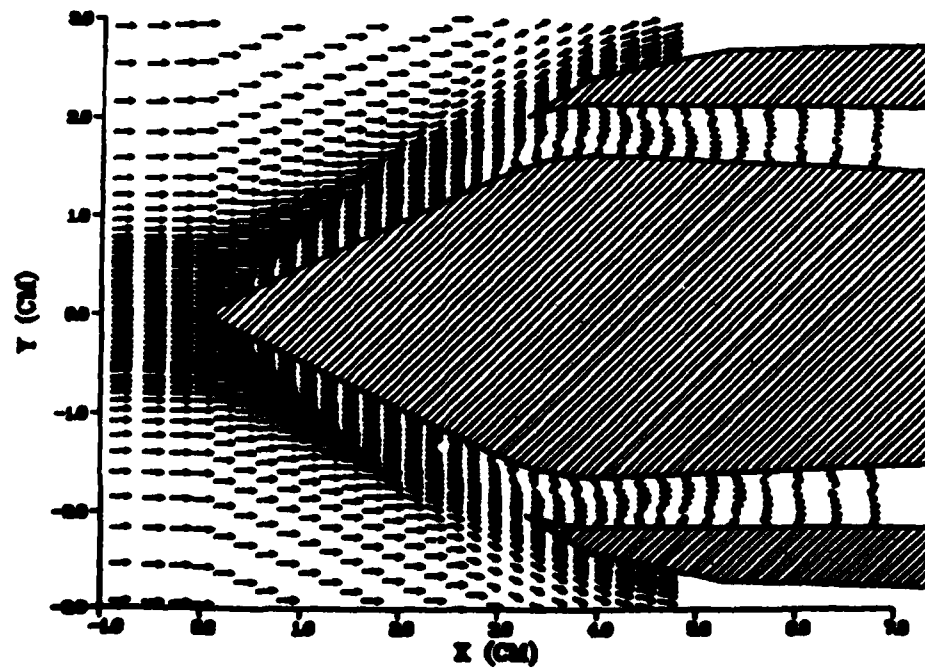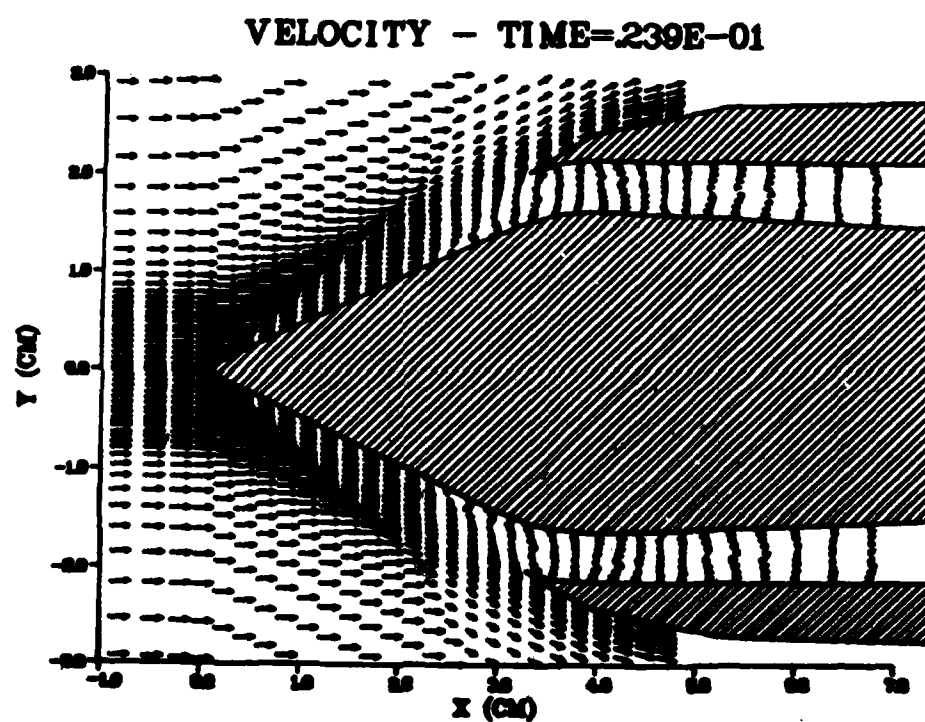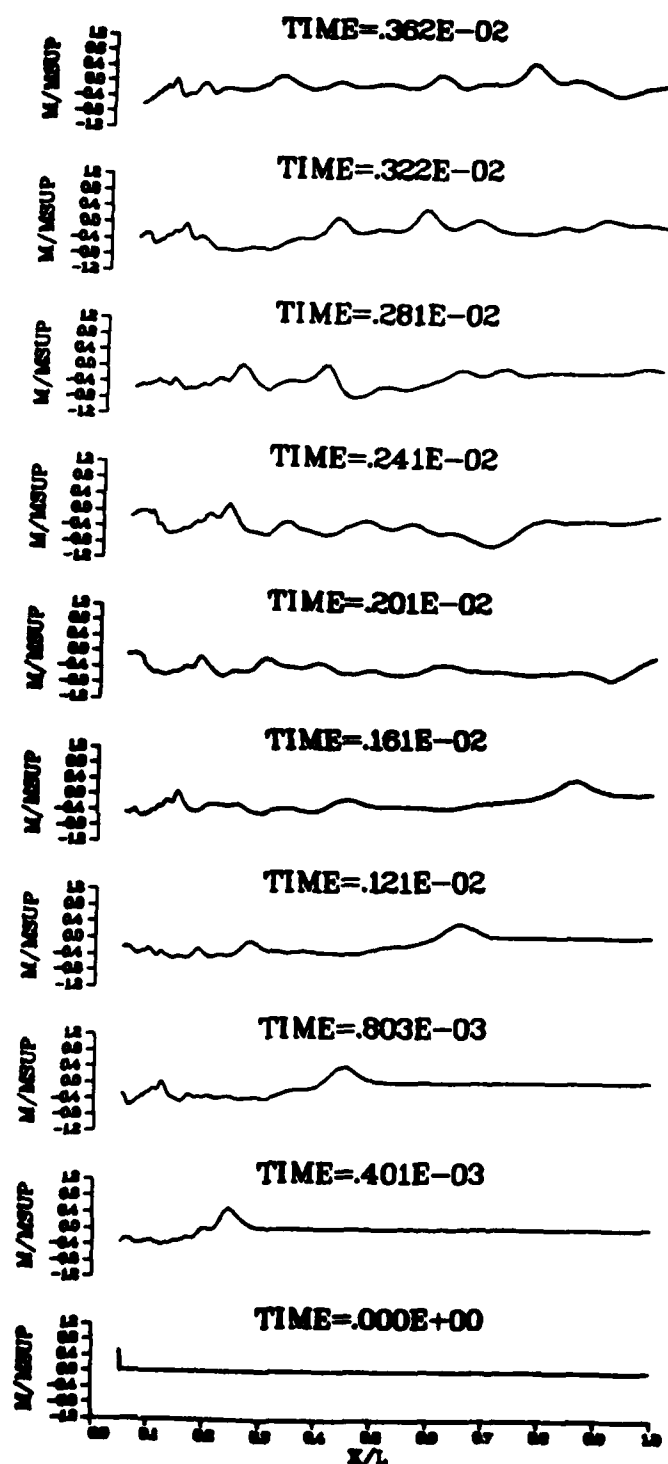
Fig. 30 Ratio of Instantaneous Mass Flux to Supercritically
Captured Mass Flux (TR=0.0, L/D=15.88)

136

Fig. 30 (cont.)

137

Fig. 30   (cont.)

138

Fig. 30 (cont.)

139

Fig. 30 (cont.)

140
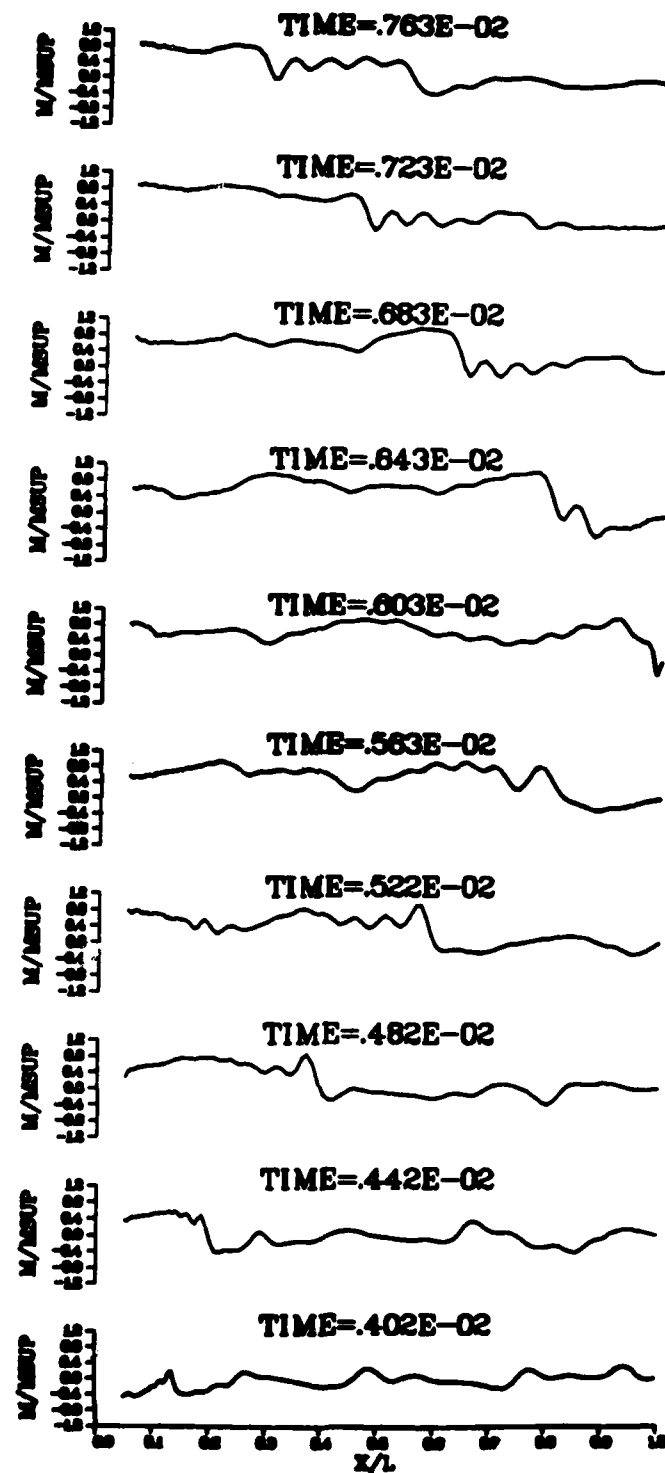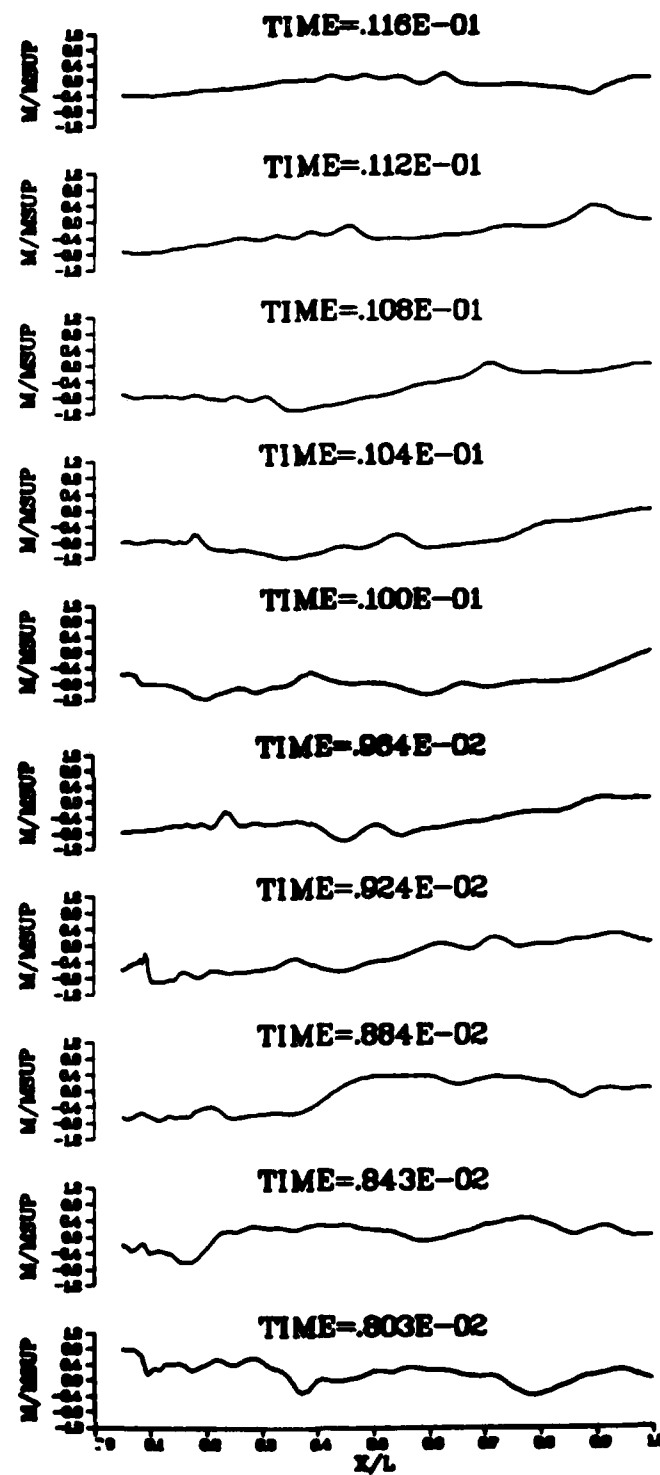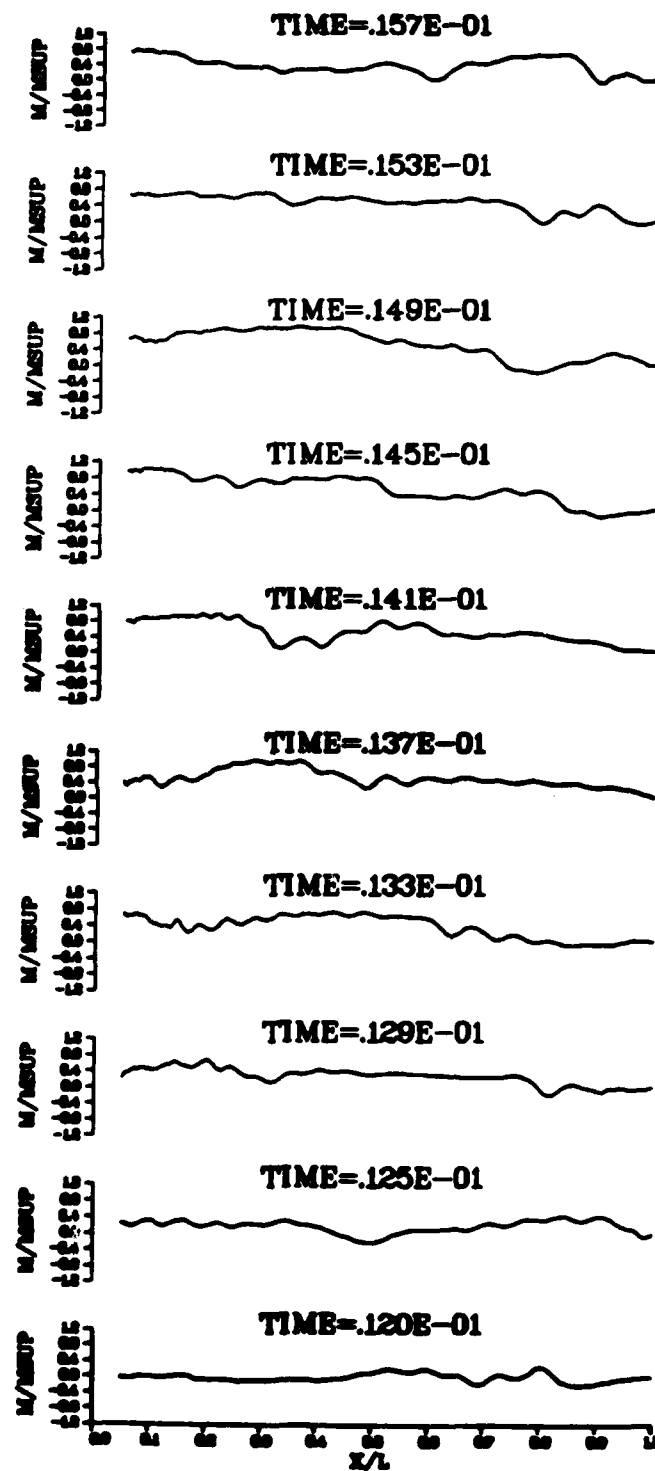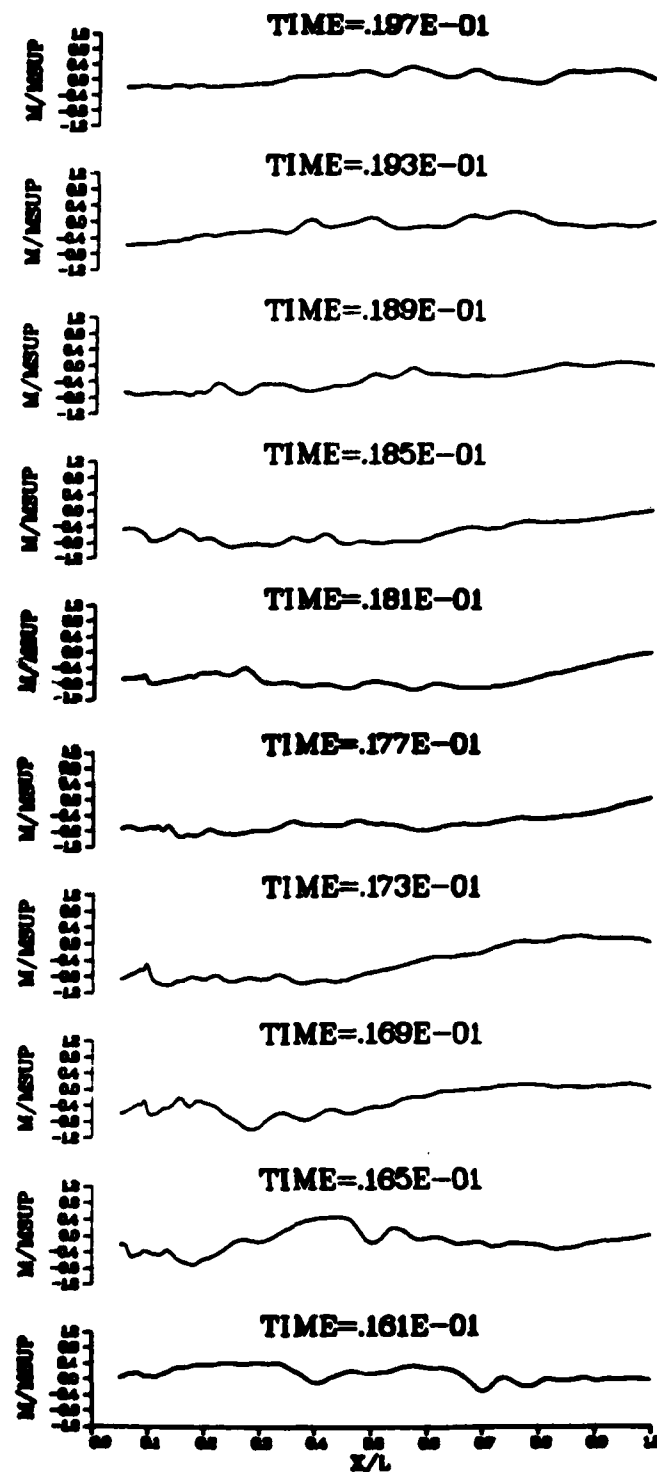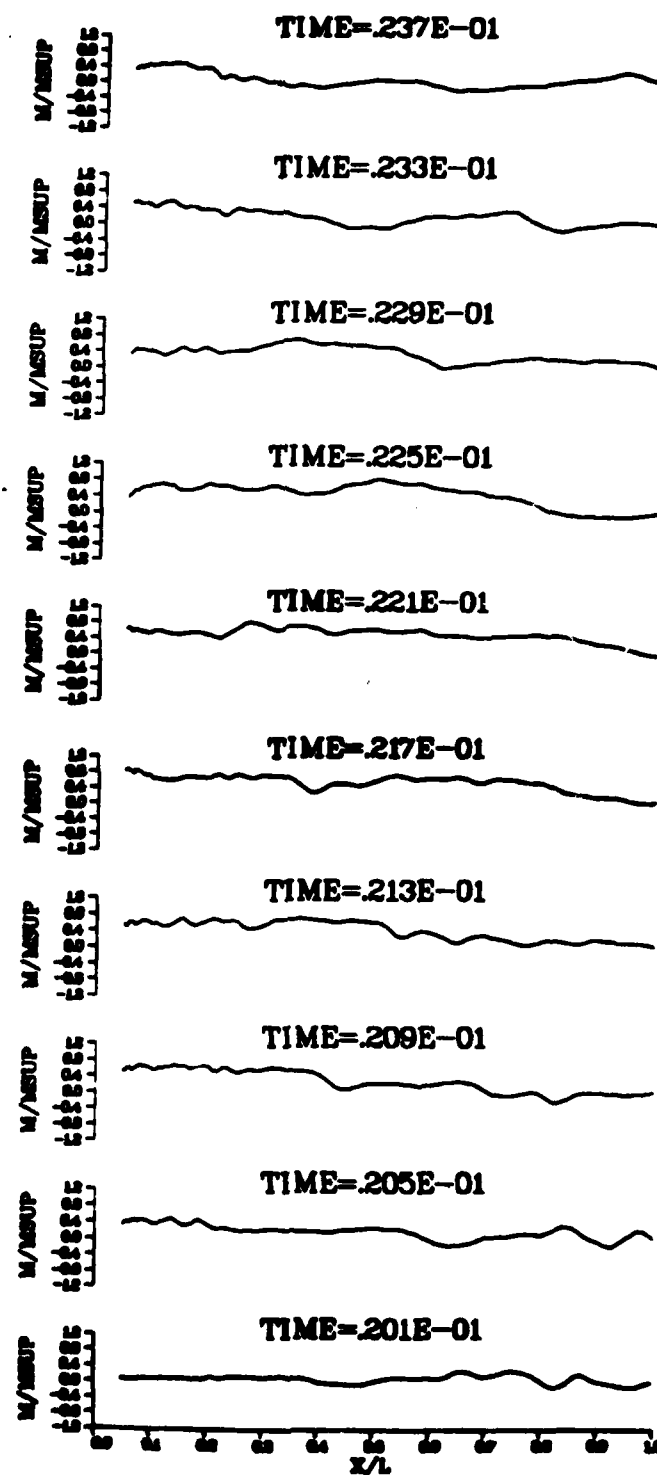
Fig. 30 (cont.)
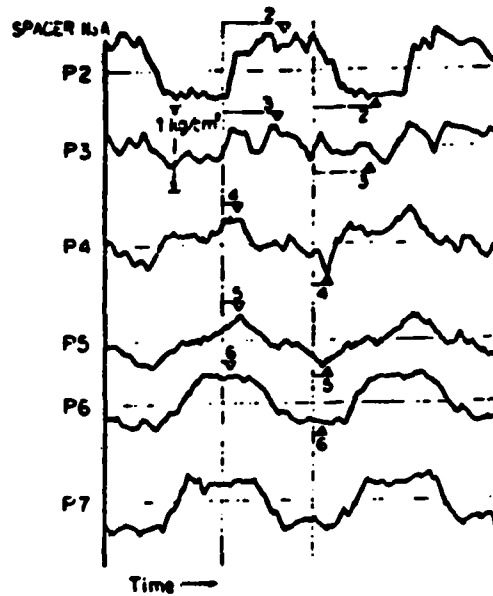
Experiment (TR=.97)
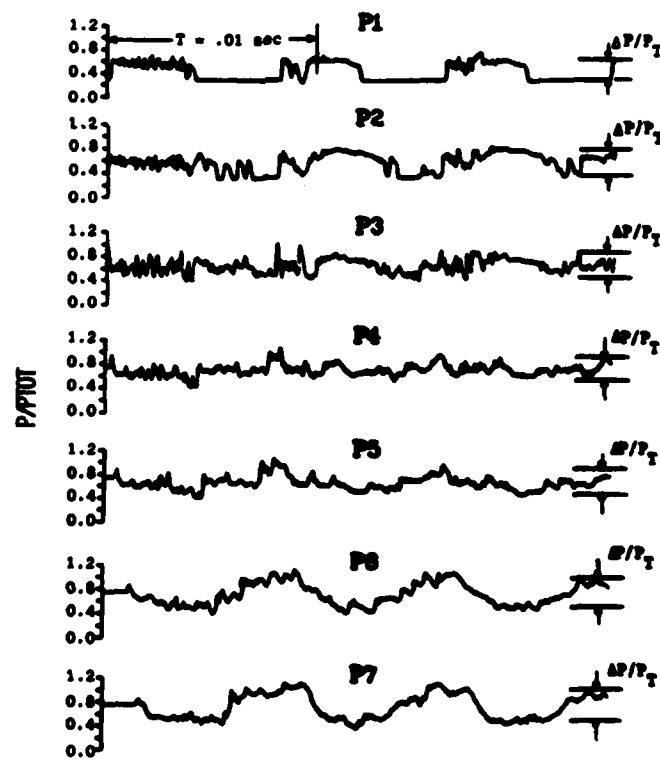
Computation (TR=0.0)

Fig. 31 Qualitative Comparison of Experimental
and Computed Pressure Waveforms

142
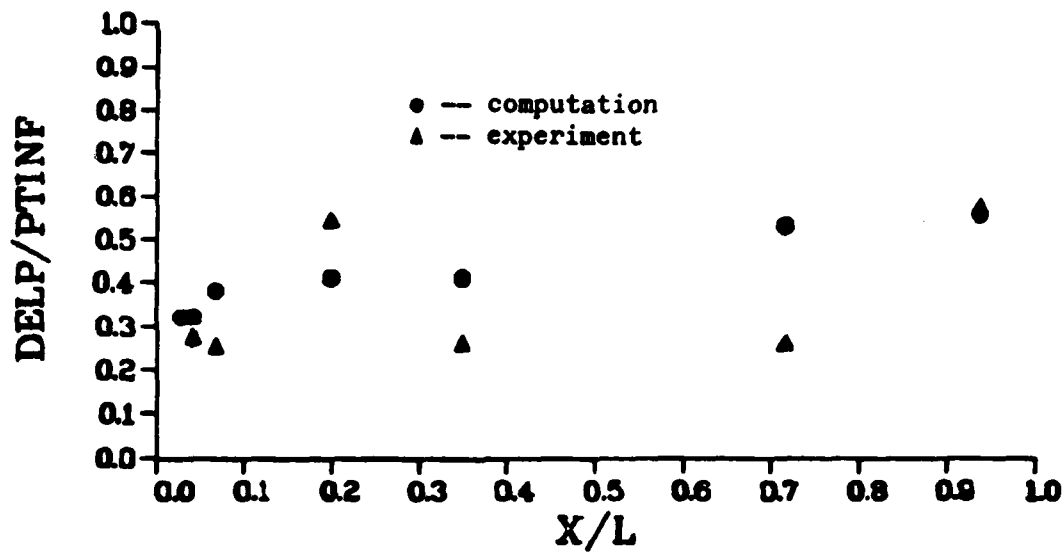
Fig. 32 Amplitude of Experimental and Computed Pressure
Fluctuations at Experimental Probe Locations
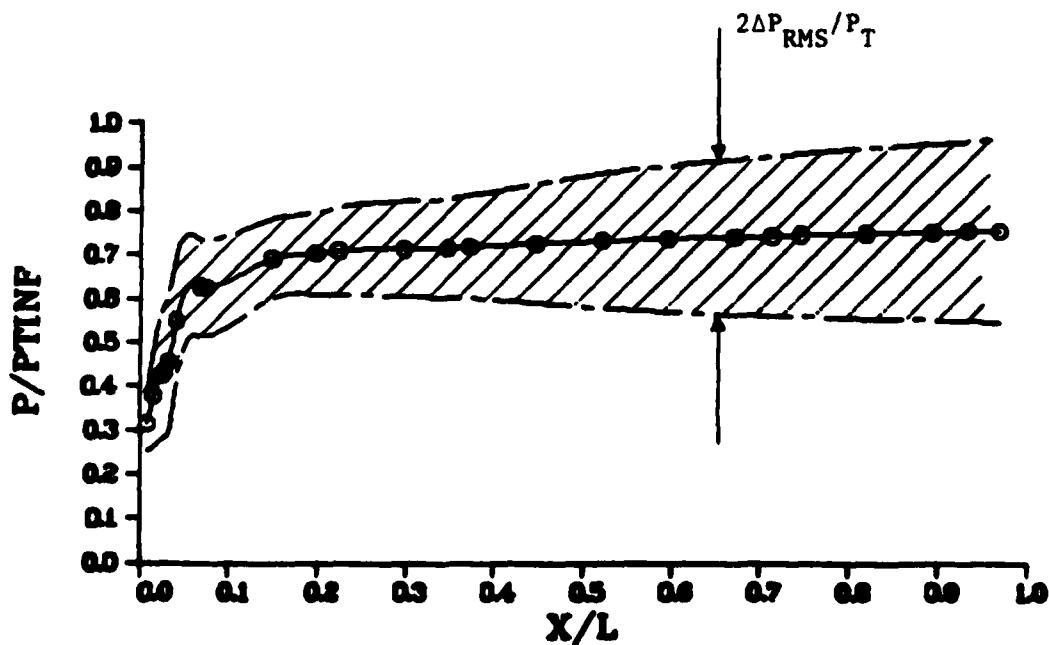
Fig. 33 Time-averaged Pressure during Three Computed Buzz Cycles
for Probe Locations of Fig. 26 and Fig. 27,
Root Mean Square (RMS) Band Indicated by Shading

Short Inlet (TR = 0.0, L/D = 10.23)

The buzz cycle obtained for this length was entirely similar to that obtained with the full length inlet. Figure 34 gives pressure-time traces at the nine probe locations shown in Figure 22. As expected, the fundamental frequency increased to 188 HZ which is in good agreement with the predicted frequency, Equation (4.4), $f_1 = 192$ HZ. The small amplitude higher frequency motion appears to be similar to that found in the full length inlet and does not scale with the length of the inlet.

Probe	X(cm)	X/L
P1	.8000	.0180
P2	2.2936	.0517
P3	4.7320	.1067
P4	9.0959	.2051
P5	15.2381	.3236
P6	21.3360	.4811
P7	27.4339	.6189
P8	30.4807	.6873
P9	39.5632	.8921

L = 44.35 cm

TABLE 3   Static Pressure Probe Locations
(L/D = 10.23, see Fig. 22)
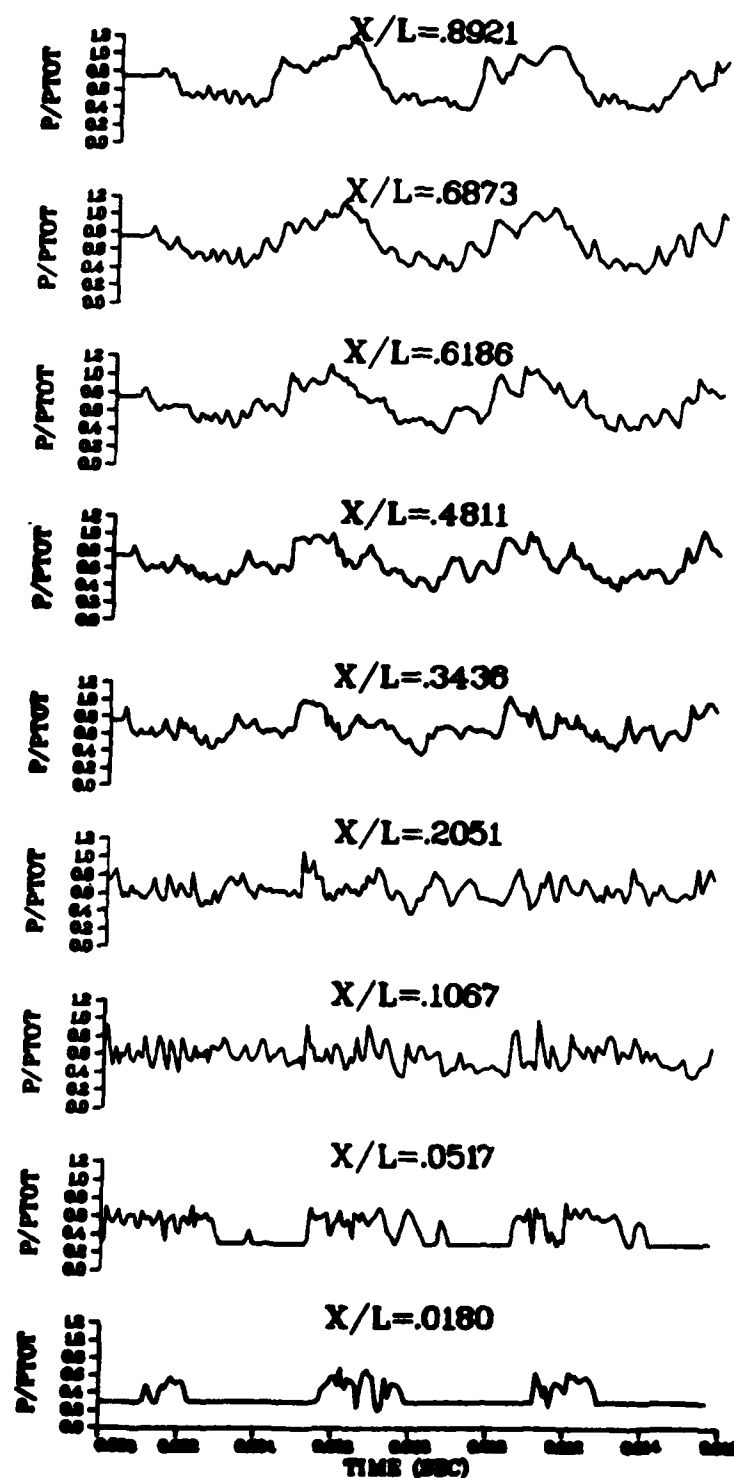
Fig. 34 Computed Pressure Fluctuations for 9 Probe
Locations (see Fig. 22), (TR=0.0, L/D=10.23)

145

Section V

CONCLUSIONS, ACCOMPLISHMENTS, AND RECOMMENDATIONS

Conclusions

A numerical method has been used to solve the unsteady, compressible Navier-Stokes equations for the flow field about an external compression axi-symmetric inlet with a length to diameter ratio, L/D = 15.88, at Mach 2.0, and a Reynolds number based upon diameter Re_D = 2.36×10^6. Solutions were obtained in the near-critical and subcritical flow regimes. The near-critical solution reached a stable steady state while the subcritical solutions were found to reach an unsteady bounded oscillatory state known as inlet buzz.

The steady state near-critical solution agreed well with all available experimental data. Investigations at the high subcritical throttle ratio, TR = .97, demonstrated a large sensitivity to turbulence modeling with the model apparently tending to damp the instability. Evidence was also found to support the hypothesis that the separated boundary layer and its flow blocking effect plays a key role in the instability mechanism. At low subcritical throttle ratios, TR = 0.0, buzz was computed for two different L/D ratios. In both cases, the dominant frequency corresponded to the fundamental mode predicted by a simple wave propagation model, and the experimentally observed shift to higher frequency modes was not found numerically. The computed solutions displayed the large amplitude pressure oscillations and traveling shock waves characteristic of inlet buzz. In addition, large regions of separated flow exhibiting a high frequency instability together with the feedback mechanism of reflected acoustic waves were clearly shown in the numerical solutions.

146

Accomplishments

The significant accomplishments resulting from the present work include the following:

1. For the first time, numerical solutions of the fundamental equations have been used to capture the naturally occurring self-sustained oscillations of an inlet operating in the subcritical flow regime.

2. The computed solutions provide further insight into buzz phenomenon. In particular, the critical importance of the separated shear layer as an amplifier of small disturbances coupled with the closed-loop feedback of reflected disturbances has been shown. Inlet buzz is thus generically related to other flows with self-sustained oscillations and can be analysed in that theoretical framework.

3. The computed near-critical steady state solution was found to be in good agreement with the experimental result. In particular, the gross behavior of the "pseudo-shock" and subsequent subsonic diffusion regions resulting from the boundary layer interaction with the terminal normal shock was predicted. To the author's knowledge, this is the first numerical solution in which this phenomenon has been observed.

4. The present work represents the first use of a choking throat in a diffuser calculation to position the shock train within the inlet. This appears to be an attractive alternative to other methods such as specifying pressure at a downstream subsonic boundary. For unsteady oscillatory flows this approach allows the passage of large amplitude disturbances through the downstream boundary with no numerical boundary condition influence on the solution.

In the course of obtaining the above numerical solutions;

5. An existing two dimensional code has been converted to axi-symmetric

147

coordinates in strong conservation law form. The resulting

code was then vectorized for efficient use on the CRAY-1S at the

A.F. Weapons Laboratory where solutions were obtained by remote

access.

6. A suitable mesh was generated and the algorithm appropriately

modified to solve for both the internal and external flow about an

axi-symmetric inlet.

Recommendations

In the course the present effort, several problem areas were dis-

covered which should be addressed in future efforts. The need for a

more economical means of obtaining numerical solutions quickly became

apparent. The solutions generated by the present explicit code were only

possible on a machine such as the CRAY. Implicit codes with unconditional

stability offer the very attractive possibility of much larger allowable

time steps. Balanced against this, the time step size necessary for

accurate temporal resolution is still restrictive and the execution time

per iteration is larger. Also, the robustness for large amplitude os-

cillatory flows as well as the efficiency on a vector processor for such

a code would need to be verified.

A second need is for a clearer understanding of the role of turbu-

lence and turbulence modeling in the solution process. The transition

region should be known from experimental results. The simple algebraic

eddy viscosity model has known deficiencies for separated flows with

large adverse pressure gradients. Turbulence models for such flows are

an area of current research. At present, it is not clear that the more

complex non-equilibrium turbulence models are superior for this type

of flow. The eddy viscosity model which, in effect, lowers the effective

148

Reynolds number of the flow by several orders of magnitude tended
to numerically damp the flow instability. Since the grid was capable
of resolving directly the lower turbulent eddy frequencies, the
turbulence model should properly account for only the higher fre-
quencies. It appears that existing turbulence models, derived from
stationary data bases, may overpredict the eddy viscosity for unsteady
mean flows with frequencies lower, but not orders of magnitude lower,
than the typical turbulent eddy frequencies. Appropriate modification
of existing turbulence models for this class of flow should be investigated.
A systematic approach to this problem, large eddy simulation, is still
in its infancy.

A final need is for more detailed experimental work. Good flow
visualization and detailed measurements are invaluable in verifying
numerical results. This is particularly true for items such as turbu-
lence which must be modeled yet appear to have a large bearing upon the
solution. In addition to errors resulting from turbulence modeling, the
computed solutions are subject to numerical error. In principle, for
steady state problems, truncation error can be removed by successive grid
refinement and techniques such as Richardson extrapolation. However, at
present, the rigorous application of such procedures is prohibitive due
to cost for many realistic problems. For unsteady flows, spatial trunca-
tion error varies as a function of time and grid refinement studies
would have to be compared at corresponding time increments. Unsteady
problems are further complicated by numerical dispersion and phase errors.
Experimental measurements provide an essential check on numerical solutions
for complex flows in which the fluid mechanics are not well understood.
In fact, numerical and experimental investigations are complimentary and

149

their joint use should produce a synergistic effect which offers the best hope of fully understanding the very complex fluid dynamic processes underlying inlet buzz.

References

1. Nagashima, T., Obokota, T., and Asanuma, T., "Experiment of Super-sonic Air Intake Buzz," Rept No 481, Institute of Space and Aeronautical Science, University of Tokyo, May 1972.

2. Faro, I, Supersonic Inlets, AGARDograph 102, May 1965.

3. Hermann, R., Supersonic Inlet Diffusers and an Introduction to Internal Aerodynamics, Minneapolis Minn., Minneapolis-Honeywell Regulator Co., 1956.

4. Oswatitsch, K., "Pressure Recovery in Missiles with Reaction Pro-pulsion at High Supersonic Speeds (The Efficiency of Shock Diffusers)." NACA TM 1140, (translation), June 1947.

5. Ferri, A. and Nucci, R.M., "The Origin of Aerodynamic Instability of Supersonic Inlets at Subcritical Conditions," NACA RM L50K30, January 1951.

6. Sterbentz, W.H. and Evvard, J.C, "Criterions for Prediction and Control of Ram-Jet Flow Pulsations," NACA TN3506, August 1955.

7. Sterbentz, W.H. and Davids, J., "Amplitude of Supersonic Diffuser Flow Pulsations," NACA TN 3572, October 1955.

8. Trimpi, R.L., "An Analysis of Buzzing in Supersonic Ram Jets by a Modified One-Dimensional Nonstationary Wave Theory," NACA TN 3695, 1956.

9. Trimpi, R.L., "A Theory for Stability and Buzz Pulsation Amplitude in Ram Jets and an Experimental Investigation Including Scale Effects," NACA Report 1265, 1956.

10. Dailey, C.L., "Supersonic Diffuser Instability," Journal of the Aeronautical Sciences, Vol. 22, No. 11, November 1955, pp. 733-749.

11. Trimpi, R.L., "Comments on Supersonic Diffuser Instability," Reader's Forum, Journal Aero. Sci., June 1956, pp. 611-612, also "Reply to Further Comments on Supersonic Diffuser Instability," Journal Aero. Sci., November 1957, pp. 846.

12. Dailey, C.L., "Further Comments on Supersonic Diffuser Instability," Readers' Forum, Journal Aero. Sci., January 1957, pp. 70-71, also "Reply," Journal Aero. Sci., November 1957, pp. 846.

13. Brown, A.C., "Investigation of Supersonic Diffuser Instability," USCEC Rept 41-101, November 1956.

14. Mirels, H., "Acoustic Analysis of Ram-Jet Buzz," NACA TN 3574, November 1955.

15. Stoolman, R., "Investigation of an Instability Phenomenon Occur-ring in Supersonic Diffusers," Ph.D. thesis, Cal. Tech., 1953.

16. Chang, C.C. and Hsu, C.T., "Solutions to Stoolman's External Diffusion Equation for Instability of a Normal Shock Inlet-Diffuser," Jet Propulsion, Vol. 28, No. 7, July 1958, pp. 457-460.

17. Chang, C.C and Hsu, C.T., "Aerodynamic Instability of Supersonic Inlet Diffusers," American Rocket Society Journal, May 1960, pp. 468-475.

18. Kowalewicz, A., "Stability Analysis of a Normal Shock Diffuser," Archiwum Mechaniki Stosowanej, Vol. 16, No. 5, 1964, pp. 1153-1179.

19. Fisher, S.A., Neale, M.C., and Brooks, A.J., "On the Subcritical Stability of Variable Ramp Intakes at Mach Numbers Around 2," R. & M. No. 3711, National Gas Turbine Establishment, February 1970.

20. Steward, D.G., and Fisher, S.A., "Instability and Turbulence in Supersonic Air Intakes," ARL/M.E. 129, Australian Defense Scientific Service, November 1970.

21. Sajben, M., Kroutil, J.C., and Chen, C.P., "Unsteady Transonic Flow in a Two-Dimensional Diffuser," AGARD Conference Proceedings No. 227, Unsteady Aerodynamics, 1977.

22. Salmon, J.T., Bogar, T.J., and Sajben, M., "Laser Velocimeter Measurements in Unsteady, Separated, Transonic Diffuser Flows," AIAA Paper No. 81-1291, June 1981.

23. Bogar, R.J., Sajben, M., and Kroutil, J.C., "Characterisitc Frequency and Length Scales in Transonic Diffuser Flow Calculations," AIAA Paper No. 81-1291, June 1981.

24. Sajben, M., Bogar, T.J., and Kroutil, J.C., "Forced Oscillation Experiments in Supercritical Diffuser Flows with Application to Ramjet Instabilities," AIAA Paper 81-1487, June 1981.

25. Knight, D.D., "Numerical Simulation of Realistic High-Speed Inlets Using the Navier-Stokes Equations," AIAA Journal, Vol. 15, No. 11, November 1977, pp. 1583-1589.

26. Knight, D.D., "Improved Calculation of High Speed Inlet Flows: Part I. Numerical Algorithm." AIAA Journal, Vol. 19, No. 1, January 1981, pp. 34-41.

27. Knight, D.D., "Improved Calculation of High Speed Inlet Flows: Part II: Results," AIAA Journal, Vol. 19, No. 2, February 1981, pp. 172-179.

28. Knight, D.D., "A Three Dimensional Navier-Stokes Code for High Speed Inlets Using the Cyber 203 Computer," Report RU-TR-156-MAE-F, Rutgers University, February 1982.

29. Buggeln, R.C., Kreskovsky, J.P., and McDonald, H., "Computation of Three-Dimensional Viscous Supersonic Flow in Inlets," AIAA Paper No. 80-0194, January, 1980.

30. Paynter, G.C., "Current Status of Inlet Flow Prediction Methods," 12th U.S. Navy Symposium on Aeroballistics, David Taylor Naval Ship Research and Development Center, Bethesda, MD., May 1981.

31. McNally, W.D., and Sockel, P.D., "Computational Methods for Internal Flows with Emphasis on Turbo-Machinery," NASA TM 82764, November 1981.

32. Levy, L.L., "Experimental and Computational Steady and Unsteady Transonic Flows About a Thick Airfoil," AIAA Journal, Vol. 16, No. 6, June 1978, pp. 564-572.

33. Steger, J.L. and Bailey, A.E., "Calculation of Transonic Aileron Buzz," AIAA Journal, Vol. 18, No. 3, March 1980, pp. 249-255.

34. Hankey, W.L. and Shang J.S., "Analysis of Pressure Oscillations in an Open Cavity," AIAA Journal, Vol. 18, No. 8, August 1980, pp. 892-898.

35. Shang, J.S., Hankey, W.L. and Smith, R.E., "Flow Oscillations of Spike Tipped Bodies," AIAA Paper 80-0062, January 1980.

36. Shang, J.S., "Oscillatory Compressible Flow Around a Cylinder," AIAA Paper No. 82-0098, January 1982.

37. Liou, M.S., Coakley, T.J., and Bergmann, M.Y., "Numerical Simulation of Transonic Flows in Diffusers," AIAA Paper No. 81-1240, June 1981.

38. Liou, M.S., and Coakley, T.J., "Numerical Simulations of Unsteady Transonic Flow in Diffusers," AIAA Paper 82-1000, June 1982.

39. Chapman, D.R., "Computational Aerodynamics Development and Outlook," AIAA Journal, Vol. 17, No. 12, December 1979, pp. 1293-1313.

40. Liepmann, H., and Roshko, Elements of Gas Dynamics, Wiley and Sons, New York, 1957.

41. Rubesin, M.W., and Rose, W.C., "The Turbulent Mean Flow Reynolds Stress and Heat Flux Equations in Mass Averaged Dependent Variables," NASA TMX-62, 248, March 1973.

42. Cebeci, T. and Smith A.M.O., Analysis of Turbulent Boundary Layers, Academic Press, New York, 1974.

43. Cebeci, T., Smith, A.M.O., and Musinkis, G., "Calculation of Compressible Adiabatic Turbulent Boundary Layers," AIAA Journal, Vol. 8, No. 11, December 1970, pp. 1974-1982.

44. Cebeci, T., "Calculation of Compressible Turbulent Boundary Layers with Heat and Mass Transfer," AIAA Journal, Vol. 9, No. 6, June 1971, pp. 1091-1097.

45. Dhawan, S. and Narashima, "Some Properties of Boundary Layer Flow During the Transition from Laminar to Turbulent Motion," _Journal of Fluid Mechanics_, No. 67, 1975.

46. Hankey, W., and Calarese, W., "Reynolds Stresses for Unsteady Turbulent Flows," Technical Note, June 1982.

47. Viviand, H., "Forms Conservative Des Equations de la Dynamique de Gas," _La Recherche Aerospatiale_, January-February 1974, pp. 65-66.

48. Vinokur, M., "Conservative Equations of Gas Dynamics in Curvilinear Coordinate Systems," _Journal of Computational Physics_, Vol. 14, February 1974, pp. 105-125.

49. Eiseman, P.R., and Stone, A.P., "Conservation Laws of Fluid Dynamics," SIAM Review, Vol. 22, No. 1, January 1980, pp. 12-26.

50. Richtmyer, R.D. and Morton, K.W., _Difference Methods for Initial-Value Problems_, 2nd Ed., Interscience Publishers, New York, 1967.

51. Roache, P.J., _Computational Fluid Dynamics_, Hermosa Publishers, Albuquerque, New Mexico, 1972.

52. Thompson, J.F., Thames, F.C., and Mastin, C.W., "Boundary Fitted Coordinate Systems for Solution of Partial Differential Equations on Fields Containing any Number of Arbitrary Two Dimensional Bodies," NASA CR-2729, July 1977.

53. Knight, D.D., "Calculation of High Speed Inlet Flows Using the Navier-Stokes Equations," AFFDL-TR-79-3138, Vol. II, February 1980.

54. MacCormack, R.W., "Numerical Solution of the Interaction of a Shock Wave with a Laminar Boundary Layer," Proceedings of the Second International Conference on Numerical Methods in Fluid Dynamics, University of California, Berkley, Sept. 1970, pp. 151-163.

55. MacCormack, R.W., and Baldwin, B.S., "A Numerical Method for Solving the Navier-Stokes Equations with Application to Shock-Boundary Interactions," AIAA Paper 75-1, January 1975.

56. MacCormack, R.W., and Paullay, A.J., "Computational Efficiency Achieved by Time Splitting of Finite Difference Operators," AIAA Paper 72-154, January 1972.

57. Yanenko, No W., _The Method of Fractional Steps_, Springer-Verlag, Berlin, 1971.

58. Lomax, H., "Recent Progress in Numerical Techniques for Flow Simulation," _AIAA Journal_, Vol. 14, No. 4, April 1976, pp. 512-518.

59. MacCormack, R.W., "A Numerical Method for Solving the Equations of Compressible Viscous Flow," _AIAA Journal_, Vol. 20, No. 9, Sept. 1982, pp. 1275-1281.

60. Beam, R.M., and Warming, R.F., "An Implicit Factored Scheme for the Compressible Navier-Stokes Equations," *AIAA Journal*, Vol. 16, No. 4, April 1978, pp. 393-402.

61. Levine, R.D., "Super Computers," *Scientific American*, January 1982, pp. 118-135.

62. Calahan, D.A., "Notes on Vector Processing with the CRAY 1," Seminar at the Flight Dynamics Laboratory, WPAFB, OH, June 9-12, 1980.

63. Anon, CRAY-1, Fortran (CFT) Reference Manual, Mendota Heights, Minnesota, 1979.

64. Shang, J.S., Buning, P.G., Hankey, W.L., and Wirth, M.G., "The Performance of a Vectorized 3-D Navier-Stokes Code on the CRAY-1 Computer," AIAA Paper 79-1448, July 1979.

65. Rockwell, D., and Naudasher, E., "Self-Sustained Oscillations of Impinging Free Shear Layers," *Annual Review of Fluid Mechanics*, 1979, pp. 67-94.

66. Hankey, W.L., and Shang, J.S., "Analysis of Self-Excited Oscillations in Fluid Flows," AIAA Paper 80-1346, July 1980.

67. Rayleigh, Lord, "On the Stability or Instability of Certain Fluid Motions," *Scientific Papers*, Vol. 1, Cambridge University Press, 1880, pp. 474-484.

68. Michalke, A., "On the Inviscid Instability of the Hyperbolic Tangent Velocity Profile," *Journal of Fluid Mechanics*, Vol. 19, 1964.

69. Roscoe, D.G., and Hankey, W.L., "The Stability of a Compressible Free Shear Layer," AFWAL-TR-80-3016, October 1979.

70. Verma, G.R., Hankey, W.L., and Scherr, S.J., "Stability Analysis of the Lower Branch of the Falkner-Skan Equations," AFFDL-TR-3116, July 1979.

71. Schlicting, H., *Boundary Layer Theory*, McGraw-Hill, New York, 1968.

72. Stetson, K., Air Force Wright Aeronautical Laboratory, private communication, June 1982.

73. Shapiro, A., *The Dynamics and Thermodynamics of Compressible Fluid Flow*, Vol. I & II, the Ronald Press, New York, 1954.

74. Emmons, H. (Ed.), *Fundamentals of Gas Dynamics*, Vol. III, High Speed Aerodynamics and Jet Propulsion, Princeton University Press, Princeton, New Jersey, 1958.

75. Hunter, L., Maj., "The Study of Normal Shocks (Pseduo Shocks) with Application to Supersonic Diffusers,' AFWAL-TM-82-184, Air Force Wright Aeronautical Laboratories, WPAFB, OH, March 1981.

Appendix A

DIFFERENCE OPERATORS USED IN
MACCORMACK'S ALGORITHM (PHYSICAL VARIABLES)

First Derivatives

$$\nabla_x f_{i,j} = (f_{i,j} - f_{i-1,j})/\Delta x = (\partial_x f)_{i,j} + \{-\frac{1}{2}(\partial_{xx}f)_{i,j}\Delta x + \ldots\}$$

$$\Delta_x f_{i,j} = (f_{i+1,j} - f_{i,j})/\Delta x = (\partial_x f)_{i,j} + \{\frac{1}{2}(\partial_{xx}f)_{i,j}\Delta x + \ldots\}$$

$$\delta_x f_{i,j} = \frac{1}{2}(\nabla_x + \Delta_x)f_{i,j} = (f_{i+1,j} - f_{i-1,j})/2\Delta x$$

$$= (\partial_x f)_{i,j} + \{\frac{1}{6}(\partial_{xxx}f)_{i,j}\Delta x^2 + \ldots\}$$

Second Derivatives

$$\delta_{xx} f_{i,j} = \nabla_x\Delta_x f_{i,j} = \Delta_x\nabla_x f_{i,j} = (f_{i+1,j} - 2f_{i,j} + f_{i-1,j})/\Delta x^2$$

$$= (\partial_{xx}f)_{i,j} + \{\frac{1}{12}(\partial_{xxxx}f)_{i,j}\Delta x^2 + \ldots\}$$

$$\delta_{xy} f_{i,j} = \frac{1}{2}(\nabla_x + \Delta_x)\delta_y f_{i,j} = \delta_x\delta_y f_{i,j}$$

$$= (f_{i+1,j+1} - f_{i+1,j-1} + f_{i-1,j-1} - f_{i-1,j+1})/4\Delta x\Delta y$$

$$= (\partial_{xy}f)_{i,j} + \{\frac{1}{6}(\partial_{xxxy}f)_{i,j}\Delta x^2 + \frac{1}{6}(\partial_{xyyy}f)_{i,j}\Delta y^2 + \ldots\}$$

Similar operators may be defined for derivatives with respect to y, as well as derivatives with respect to the transformed variables, ξ,η.

Appendix B

TRUNCATION ERROR FOR MACCORMACK'S ALGORITHM

Because of the asymmetric differencing in time and space it is not immediately obvious what the order of the truncation error terms are in MacCormack's method. It is useful to demonstrate the second order accuracy of the algorithm rigorously. In what follows, it is not necessary to consider the individual terms of the F vector. In particular, differencing of the viscous derivative terms can be shown to be of equivalent accuracy as the inviscid terms and need not be considered in detail. Also, because of the use of splitting, it is only necessary to consider one spatial dimension.

Given the non-linear system of equations

$$\frac{\partial}{\partial t} (U) + \frac{\partial}{\partial x} (F) = 0 \tag{B.1}$$

where $U(x,t)$, $F(U)$ are n-dimensional vectors (for the present case, n=4). A difference equation approximation may be written as

$$\overline{U_i^{n+1}} = U_i^n - \sigma (F_i^n - F_{i-1}^n) \tag{B.2}$$

$$U_i^{n+1} = \frac{1}{2} [U_i^n + \overline{U_i^{n+1}} - \sigma (\overline{F_{i+1}^{n+1}} - \overline{F_i^{n+1}})] \tag{B.3}$$

where

$$\sigma = \frac{\Delta t}{\Delta x}$$

Provisional time levels in the corrector are eliminated by substituting the following expansions:

$$\overline{F_i^{n+1}} = F (\overline{U_i^{n+1}}) = F_i^n + \left(\frac{\partial F}{\partial U}\right)_i^n (\overline{U_i^{n+1}} - U_i^n)$$

$$+ \frac{1}{2} \left(\frac{\partial^2 F}{\partial U^2}\right)_i^n (\overline{U_i^{n+1}} - U_i^n)^2 + \ldots$$

$$\overline{F_{i+1}^{n+1}} = F(\overline{u_{i+1}^{n+1}}) = F_{i+1}^n + (\frac{\partial F}{\partial U})_{i+1}^n \; (\overline{U_{i+1}^{n+1}} - U_{i+1}^n)$$

$$+ \frac{1}{2} (\frac{\partial^2 F}{\partial U^2})_i^n \; (\overline{U_{i+1}^{n+1}} - U_{i+1}^n)^2 + \ldots \qquad (B.4)$$

in which

$$\frac{\partial F}{\partial U} = A - n \times n \text{ Jacobian matrix}$$

$$\frac{\partial^2 F}{\partial U^2} - \text{3rd order } n \times n \times n \text{ tensor.}$$

However, from the predictor,

$$\overline{U_i^{n+1}} - U_i^n = - \sigma \; (F_i^n - F_{i-1}^n)$$

$$\overline{U_{i+1}^{n+1}} - U_{i+1}^n = - \sigma \; (F_{i+1}^n - F_i^n) \qquad (B.5)$$

and thus

$$\overline{F_i^{n+1}} = F_i^n - \sigma(\frac{\partial F}{\partial U})_i^n \; (F_i^n - F_{i-1}^n) + \frac{\sigma^2}{2} (\frac{\partial^2 F}{\partial U^2})_i^n \; (F_i^n - F_{i-1}^n)^2 + \ldots$$

$$\qquad (B.6)$$

$$\overline{F_{i+1}^{n+1}} = F_{i+1}^n - \sigma(\frac{\partial F}{\partial U})_{i+1}^n \; (F_{i+1}^n - F_i^n) + \frac{\sigma^2}{2} (\frac{\partial^2 F}{\partial U^2})_i^n \; (F_{i+1}^n - F_i^n)^2 + \ldots \; .$$

Taylor series expansions may be used to give,

$$U_i^{n+1} = U_i^n + \Delta t \; U_{t_i}^n + \frac{\Delta t^2}{2} U_{tt_i}^n + \frac{\Delta t^3}{6} U_{ttt_i}^n + \ldots$$

$$F_{i+1}^n = F_i^n + \Delta x \; F_{x_i}^n + \frac{\Delta x^2}{2} F_{xx_i}^n + \frac{\Delta x^3}{6} F_{xxx_i}^n + \ldots \qquad (B.7)$$

$$F_{i-1}^n = F_i^n - \Delta x \; F_{x_i}^n + \frac{\Delta x^2}{2} F_{xx_i}^n - \frac{\Delta x^3}{6} F_{xxx_i}^n + \ldots$$

Substituting Eqns. (B.6), (B.7) into (B.3) will give, to the lowest
order remaining terms,

$$[U_t + F_x + \frac{\Delta x^2}{6} \{F_{xxx}\} - \frac{\Delta t \Delta x}{4} \frac{\partial}{\partial x} \{ \frac{\partial}{\partial x}(\frac{\partial F}{\partial U}) \; F_x \}$$

$$+ \Delta t^2 \{ \frac{1}{6} U_{ttt} + F_x \; (\frac{1}{2} \frac{\partial^2 F}{\partial U^2} F_{xx} + \frac{1}{4} \frac{\partial}{\partial x}(\frac{\partial^2 F}{\partial U^2}) \; F_x) \}$$

$$= - \frac{\Delta t}{2} \{ U_{tt} - \frac{\partial}{\partial x} (\frac{\partial F}{\partial U} F_x) \}]_i^n \qquad (B.8)$$

158

However, from the exact equation, (B.1)

$$\frac{\partial U}{\partial t} = -\frac{\partial F}{\partial x}$$

and thus

$$U_{tt} = \frac{\partial}{\partial t}(-F_x) = -\frac{\partial}{\partial x}\left(\frac{\partial F}{\partial U} u_t\right) = \frac{\partial}{\partial x}\left(\frac{\partial F}{\partial U} F_x\right) \qquad (B.9)$$

The right hand side of Eqn. (B.8) is then identically zero and the difference algorithm generates an approximation of the form,

$$U_t + F_x + O(\Delta x^2) + O(\Delta x \Delta t) + O(\Delta t^2) = 0 \qquad (B.10)$$

159

SPLITTING

The concept of operator factoring or time splitting was introduced in Section III as an efficient method of solving multi-dimensional system of equations.

It remains to show that this does not affect the formal accuracy of the numerical method. Lomax, (Ref 58), has introduced a simple procedure in order to prove:

(1) A symmetric operator sequence is a necessary condition for second order temporal accuracy,

(2) In the linear case, a symmetric operator sequency recovers the full second order accuracy of the algorithm.

In what follows, the spatial accuracy is unaffected by the time splitting and does not need to be considered in detail. The two dimensional equation

$$\frac{\partial U}{\partial t} + \frac{\partial F}{\partial x} + \frac{\partial G}{\partial y} = 0 \tag{C.1}$$

may be written in quasi-linear form as

$$\frac{\partial U}{\partial t} + A_x \frac{\partial U}{\partial x} + A_y \frac{\partial U}{\partial y} = 0 \tag{C.2}$$

where

$$A_x = \frac{\partial F}{\partial U} \qquad A_y = \frac{\partial G}{\partial U}$$

If the Jacobian matrices, A_x A_y are assumed to be constant, the system is then linear. A second order accurate solution to Eqn. (C.2) must reproduce the terms of a Taylor series expansion up to order two.

$$U^{n+1} = U^n + \Delta t\, U_t + \frac{\Delta t^2}{2} U_{tt} + O(\Delta t^3) \tag{C.3}$$

But from Eqn. (C.2)

$$U_t = (A_x\, \partial_x + A_y\, \partial_y)\, U$$

$$U_{tt} = (A_x^2\, \partial_{xx} + (A_x A_y + A_y A_x)\, \partial_{xy} + A_y^2\, \partial_{yy})U \tag{C.4}$$

160

A numerical approximation to Eqn. (C.3) may be generated by time splitting as the symmetric sequence,

$$U^{n+1} = L_y(\frac{\Delta t}{2}) \; L_x(\Delta t) \; L_y(\frac{\Delta t}{2}) \; U^n \tag{C.5}$$

or

$$U^* = L_y U^n \; , \; U^{**} = L_x U^* \; , \; U^{n+1} = L_y U^{**}$$

The L_y operator solves the equation

$$\frac{\partial U}{\partial t} + A_y \frac{\partial U}{\partial y} = 0 \tag{C.6}$$

by the MacCormack predictor-corrector to give the second order accurate approximation

$$U^* = L_y(\frac{\Delta t}{2}) \; U^n \tag{C.7}$$

where

$$L_y(\frac{\Delta t}{2}) = I + \frac{\Delta t}{2} A_y \; \delta_y + \frac{1}{2} (\frac{\Delta t}{2})^2 \; A_y^2 \; \delta_{yy}$$

The L_x operator similarly solves

$$\frac{\partial U}{\partial t} + A_x \frac{\partial U}{\partial x} = 0$$

to give

$$U^{**} = L_x(\Delta t) \; U^* \tag{C.8}$$

where

$$L_x(\Delta t) = I + \Delta t \; A_x \; \delta_x + \frac{1}{2} (\Delta t)^2 \; A_x^2 \; \delta_{xx}$$

Then Eqn. (C.5) may be written as

$$U^{n+1} = (I + (\frac{\Delta t}{2}) \; A_y \; \delta_y + \frac{1}{2} (\frac{\Delta t}{2})^2 \; A_y^2 \; \delta_{yy})(I + \Delta t \; A_x \; \delta_x + \frac{1}{2} \Delta t^2 A_x^2 \delta_{xx}) \tag{C.9}$$

$$x (I + (\frac{\Delta t}{2}) \; A_y \; \delta_y + \frac{1}{2} (\frac{\Delta t}{2})^2 \; A_y^2 \; \delta_{yy}) U^n$$

which may be expanded to give

$$U^{n+1} = \{ I + \Delta t (A_y \; \delta_y + A_x \; \delta_x) \tag{C.10}$$

$$+ \frac{\Delta t^2}{2} (A_y^2 \; \delta_{yy} + [A_x A_y + A_y A_x] \delta_x \delta_y + A_x^2 \delta_{xx}) \} u^n + O(\Delta t^3)$$

since

$$\delta_y \, \delta_y = \delta_{yy}$$

$$\delta_x \, \delta_y = \delta_y \delta_x$$

Equation (C.10) thus produces a second order accurate approximation to Eqn. (C.3). If the non-symmetric sequence

$$U^{n+1} = L_x \, (\Delta t) \, L_y(\Delta t) \, U^n \tag{C.11}$$

is used the second order term is then

$$\frac{\Delta t^2}{2} \, (A_y^2 \, \delta_{yy} + 2A_x A_y \, \delta_x \delta_y + A_x^2 \, \delta_{xx})$$

This however, does not agree with Eqn. (C.4) because matrix multiplication is not commutative

$$2 \, A_x A_y \neq A_x A_y + A_y A_x$$

Thus a symmetric sequence is a necessary condition for the linear as well as more general non-linear system of equations for second order accuracy.

Appendix D

STABILITY CRITERIA FOR THE TRANSFORMED

NAVIER-STOKES EQUATIONS

The purpose of this appendix is to show how the stability analysis
of MacCormack and Baldwin (Ref 55) may be generalized for the trans-
formed equations written in computational variables. The dominant
inviscid limit will be considered in some detail and a simple general-
ization then given for the viscous corrections. Attention will be
restricted to the L_ξ operator, Eqn. (3.36). Inviscid terms in Eqn.
(3.37) may be written in non-conservative form as:

$$\frac{\partial}{\partial t} (U) + \xi_x \frac{\partial}{\partial \xi} (F_I) + \xi_y \frac{1}{y} \frac{\partial}{\partial \xi} (yG_I) = 0 \qquad (D.1)$$

where

$$U = \begin{bmatrix} \rho \\ \rho u \\ \rho v \\ \rho E \end{bmatrix} \qquad F_I = \begin{bmatrix} \rho u \\ \rho u^2 \\ \rho uv \\ \rho uE \end{bmatrix} \qquad G_I = \begin{bmatrix} \rho v \\ \rho uv \\ \rho v^2 \\ \rho vE \end{bmatrix}$$

The spectral radius of the amplification matrix, G, associated with
Eqn. (D.1), may be more conveniently found if a change of dependent
variables is made, (Ref 50: Sec 13.4):

$$V = \begin{bmatrix} \rho \\ u \\ v \\ p \end{bmatrix} \qquad (D.2)$$

Equation (D.1) can then be written in quasi-linear form as

$$\frac{\partial}{\partial t} (V) + A \frac{\partial V}{\partial \xi} + F_1 V = 0 \qquad (D.3)$$

where

$$A = \begin{bmatrix} U_c & \xi_x\rho & \xi_y\rho & 0 \\ 0 & U_c & 0 & \xi_x/\rho \\ 0 & 0 & U_c & \xi_y/\rho \\ 0 & \xi_x\gamma p & \xi_y\gamma p & U_c \end{bmatrix}$$

$$F_1 = \begin{bmatrix} 0 & 0 & 0 & \rho \\ 0 & 0 & 0 & 0 \\ 0 & 0 & 0 & 1/\rho \\ 0 & 0 & (\gamma-1)p & 0 \end{bmatrix}$$

$$U_c = \xi_x u + \xi_y v$$

Following Ricthmyer (Ref 50: Sec 8.4), the lower order term F_1V may be neglected. The amplification matrix for Eqn. (D.3) may be determined as outlined in Section III and has been given by MacCormack (Ref 54) as

$$G = I - i \frac{\Delta t}{\Delta\xi} A \sin\alpha - \frac{1}{2} \left(\frac{\Delta t}{\Delta\xi}\right)^2 \{A(1-e^{-i\alpha})\}^2 \qquad (D.4)$$

where

$$i = \sqrt{-1} \qquad I - \text{identity matrix}$$

$$\alpha = k_\xi \Delta\xi - \text{phase angle}$$

To find the stability restriction, one must find the largest eigenvalue of the matrix A, which now differs from Reference (55) due to the presence of the transformation derivatives:

$$\lambda_A = U_c, \; U_c, \; U_c \pm \sqrt{\xi_x^2 + \xi_y^2} \; c \qquad (D.5)$$

of which

$$(\lambda_A)_{max} = U_c + \sqrt{\xi_x^2 + \xi_y^2} \; c$$

The eigenvalues of the amplification matrix are then

$$\lambda = 1 + i \frac{\Delta t}{\Delta \xi} \lambda_A \sin \alpha + \frac{1}{2} \left(\frac{\Delta t}{\Delta \xi}\right)^2 \{ \lambda_A (1-e^{-i\alpha}) \}^2 \tag{D.6}$$

For stability,

$$|\lambda| = \left[1-\left(\frac{\Delta t}{\Delta \xi}\right)^2 \lambda_A^2 (1-\cos \alpha)\right]^2 + \left[\left(\frac{\Delta t}{\Delta \xi}\right) \lambda_A \sin \alpha\right]^2 \le 1 \tag{D.7}$$

Substituting $(\lambda_A)_{max}$ into Eqn. (D.7) and differentiating with respect to α to find the extremal values gives

$$\left. |\lambda(\lambda_A, \alpha)| \right|_{\alpha=\pi/2} = |\lambda|_{max} \le 1 \tag{D.8}$$

From Eqn. (D.8), for stability

$$(\Delta t_\xi)_{inv} \le \frac{\Delta \xi}{(\lambda_A)_{max}} = \frac{\Delta S_\xi}{|U_\xi|+c} \tag{D.9}$$

where

$$\Delta S_\xi = \frac{\Delta \xi}{\sqrt{\xi_x^2 + \xi_y^2}} \qquad , \qquad U_\xi = \frac{U_c}{\sqrt{\xi_x^2 + \xi_y^2}}$$

Equation (D.9) may be compared with results given by MacCormack, (Ref 55).

$$(\Delta t_x)_{inv} = \frac{\Delta x}{|u|+c} \tag{D.10}$$

The similarity in form suggests that the viscous corrections may be generalized by a simple change of variables:

$$(\Delta t_x)_{diff} = \frac{1}{2} \frac{\Delta x^2}{\gamma \mu/(Pr\rho)} \qquad \text{(Ref 55)} \tag{D.11}$$

becomes

$$(\Delta t_\xi)_{diff} = \frac{1}{2} \frac{\Delta S_\xi^2}{\gamma\left(\frac{\mu}{Pr} + \frac{\epsilon}{Pr_t}\right)/\rho} \tag{D.12}$$

and

$$(\Delta t_x)_{md} = \frac{\Delta x \Delta y}{\sqrt{-\lambda\mu/\rho}} \qquad \text{(Ref 55)} \tag{D.13}$$

165

becomes

$$(\Delta t_\xi)_{md} = \frac{\Delta S_\xi \Delta S_\eta}{\sqrt{\lceil(\mu+\xi)(\lambda+\lambda_t)\rceil}/\rho}$$ (D.14)

where

$$\Delta S_\eta = \frac{\Delta\eta}{\sqrt{\eta_x^2+\eta_y^2}}$$

Corresponding expressions for the L_η operator may be derived in a similar manner.

Appendix E

THROTTLE RATIO CORRECTION TO AREA RATIO

As mentioned in Section 4.4, the throttle ratio settings given in Reference 1 are based upon the exit area of the holes in the cowling. Since this is not the physical choking area, a procedure must be used to determine the choking area if the numerical simulation is to be run at the same condition as the experiment.

Referring to Figure 35, throttle ratio, TR, is based upon the exit area

$$A_e = \kappa \pi R_1 h \qquad (E.1)$$

where κ is a constant which accounts for the area reduction due to the presence of struts at the outlet. The choking area is calculated as
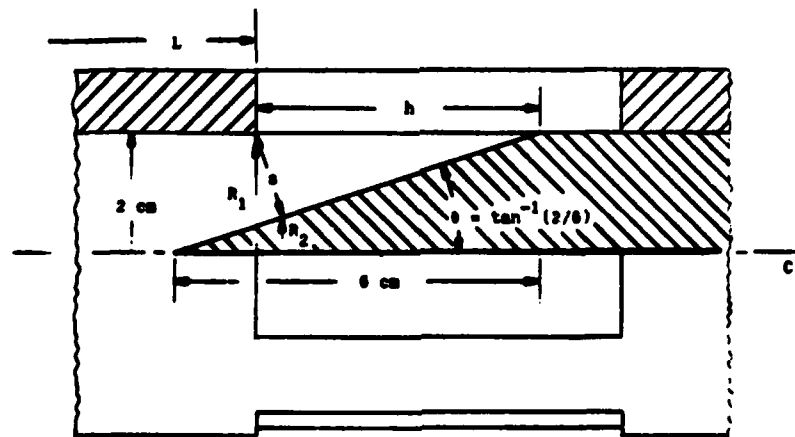
$$A_* = \pi s \ (R_1 + R_2) \qquad (E.2)$$

Fig. 35 Experimental Throttle Value Geometry

167

The two can not be related because the constant κ was not reported in Ref 1. One-dimensional relationships may be used to determine the throat area, A_t, such that the pressure values agree with the results of Figure 7 from the experiment. For any steady state flow, the mass flux across all crossectional areas of the duct must be identically equal. The mass flux, captured by the inlet in the supercritical regime, $\dot{m}_{cap}$, was calculated by applying the Navier-Stokes equations only to the upstream region and may be considered known.

Since the area ratio and pressure at station 7 were given, this station may be used to infer properties at the downstream throat. A one-dimensional area ratio may be written as

$$\frac{A_7}{A_{*_{eff}}} = \frac{1}{M_7}\left[\frac{2}{(\gamma+1)}\left(1 + \frac{\gamma-1}{2}M_7^2\right)\right]^{\frac{\gamma+1}{2(\gamma-1)}} \qquad (E.3)$$

where $A_{*_{eff}}$ is the area required to choke the throat from the values specified at station 7. If there is little total pressure loss from station 7 to the throat, $p_{t_*} = p_{t_7}$, $A_{*_{eff}}$ will be the desired area after correcting for boundary layer displacement effects. The mass flux across station 7 is given as

$$\dot{m}_7 = \sqrt{\frac{\gamma}{R}}\,\frac{p_7}{\sqrt{T_{t_7}}}\,M_7\sqrt{1 + \frac{\gamma-1}{2}M_7^2}\,A_7 = \dot{m}_{cap} \qquad (E.4)$$

with $A_7 = \pi R_1^2$

$p_7 = p_{t_\infty}(p_7/p_{t_\infty})$ \hfill (from Figure 7)

Equation (E.4) may be solved for M_7 which is, in turn, substituted into Eqn (E.3) to give $A_{*_{eff}}$. The actual geometric area will be somewhat

larger than $A_{*_{eff}}$ due to the presence of the boundary layers

$$A_* = \frac{A_{*_{eff}}}{\varepsilon_d} \qquad\qquad (E.5)$$

The displacement correction was obtained from preliminary aft-diffuser calculations in which mass-averaged quantities were computed from the numerical solution and substituted into Eqn (E.4) written at the nozzle throat. After solving for $A_{*_{eff}}$, with the geometric area known, the displacement correction was set as $\varepsilon_d = .969$.

Now that the two areas have been related, the blockage constant, κ, can be computed once and for all. For TR = 1.42

$$A_e = TR \times A_c = 7.668 \text{ cm}^2$$

where A_c is given as 5.4 cm^2. To match the resulting pressure at station 7 (Fig. 7) requires

$$A_* = 6.367 \text{ cm}^2.$$

Upon using Eqn (E.2) and trignometric relationships from Figure (E.1)

$$R_1 = 2 \text{ cm}$$

$$R_2 = R_1 - s \cos \theta$$

$$s = h \sin \theta$$

the geometry is completely determined. Eqn (E.1) can then be solved to calculate the blockage constant

$$\kappa = .655 \simeq .66$$

Once this constant has been fixed, the two areas are directly related by geometry. For $\kappa = .66$, TR = 1.42 corresponds to an area ratio

$$AR = A_e/A_* = 1.162$$

In a similar manner, TR = .97 corresponds to AR = .834.

After the numerical solution has been obtained, the validity of
the assumptions made in the analysis may be checked by computing one
dimensional mass-averaged properties from the full solution. For
TR = 1.42

$$P_{t_*}/P_{t_7} = .995$$

$$\varepsilon_d = A_{*_{eff}}/A_* = .967$$

VITA

Richard W. Newsome, Jr. was born on 19 April 1952 in Augusta, Georgia. He graduated from high school in Aiken, South Carolina in 1970 and entered the US Air Force Academy from which he received the degree of Bachelor of Science in Aeronautical Engineering in June 1974. Upon graduation, he was commissioned in the USAF and assigned, through the Air Force Institute of Technology, to Purdue University from which he received an M.S. in Aeronautics and Astronautics in May 1975. He was assigned to the Deputy for Engineering, Aeronautical System Division, Wright-Patterson AFB in September 1975 as a propulsion performance engineer. In July of 1978, he entered the doctorial program of the Air Force Institute of Technology. In July 1981, he began his current assignment in the Computational Aerodynamics Group of the Flight Dynamics Laboratory, AF Wright Aeronautical Laboratories. He was married to Mary A. Boyle on May 24, 1975. The Newsome's have two children, Brian and Laura.

Permanent Address: 3429 Summit Drive
                   Aiken, South Carolina, 29801

REPORT DOCUMENTATION PAGE		READ INSTRUCTIONS BEFORE COMPLETING FORM
1. REPORT NUMBER AFIT/DS/AA/82-2	**2. GOVT ACCESSION NO.** AD-A124 747	**3. RECIPIENT'S CATALOG NUMBER**
4. TITLE *(and Subtitle)* Numerical Solutions for Critical and Unsteady Subcritical Flow about an External Compression Axi-Symmetric Inlet		**5. TYPE OF REPORT & PERIOD COVERED** PhD Dissertation
		6. PERFORMING ORG. REPORT NUMBER
7. AUTHOR(s) Richard W. Newsome Jr. Captain, USAF		**8. CONTRACT OR GRANT NUMBER(s)**
9. PERFORMING ORGANIZATION NAME AND ADDRESS Air Force Institute of Technology (AFIT-EN) Wright-Patterson AFB, Ohio 45433		**10. PROGRAM ELEMENT, PROJECT, TASK AREA & WORK UNIT NUMBERS** Project 2307-N6-03
11. CONTROLLING OFFICE NAME AND ADDRESS Flight Dynamics Laboratory (AFWAL/FIMM) Air Force Wright Aeronautical Laboratories Wright-Patterson AFB, Ohio 45433		**12. REPORT DATE** November 1982
		13. NUMBER OF PAGES 170
14. MONITORING AGENCY NAME & ADDRESS*(if different from Controlling Office)*		**15. SECURITY CLASS. *(of this report)*** Unclassified
		15a. DECLASSIFICATION/DOWNGRADING SCHEDULE

16. DISTRIBUTION STATEMENT *(of this Report)*

Approved for public release; distribution unlimited

17. DISTRIBUTION STATEMENT *(of the abstract entered in Block 20, if different from Report)*

18. SUPPLEMENTARY NOTES

Approved for public release: IAW AFR 190-17.

LYNN E. WOLAVER
Dean for Research and Professional Development
Air Force Institute of Technology (ATC)
Wright-Patterson AFB OH 45433

4 JAN 1983

19. KEY WORDS *(Continue on reverse side if necessary and identify by block number)*

Navier-Stokes equations	Unsteady flow
Numerical Solutions	Self-Sustained oscillations
Buzz	
Inlet Buzz	

20. ABSTRACT *(Continue on reverse side if necessary and identify by block number)*

The unsteady, compressible, Reynolds-averaged Navier-Stokes equations were solved for the flow field about an external compression axi-symmetric inlet with a length to diameter ratio, $L/D=15.88$, at Mach 2.0 and a Reynolds number based on diameter, $Re_D = 2.36 \times 10^6$, operating in the near-critical and subcritical flow regimes. The near-critical solution reached a stable steady state while the subcritical solutions attained an unstable bounded oscillatory state, characterized by large amplitude pressure oscillations and traveling

DD $_{1 \text{ JAN } 73}^{\text{FORM}}$ **1473**   EDITION OF 1 NOV 65 IS OBSOLETE

shock waves. This phenomenon is a result of a shear layer instability combined with a closed-loop feedback of reflected disturbances and the naturally occurring self-sustained oscillations are commonly known as buzz. Numerical results are given in terms of Mach contours, velocity field plots, pressure-time traces at selected stations, as well as mass flux and other mass-averaged quantities along the duct length. Comparison with experiment is also given.

END

FILMED

3-83

DTIC